Land-Atmosphere Interaction and Radiative-Convective Equilibrium

by

Timothy Cronin

B.A., Swarthmore College (2006)

Submitted to the Department of Earth, Atmospheric, and Planetary Science
in partial fulfillment of the requirements for the degree of

Doctor of Philosophy in Climate Physics and Chemistry

at the

MASSACHUSETTS INSTITUTE OF TECHNOLOGY

June 2014

Author . . . .
Department of Earth, Atmospheric, and Planetary Science
February 14, 2014

Certified by. . . . .
Kerry A. Emanuel
Cecil and Ida Green Professor of Atmospheric Science
Thesis Supervisor

Accepted by . . . .
Robert van der Hilst
Schlumberger Professor of Earth and Planetary Sciences
Head of Department of Earth, Atmospheric, and Planetary Sciences

Land-Atmosphere Interaction and Radiative-Convective Equilibrium

by

Timothy Cronin

Abstract

I present work on several topics related to land-atmosphere interaction and radiative-convective equilibrium: the first two research chapters invoke ideas related to land-atmosphere interaction to better understand radiative-convective equilibrium; the last two research chapters use the framework of radiative-convective equilibrium to better understand land-atmosphere interaction.

First, I calculate how averaging the incident solar radiation can lead to biases in idealized climate models. I derive an expression for the absorption-weighted solar zenith angle, which minimizes the bias in mean absorbed shortwave radiation, and I find that it is closely matched by the insolation-weighted zenith angle. Common use of daytime-weighted zenith angle likely leads to high biases in albedo by $\sim$3%.

Second, I explore the time scales of approach to radiative-convective equilibrium with both a simple linearized two-variable model, and a single-column model with full physics. I show that there is a long time scale of approach to radiative-convective equilibrium that is order hundreds of days even when the surface heat capacity vanishes. The impact of water vapor on the effective atmospheric heat capacity can more than double this time scale for warm temperatures and low surface heat capacities.

Third, I develop an analytic theory for the sensitivity of near-surface temperature to properties of the land surface. I show that the theory compares well against a simple numerical model of the coupled boundary layer-surface system, as well as a more complex two-column model, and discuss application of the theory to questions of how changes in land use or ecosystem function may affect climate change.

Finally, I find that the diurnal cycle of convection is important for the spatial distribution of rainfall in idealized simulations of radiative-convective equilibrium with a cloud-resolving model. In a region that is partly an island and mostly ocean, precipitation over the island falls primarily in a regular, strong, afternoon thunderstorm, with a time-mean rainfall rate more than double the domain average. I explore mechanisms for this island rainfall enhancement, investigate the importance of island size for my results, and find that the upper troposphere warms with the inclusion of an island, which may have implications for the large-scale tropical circulation.

3

Thesis Supervisor: Kerry A. Emanuel
Title: Cecil and Ida Green Professor of Atmospheric Science

Acknowledgments

It's been a wonderful four and a half years as a grad student here at MIT, and there are so many people to thank for making it so! First, thanks to Kaya, for constantly reminding me of what is truly important, keeping me sane and happy all this time, and for traveling with me to small tropical islands (for leisure, not research).

I'm deeply indebted to Kerry Emanuel for conversations and helpful input on all of the chapters of this paper, and for the selflessness to suggest that I should be sole author on two papers (chapters 2 and 4); it is rare to find such integrity.

Thanks as well to the other members of Kerry's group, who I've worked and laughed with, in contexts ranging from confusing figures on someone's desk, to the ferry to Alcatraz, to New Orleans streetcars and Newport beaches. From the long hours spent talking about SAM with Alli Wing, to the loud laughter of Dan Chavas next door that would inevitably lead to me stopping by for 30-minute science and politics chats, to the early suggestion by Morgan O'Neill that I work with Kerry's RC model for a class project first semester: you all helped me immensely. I have also appreciated help from the two remaining atmosphere and climate students who started back in the fall of 2009: Marty Singh's endless patience for me stopping by to ask questions and shoot the breeze about radiative-convective equilibrium and cloud-resolving models has been impressive, as has Mike Byrne's willingness to read through paper drafts of mine, and even run simulations to test ill-fated ideas. Thanks as well to Malte Jansen for sparking the "Purple Monster" reading group which served me so well, and to my erstwhile office-mates, Laura Meredith and Diane Ivy, who showed me the ropes in my first two years here. Conversations with my student mentor, Daniela Domeisen, were also important in pushing me to join Kerry's group, for which I'm thankful. Finally, to Ryan Abernathey, thank you for encouraging me to get a Ph.D in PAOC before I even knew what "PAOC" stood for!

It was an incredible stroke of luck to have Peter Molnar on my thesis committee. The benefits included, but were not limited to: visiting him and enjoying excellent food and lodging each summer in the mountains of Colorado; receiving thoughtful

reviews and writing advice on drafts of all papers in a matter of days; hiking with him up mountains and calling it work; and attentive scientific mentoring from a top-notch geophysicist. I would highly recommend him to any graduate student who has not yet formed their thesis committee (though I suspect the number of such students reading this will forever remain zero).

I would also like to thank the faculty in PAOC, especially Ron Prinn, who advised me up until generals. I'm grateful that switching to Kerry's group for a better research fit occurred entirely without personal or professional friction. The other members of my thesis committee – Paul O'Gorman, David McGee, and Adam Schlosser – were supportive and helpful when I asked, though in the end I didn't end up leaning on them very hard. Scientists from other places who have kept my faith in the scientific method include Alan Betts, Adam Sobel, Tapio Schneider, Frank Robinson, and – last but not least – Marat Khairoutdinov, who generously and freely provided the code for SAM with which the simulations in Chapter 5 were performed.

Thanks to my parents, Greg and Lois, and my brother Ben, for encouragement and support, and to my uncle Jeff for pushing me to go back to school. Getting a Ph.D feels like it was the right choice, and coming at the end of writing a thesis, I think that means something.

Contents

Chapter 1

Overview

In this thesis, I attempt to make progress on a collection of topics, related to land-atmosphere interaction and radiative-convective equilibrium. Chapters 2 and 3 discuss ways in which thinking about land-atmosphere interaction yields insights about radiative-convective equilibrium; Chapters 4 and 5 discuss ways in which the framework of radiative-convective equilibrium allows for advances in our understanding on land-atmosphere interaction. With the conceit of anthropomorphism, this thesis is a conversation between two characters in the climate system: one called land-atmosphere interaction, and the other radiative-convective equilibrium. Each learns something from the other, and both come away with new understanding when the conversation is over. Land-atmosphere interaction opens the conversation, whispering words of caution to radiative-convective equilibrium, that the diurnal cycle of solar radiation is important, and attempting to average the sun invites peril (Chapter 2). Land-atmosphere interaction then insists to radiative-convective equilibrium that including an interactive surface can have impacts on the time-scale of approach to radiative-convective equilibrium, which are not merely a result of the thermal inertia of the surface itself (Chapter 3). Radiative-convective equilibrium then takes over as the protagonist, suggesting to land-atmosphere interaction that a simple coupled land-atmosphere model can be understood via a sensitivity analysis that is akin to global climate sensitivity, and with radiative-convective equilibrium as an atmospheric basic state (Chapter 4). Finally, radiative-convective equilibrium closes the

conversation by asserting that it should be the natural basic state of the atmosphere for looking at the problem of land-atmosphere interaction and rainfall enhancement over tropical islands (Chapter 5).

Radiative-convective equilibrium is arguably the older and more rigorous of the two characters. Radiative-convective equilibrium is predated by the concept of pure radiative equilibrium, wherein the thermal structure of an atmosphere is set by the balance between absorbed and emitted radiation at each level. Pure radiative equilibrium dates back to the early 20th century (*Schwarzschild*, 1906; *Eddington*, 1926), but its physics apply more realistically to stars than planets. Radiative equilibrium applies quite well to intermediate layers of stellar atmospheres, but stellar atmospheres become convective in their outer layers; this situation is typically reversed for planetary atmospheres, where the lower layers are typically convecting, and the upper layers often close to radiative equilibrium. Convection is a necessary ingredient in a zero-order model of the Earth's atmosphere, because the pure radiative equilibrium state is unstable to convective overturning; this convective instability results from the emissivity discontinuity at the Earth's surface, the rapid decay of water vapor mixing ratio with height, and pressure broadening of strong absorption lines (*Weaver and Ramanathan*, 1995). The first calculations of radiative-convective equilibrium, where radiative cooling of the atmosphere is balanced by convective heating through the depth of the troposphere, were performed in the mid-1960s (*Manabe and Strickler*, 1964; *Manabe and Wetherald*, 1967). These initial computations made crude assumptions about the critical atmospheric lapse rate, used simple hard convective adjustment schemes, and included only climatological relative humidity and cloud fields, but by enforcing surface and top-of-atmosphere energy balances, they provided a firm foundation for predictions about the sensitivity and stability of Earth's climate. Nearly a half century later, radiative-convective equilibrium is a widely accepted paradigm, which continues to serve as a jumping-off point for addressing many fundamental questions in climate, such as planetary habitability (*Wordsworth et al.*, 2010), existence of multiple equilibria (*Renno*, 1997; *Emanuel et al.*, 2014; *Abbot and Tziperman*, 2008), and scaling of the hydrological cycle with temperature (*Pierrehum-*

bert, 2002; *Takahashi*, 2009; *Romps*, 2011). But the meaning of radiative-convective equilibrium for much of the atmospheric science community has also shifted over the past 20 years; with single-column models increasingly replaced by "Cloud-Resolving Models." Influential studies with such models (*Held et al.*, 1993; *Tompkins and Craig*, 1998a,b) made decisions to fix the sea surface temperature (SST), so as to reduce required simulation times, and focused on atmosphere-only radiative-convective equilibrium, where the atmospheric energy and water balance hold, but surface energy balance does not. Study of atmospheric convection in cloud-resolving models with fixed SST has since proliferated, to the great benefit of our understanding of moist convection, but somewhat to the detriment of using radiative-convective equilibrium to understand climate, where surface temperature must be allowed to change with time, and energy balance of the entire atmosphere-surface system is a key principle.

Land-atmosphere interaction has long but shallow roots, with a limited intuitive understanding of the impact of land on climate stretching back at least centuries, perhaps even millennia, but with more influential and quantitatively rigorous work occurring only in the last few decades. The influence of land-ocean contrasts on atmospheric winds – especially with regards to the land and sea breeze – has long been realized (*Halley*, 1686; *Davis et al*, 1889), as has the influence of land on the amplitude of the seasonal cycle of surface temperatures (*Ward*, 1906). A fuller analysis of the impact of land on climate awaited the development of early atmospheric general circulation models, where the importance of various processes in the land-atmosphere system could be tested. Work by *Charney* (1975) and *Shukla and Mintz* (1982) highlighted that the properties of the land surface can indeed profoundly affect the hydrological cycle and air temperatures on regional scales. Coupling can either transform the system qualitatively, introducing new instabilities to the land-atmosphere system that would not exist in an isolated model of either, or quantitatively, giving substantially different sensitivities than would be predicted by a stand-alone land model forced by changes in atmospheric properties (e.g, *Jacobs and De Bruin* (1992)).

Consideration of the importance of land in the climate often emphasizes ways in which land and ocean differ. One key difference is that water is generally not freely

available for evaporation over land; the evaporation of water is regulated not only by atmospheric demand, but also by surface supply via plants and soils. Another key difference is that the heat capacity of land surfaces is relatively low, so that the diurnal cycle of surface temperature and energy balance is important. As noted by *Zeng and Neelin* (1999), it does not make sense to prescribe land surface temperature as a boundary condition to an atmospheric model, as is often done for the sea surface, because the thermal adjustment time scale of the land surface temperature is small compared to nearly all processes of meteorological interest. Furthermore, it often does not make sense to prescribe surface temperatures even over the ocean, because specification of surface temperatures eliminates the important constraint of surface energy balance. It is here that we find the main point of contact, the bit of shared language that both of our characters can speak to find common ground: surface energy balance is a fundamental concern in both land-atmosphere interaction and in radiative-convective equilibrium, though this latter point has been increasingly forgotten. Much of the conversation that is this thesis grows out of this shared concern for surface energy balance.

In Chapter 2, I calculate how averaging the incident solar radiation can lead to biases, and I suggest a way of averaging that minimizes biases. Idealized climate modeling studies, including many simulations of radiative-convective equilibrium, often perform such averaging of solar radiation over space and/or time, in order to simplify boundary conditions or eliminate a source of undesired forced variability. But averaging the solar zenith angle can introduce biases in the average albedo, even if the incoming solar energy at the top of the atmosphere is correct. To address this issue, I develop the idea of an absorption-weighted zenith angle, which is the zenith angle for which the partitioning of sunlight between absorption and reflection is the same as it would be in the time-mean, for a time-varying solar zenith angle. If the albedo depends linearly on the cosine of the zenith angle, then the absorption-weighted zenith angle is equal to the insolation-weighted zenith angle. Calculations with a radiative transfer model show that if clouds play a dominant role in reflection of sunlight, then the albedo likely does depend nearly linearly on the cosine of the zenith angle. For

single-column radiative-convective modeling studies of Earth's mean climate, the use of daytime-weighted zenith angle, rather than insolation-weighted zenith angle, may underestimate the absorption of solar radiation by $\sim$10 W/m². I also find that other studies, which use three-dimensional climate models and spatially homogeneous insolation, may overestimate the absorption of solar radiation because they use a zenith angle that is too low in comparison to the absorption-weighted zenith angle.

In Chapter 3, I explore the question of how long it takes to get to radiative-convective equilibrium when the surface temperature is interactive. Using a two-variable model for perturbation surface and atmospheric temperature, I find that a long time scale of approach to radiative-convective equilibrium emerges, and remains long even in the limit that the surface heat capacity vanishes. This climate time scale is given by $\tau_C \approx (C_A + C_S)/B$, where C_A is the effective atmospheric heat capacity, C_S is the surface heat capacity, and B is the change in outgoing longwave radiation with respect to change in atmospheric temperature. The effective heat capacity of the atmosphere includes not only the dry heat capacity of the atmosphere, but also the latent heat capacity of the atmosphere, or amount of energy needed to evaporate the water associated with warming the atmosphere by a unit amount at constant relative humidity. The latent heat capacity of the atmosphere increases with temperature, and surpasses the dry heat capacity of the atmosphere near current tropical temperatures, which greatly lengthens τ_C, especially when the surface heat capacity is small. I use a single-column radiative-convective model to explore the validity of this simple model, and find a close correlation between modeled and theoretical relaxation time scales, given the ability to diagnose several key parameters from equilibrium model states.

In Chapter 4, I introduce the framework of boundary-layer climate sensitivity, which parallels the widely used framework of global climate sensitivity. I derive an analytic sensitivity theory for the case of an idealized model of a well-mixed boundary layer over land from *Betts* (2000). Forcings are identified as changes in land surface properties, such as surface conductance to water vapor, albedo, and surface roughness, that affect the surface energy budget. Feedbacks are associated with the four different fluxes involved in surface energy balance: latent and sensible turbulent

13

fluxes, and longwave and shortwave radiative fluxes. As in previous work (*Brubaker and Entekhabi*, 1996), I find that the strongest negative feedback is associated with the dependence of the latent heat flux on the surface temperature. Using nonlinear forcings is quite important for understanding sensitivity to large changes in land surface properties, and I find that the surface wetness has an evaporative forcing with a saturating nonlinearity that is mathematically similar to the saturation of radiative forcing by carbon dioxide. The theory agrees well with the numerical model of *Betts* (2000); both the theory and the numerical model are compared with simulations by a two-column radiative-convective model (*Abbot and Emanuel*, 2007), with generally good agreement. I explore limitations of the theory, and apply the theory to estimate the magnitude of temperature changes over land as a result of "physiological forcing", or the effects of carbon dioxide on plant stomata and the partitioning of turbulent surface enthalpy fluxes.

In Chapter 5, I use radiative-convective equilibrium as a framework for trying to understand why tropical islands are rainier than nearby ocean areas (*Sobel et al.*, 2011; *As-syakur et al.*, 2013), and whether this rainfall enhancement could have an impact on the general circulation of the tropical atmosphere. I perform simulations of radiative-convective equilibrium with a three-dimensional cloud-system resolving model (SAM, *Khairoutdinov and Randall* (2003)), where the surface temperature is interactive everywhere, but a region of reduced surface heat capacity is included to represent an island. The heterogeneous surface heat capacity is allowed to interact with a regular diurnal cycle of solar insolation. With surface heat capacity as the only contrast between island and ocean, I find that the diurnal cycle strongly "rectifies," with time-mean ascent over the simulated island and a doubling of time-mean rainfall as compared to the ocean. As measured by extreme quantiles of cloud-top height, vertical velocity, and surface precipitation rate, convection is far more intense over the island than the ocean. The timing of peak rainfall varies with island size, from early afternoon over smaller islands, to near sunset over larger islands; the principal lag that changes with island size is the lag between maximum surface enthalpy fluxes and maximum rainfall. Island rainfall enhancement is mostly due to

atmospheric moisture convergence, which scales non-monotonically with island size, and has a maximum value for an island radius of $\sim$20 km. I discuss thermodynamic rectification mechanisms, but find them unlikely to be the primary explanation for island rainfall enhancement. I then present the dynamical rectification mechanism of convection-stability nonlinearity as a more likely candidate for explaining island rainfall enhancement. I idealize the mechanism with a simulation where a dry, unstratified, nonrotating atmosphere is subjected to a lower boundary buoyancy forcing that is localized in space, periodic in time, and has zero mean value; in this simulation, mean ascent develops over the island-like region with the temporally varying buoyancy forcing. I find that the upper troposphere generally warms with the inclusion of an island, which suggests that a region with islands would be favored for large-scale ascent, as compared to a region without islands. I extend the theory of the linear sea breeze to the case of cylindrical symmetry and the limit of substantial thermal and momentum damping, and I suggest that the several-hour phase lag between maximum surface enthalpy fluxes and maximum rainfall may be related to the finite spin-up time for a sea breeze circulation.

In Chapter 6, I present a summary of key results from the four research chapters, as well as the potentially broader implications of the results from each chapter. I then outline three big questions in climate science: stability and multiple equilibria, variability-mean state interaction, and cloud-climate interaction. In each case, I discuss how the big question relates to the work that I have done so far, and how it lights the way for future work, by myself or others.

Chapter 2

On the Choice of Average Solar Zenith Angle

Abstract

Simulations with idealized climate models often choose to neglect spatiotemporal variations in solar radiation, but doing so comes with an important decision about how to average solar radiation in space and time. Since both clear-sky and cloud albedo are increasing functions of the solar zenith angle, one can choose an absorption-weighted zenith angle which reproduces the spatial- or time-mean absorbed solar radiation. Here, we perform calculations for a pure scattering atmosphere and with a more detailed radiative transfer model, and find that the absorption-weighted zenith angle is usually between the daytime-weighted and insolation-weighted zenith angles, but much closer to the insolation-weighted zenith angle in most cases, especially if clouds are responsible for much of the shortwave reflection. Use of daytime-average zenith angle may lead to a high bias in planetary albedo of $\sim$3%, equivalent to a deficit in shortwave absorption of $\sim$10 W m^{-2} in the global energy budget (comparable to the radiative forcing of a roughly sixfold change in CO_2 concentration). Other studies that have used general circulation models with spatially constant insolation have underestimated the global-mean zenith angle, with a consequent low bias in planetary albedo of $\sim$2-6%, or a surplus in shortwave absorption of $\sim$7-20 W m^{-2} in the global energy budget.

2.1 Introduction

Comprehensive climate models suggest that a global increase in absorbed solar radiation by 1 W m^{-2} would lead to an 0.6-1.1 °C increase in global-mean surface temperatures (*Soden and Held*, 2006). The amount of solar radiation absorbed or reflected by the Earth depends on the solar zenith angle (ζ), or angle the sun makes with a line perpendicular to the surface. When the sun is low in the sky (high ζ), much of the incident sunlight may be reflected even for a clear sky; when the sun is high in the sky (low ζ), even thick clouds may not reflect most of the incident sunlight. The difference in average zenith angle between the equator and poles is an important reason why the albedo is typically higher at high latitudes.

In order to simulate the average climate of a planet in radiative-convective equilibrium, one must globally average the incident solar radiation, and define either a solar zenith angle which is constant in time, or which varies diurnally (i.e., the sun rising and setting). The top-of-atmosphere incident solar radiation per unit ground area, or insolation I, is simply the product of the solar constant S_0 and the cosine of the solar zenith angle, $\mu \equiv \cos \zeta$:

$$I = S_0 \cos \zeta, \tag{2.1}$$

where the planetary-mean insolation is simply $\langle I \rangle = S_0/4 \approx 342$ W m^{-2} (in this paper, we will denote spatial averages with $\langle x \rangle$ and time averages with $\overline{x}$). A global-average radiative transfer calculation requires specifying both an effective cosine of solar zenith angle μ^*, and an effective solar constant, S_0^*, such that the resulting insolation matches the planetary-mean insolation:

$$\langle I \rangle = S_0/4 = S_0^* \mu^*. \tag{2.2}$$

Matching the mean insolation constrains only the product $S_0^* \mu^*$, and not either parameter individually, so additional assumptions are needed.

The specifics of these additional assumptions are quite important to simulated

climate, because radiative transfer processes, most importantly cloud albedo, depend on μ (e.g., *Hartmann* (1994)). For instance, the most straightforward choice for a planetary-average calculation might seem to be a simple average of μ over the whole planet, including the dark half, so that $S_{0S}^* = S_0$ and $\mu_S^* = 1/4$. However, this simple average would correspond to a sun that was always near setting, only $\sim 15°$ above the horizon; with such a low sun, the albedo of clouds and the reflection by clear-sky Rayleigh scattering would be highly exaggerated. A more thoughtful, and widely used choice, is to ignore the contribution of the dark half of the planet to the average zenith angle. With this choice of daytime-weighted zenith angle, $\mu_D^* = 1/2$, and $S_{0D}^* = S_0/2$.

A slightly more complex option is to calculate the insolation-weighted cosine of the zenith angle, μ_I^*:

$$\mu_I^* = \frac{\int \mu S_0 \mu P(\mu) d\mu}{\int S_0 \mu P(\mu) d\mu}, \tag{2.3}$$

where $P(\mu)$ is the probability distribution function of global surface area as a function of the cosine of the zenith angle, μ, over the illuminated hemisphere. For the purposes of a planetary average, $P(\mu)$ simply equals 1. This can be seen by rotating coordinates so that the north pole is aligned with the subsolar point, where $\mu = 1$; then μ is given by the sine of the latitude over the illuminated northern hemisphere, and since area is evenly distributed in the sine of the latitude, it follows that area is evenly distributed over all values of μ between 0 and 1. Hereafter, when discussing planetary averages, it should be understood that integrals over μ implicitly contain the probability distribution function $P(\mu) = 1$. Evaluation of (2.3) gives $\mu_I^* = 2/3$, and $S_{0I}^* = 3S_0/8$. Since most of the sunlight falling on the daytime hemisphere occurs where the sun is high, μ_I^* is considerably larger than μ_D^*. A schematic comparison of these three different choices – simple average, daytime-weighted, and insolation-weighted zenith angles – is given in Figure 2-1.

The daytime-average cosine zenith angle of 0.5 has been widely used. The early studies of radiative-convective equilibrium by *Manabe and Strickler* (1964), *Manabe and Wetherald* (1967), *Ramanathan* (1976), and the early review paper by *Ramanathan and Coakley* (1978), all took $\mu^* = 0.5$. The daytime-average zenith angle
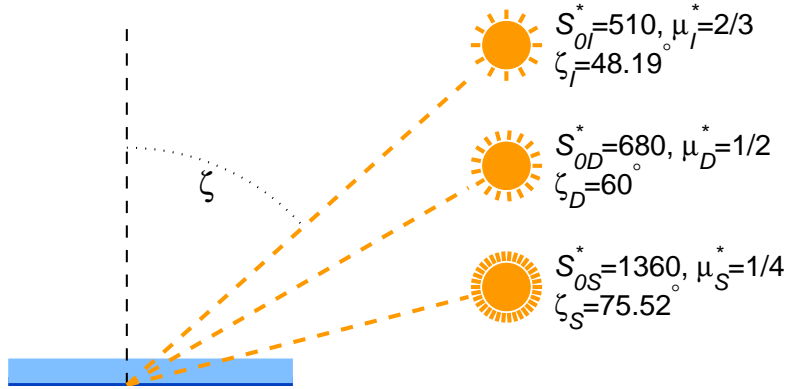
Figure 2-1: Schematic example of three different choices of zenith angle and solar constant that give the same insolation. The solar zenith angle ζ is shown for each of the three choices, which correspond to simple average, daytime-weighted, and insolation-weighted choices of μ, as in the text.

has also been used in simulation of climate on other planets (e.g., *Wordsworth et al.* (2010)), as well as estimation of global radiative forcing by clouds and aerosols (*Fu and Liou*, 1993; *Zhang et al.*, 2013).

To our knowledge, no studies of global-mean climate with single-column models have used an insolation-weighted cosine zenith angle of 2/3. However, the above considerations regarding spatial averaging over variations in insolation also apply to the temporal averaging of insolation that is required to represent the diurnal cycle, or combined diurnal and annual cycles of insolation, with a zenith angle that is constant in time. In this context, *Hartmann* (1994) strongly argues for the use of insolation-weighted zenith angle, and provides a figure with appropriate daily-mean insolation-weighted zenith angles as a function of latitude for the solstices and the equinoxes (see *Hartmann* (1994), Figure 2.8). *Romps* (2011) also uses an equatorial insolation-weighted zenith in a study of radiative-convective equilibrium with a cloud-resolving model; though other studies that have focused on tropical radiative-convective equilibrium, such as the work by *Tompkins and Craig* (1998a), have used a daytime-weighted zenith angle. In large-eddy simulations of marine low clouds, *Bretherton et al.* (2013) advocate for the greater accuracy of the insolation-weighted zenith angle, noting that the use of daytime-weighted zenith angle gives a 20 W m^{-2}

stronger negative shortwave cloud radiative effect than the insolation-weighted zenith angle. Biases of such a magnitude would be especially disconcerting for situations where the surface temperature is interactive, as they could lead to dramatic biases in mean temperatures.

Whether averaging in space or time, an objective decision of whether to use daytime-weighted or insolation-weighted zenith angle requires some known and unbiased reference point. In section 2.2, we develop the idea of absorption-weighted zenith angle as such an unbiased reference point. We show that if albedo depends nearly linearly on the zenith angle, which is true if clouds play a dominant role in solar reflection, then the insolation-weighted zenith angle is likely to be less biased than the daytime-weighted zenith angle. We then calculate the planetary-average absorption-weighted zenith angle for the extremely idealized case of a purely conservative scattering atmosphere. In section 2.3, we perform calculations with a more detailed shortwave radiative transfer model, and show that differences in planetary albedo between $\mu_D^*=1/2$ and $\mu_I^* = 2/3$ can be $\sim3\%$, equivalent to a radiative forcing difference of over 10 W m^{-2}. In section 2.4 we show that the superiority of insolation-weighting also applies for diurnally- or annually-averaged insolation. Finally, in section 2.5, we discuss the implications of our findings for recent studies with global models, and summarize our main findings.

2.2   Absorption-Weighted Zenith Angle

For the purposes of minimizing biases in solar absorption, the zenith angle should be chosen to most closely match the spatial- or time-mean albedo. By this, we do not intend that the zenith angle should be tuned so as to match the observed albedo over a specific region or time period; rather, we wish to formulate a precise geometric closure on (2.2). If the albedo is a known function of the zenith angle (i.e., $\alpha = f_\alpha(\mu) = f_\alpha(\cos\zeta)$), then we can choose a zenith angle, μ_A^*, such that its albedo matches the albedo that would be calculated from a full average over space or time

21

(as weighted by the probability density function $P(\mu)$):

$$f_\alpha(\mu_A^*) \int S_0 \mu P(\mu) d\mu = \int S_0 \mu f_\alpha(\mu) P(\mu) d\mu \qquad (2.4)$$

If the albedo function f_α is smooth and monotonic in the zenith angle – the likely (albeit not universal) case for planetary reflection – then f_α can be inverted, and the problem is well-posed, with a unique solution:

$$\mu_A^* = f_\alpha^{-1} \left[\frac{\int \mu f_\alpha(\mu) P(\mu) d\mu}{\int \mu P(\mu) d\mu} \right], \qquad (2.5)$$

where f_α^{-1} represents the inverse function of f_α. Note that for the case of planetary-average climate, $P(\mu) = 1$, and thus (2.5) simplifies to:

$$\langle \alpha \rangle = 2 \int_0^1 \mu f_\alpha(\mu) d\mu, \qquad (2.6)$$

$$\mu_A^* = f_\alpha^{-1} \left[2 \int_0^1 \mu f_\alpha(\mu) d\mu \right], \qquad (2.7)$$

where $\langle \alpha \rangle$ is the planetary albedo, or ratio of reflected to incident global shortwave radiation. Note that a bias in planetary albedo by 1% would lead to a bias in planetary-average absorbed shortwave radiation of 3.42 W m^{-2}.

If the albedo is a linear function of the zenith angle, we can write:

$$f_\alpha(\mu) = \alpha_{\max} - \alpha_\Delta \mu, \qquad (2.8)$$

where $\alpha_{\max}$ is the maximum albedo (for $\mu = 0$), and α_Δ is the drop in albedo in going from $\mu = 0$ to $\mu = 1$. In this case, we can show that the absorption-weighted zenith angle is exactly equal to the insolation-weighted zenith angle, regardless of the form of $P(\mu)$. From (2.3), (2.4), and (2.8), it follows that:

$$\alpha_{\max} \int \mu P(\mu) d\mu - \alpha_\Delta \mu_A^* \int \mu P(\mu) d\mu = \alpha_{\max} \int \mu P(\mu) d\mu - \alpha_\Delta \int \mu^2 P(\mu) d\mu$$

$$\mu_A^* = \frac{\int \mu^2 P(\mu) d\mu}{\int \mu P(\mu) d\mu} = \mu_I^*. \qquad (2.9)$$

Thus, if the albedo varies roughly linearly with μ, then we expect the insolation-weighted zenith angle to closely match the absorption-weighted zenith angle.

For planetary-average climate, the simplicity of $P(\mu)$ allows us to perform an additional analytic calculation of the absorption-weighted zenith angle. Consider an albedo similar to (2.8), but which may now vary nonlinearly, as some power of the cosine of the zenith angle:

$$f_\alpha(\mu) = \alpha_{\max} - \alpha_\Delta \mu^b. \tag{2.10}$$

The power b is likely equal to or less than 1, so that the albedo is more sensitive to the zenith angle when the sun is low than when the sun is high. For a general value of b, the planetary albedo and absorption-weighted zenith angle are given by:

$$
\begin{aligned}
\langle \alpha \rangle &= \alpha_{\max} - \frac{\alpha_\Delta}{1 + b/2} \\
\mu_A^* &= \left(\frac{1}{1 + b/2} \right)^{1/b}.
\end{aligned}
\tag{2.11}
$$

As noted above, if the albedo depends linearly on μ ($b{=}1$), then the absorption-weighted zenith angle has a cosine of $2/3$, which is equal to to planetary-average value of the insolation-weighted cosine zenith angle (μ_I^*). For $0 < b < 1$, μ_A^* always falls between $e^{-1/2} \approx 0.607$ and $2/3$, suggesting that $\mu_I^* = 2/3$ is generally a good choice for the zenith angle in planetary-mean calculations. The albedo must be a strongly nonlinear function of μ, with significant weight at low μ, in order to obtain values of $\mu_A^* < 0.6$.

2.2.1 Example: A Pure Scattering Atmosphere

How strongly does the planetary albedo depend on μ for a less idealized function $f_\alpha(\mu)$? For a pure conservative scattering atmosphere, with optical thickness τ^*, two-stream coefficient γ (which we will take $=3/4$, corresponding to the Eddington approximation (*Pierrehumbert*, 2010)), and scattering asymmetry parameter $\hat{g}$, *Pier-*

rehumbert (2010) (Eqn. 5.38) gives the atmospheric albedo as:

$$\alpha_a = \frac{(1/2 - \gamma\mu)(1 - e^{-\tau^*/\mu}) + (1 - \hat{g})\gamma\tau^*}{1 + (1 - \hat{g})\gamma\tau^*}. \tag{2.12}$$

Defining a constant surface albedo of α_g, and a diffuse atmospheric albedo α_a', the total albedo is:

$$\alpha = 1 - \frac{(1 - \alpha_g)(1 - \alpha_a)}{(1 - \alpha_g)\alpha_a' + (1 - \alpha_a')}. \tag{2.13}$$

Using this expression, we can calculate how the albedo depends on zenith angle for different sky conditions. Figure 2-2 shows the dependence of the albedo on the cosine of the solar zenith angle, for a case of Rayleigh scattering by the clear sky ($\tau^* \approx 0.12$, $\hat{g} = 0$), for a cloudy-sky example ($\tau^* = 3.92$, $\hat{g} = 0.843$), and for a linear mix of 68.6 % cloudy and 31.4 % clear sky, which is roughly the observed cloud fraction as measured by satellites (*Rossow and Schiffer*, 1999). Values of average cloud optical thickness are taken from *Rossow and Schiffer* (1999), with the optical thickness equal to the sum of cloud and Rayleigh scattering optical thicknesses (3.8 and 0.12, respectively), and the asymmetry parameter set to a weighted average of cloud and Rayleigh scattering asymmetry parameters (0.87 and 0, respectively). Figure 2-2 also shows the appropriate choice of the cosine of the absorption-weighted zenith angle, μ_A^*, for the clear and cloudy-sky examples. The clear-sky case has $\mu_A^* = 0.55$, the cloudy-sky case has $\mu_A^* = 0.665$, and the mixed-sky case has $\mu_A^* = 0.653$. In these calculations, and others throughout the paper, we have fixed the surface albedo to a constant of 0.12, independent of μ, in order to focus on the atmospheric contribution to planetary reflection. The particular surface albedo value of 0.12 is chosen following the observed global mean surface reflectance from Figure 5 of *Donohoe and Battisti* (2011) (average of the hemispheric values from observations). Of course, surface reflection also generally depends on μ, with the direct-beam albedo increasing at lower μ, but surface reflection plays a relatively minor role in planetary albedo, in part because so much of the Earth is covered by clouds (*Donohoe and Battisti*, 2011).

We can also use these results to calculate what bias would result from the use of the daytime-weighted zenith angle ($\mu_D^*=1/2$) or the insolation-weighted zenith
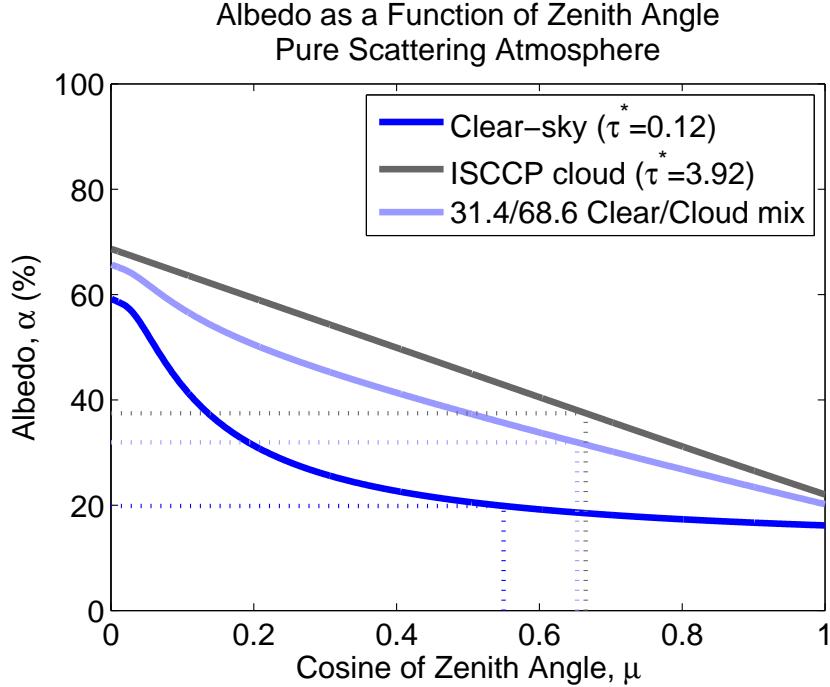
Figure 2-2: Plot of albedo against cosine of the zenith angle, for a pure conservative scattering atmospheric column, based on *Pierrehumbert* (2010), Eqn. (5.41). We show calculations for a clear-sky case with τ^*=0.12 and $\hat{g}$=0 (blue), for a cloudy case, with τ^*=3.92 and $\hat{g}$=0.843 (gray), and a linear mix of the two for a sky that is 68.6 % cloudy and 31.4 % clear (blue-gray). The average cloud fraction and optical thickness are taken after International Satellite Cloud Climatology Project (ISCCP) measurements (*Rossow and Schiffer*, 1999), and the surface albedo is set to a constant of 0.12, independent of μ. The values of the cosines of absorption-weighted zenith angle are indicated by the x-locations of the vertical dotted lines, and the planetary average albedos are indicated by the y-locations of the horizontal dotted lines (see also Table 2.1).

angle (μ_I^*=2/3). The planetary albedo is generally overestimated by use of μ_D^* and underestimated by use of μ_I^*; the first three rows of Table 2.1 summarize our findings for a pure scattering atmosphere. For a clear sky, the daytime-weighted zenith angle is a slightly more accurate choice than the insolation-weighted zenith angle. On the other hand, for a cloudy sky with moderate optical thickness, the insolation-weighted zenith angle is essentially exact, and a daytime-weighted zenith angle may overestimate the planetary albedo by over 7%. For Earthlike conditions, with a mixed sky that has low optical thickness in clear regions, and moderate optical thickness in cloudy regions, a cosine-zenith angle close to but slightly less than the planetary

Table 2.1: Table of planetary albedos and biases.

Radiative Transfer Model	Atmospheric Profile	$\langle \alpha \rangle$ (%)	μ_A^*	Biases in α (%) μ=1/2	μ=2/3
Pure scattering	clear sky	19.9	0.550	0.78	-1.40
Pure scattering	68.6% ISCCP cloud, 31.4% clear	31.9	0.653	5.57	-0.49
Pure scattering	ISCCP cloud	37.4	0.665	7.77	-0.08
RRTM	1976 U.S. Standard - clear	14.1	0.576	0.56	-0.53
RRTM	1976 U.S. Standard - RS99 clouds	34.8	0.657	3.16	-0.19
RRTM	1976 U.S. Standard - Stratocumulus	51.5	0.686	3.53	0.37

insolation-weighted mean value of 2/3 is likely the best choice. The common choice of μ^*=1/2 will overestimate the negative shortwave radiative effect of clouds, while choices of μ^* that are larger than 2/3 will underestimate the negative shortwave radiative effect of clouds. Our calculations here, however, are quite simplistic, and do not account for atmospheric absorption or wavelength-dependent optical properties. In the following section, we will use a more detailed model to support the assertion that the insolation-weighted zenith angle leads to smaller albedo biases than the daytime-weighted zenith angle.

2.3 Calculations with a Full Radiative Transfer Model

The above calculations provide a sense for the magnitude of planetary albedo bias that may result from different choices of average solar zenith angle. In this section, we calculate albedos using version 3.8 of the shortwave portion of the Rapid Radiative Transfer Model, for application to GCMs (RRTMG_SW, v3.8; *Iacono et al.* (2008); *Clough et al.* (2005)); hereafter we refer to this model as simply "RRTM" for brevity. Calculations with RRTM allow for estimation of biases associated with different choices of μ when the atmosphere has more realistic scattering and absorption properties than we assumed in the pure scattering expressions above (2.12), (2.13). RRTM is a broadband, two-stream, correlated k-distribution radiative transfer model, which has been tested against line-by-line radiative transfer models, and is used in several general circulation models (GCMs). For calculation of radiative fluxes in partly cloudy skies, the model uses the Monte-Carlo independent column approximation (McICA; *Pincus et al.* (2003)), which stochastically samples 200 profiles over

26

the prescribed range of combinations of cloud fraction at different vertical levels, and averages the fluxes that result.

We use RRTM to calculate the albedo as a function of zenith angle for a set of built-in reference atmospheric profiles, and several cloud profile assumptions. The atmospheric profiles we use are the Tropical atmosphere, the 1976 U.S. Standard Atmosphere, and the Subarctic Winter atmosphere, and we perform calculations with clear skies, as well as two cloud profile assumptions (Table 2.2). One cloud profile is a mixed sky, intended to mirror Earth's climatological cloud distribution, with four cloud layers having fractional coverage, water path, and altitudes based *Rossow and Schiffer* (1999); we call this case "RS99". The other cloud profile is simply fully overcast with a low-level "Stratocumulus" cloud deck, having a water path of 100 g/m². Table 2.2 gives the values for assumed cloud fractions, altitudes, and in-cloud average liquid and ice water in clouds at each level. Cloud fractions have been modified from Table 4 of *Rossow and Schiffer* (1999) because satellites see clouds from above, and will underestimate true low cloud fraction that is overlain by higher clouds. If multiple cloud layers are randomly overlapping, and seen from above, then, indexing cloud layers as (1,2,...) from the top down, we denote $\hat{\sigma}_i$ as the observed cloud fraction in layer i, and σ_i as the true cloud fraction in layer i. Then the true cloud fraction in layer i is:

$$\sigma_i = \hat{\sigma}_i \left(1 - \sum_{j=1}^{i-1} \hat{\sigma}_j \right)^{-1}, \tag{2.14}$$

which can be seen because the summation gives the fraction of observed cloudy sky above level i, so the term in parentheses gives the fraction of clear sky above level i, which is equal to the ratio of observed cloud fraction to true cloud fraction in layer i (again assuming random cloud overlap). Applying this correction to observed cloud fractions $(\hat{\sigma}_1, \hat{\sigma}_2, \hat{\sigma}_3, \hat{\sigma}_4)$=(0.196, 0.026, 0.190, 0.275) from Table 4 of *Rossow and Schiffer* (1999) gives the cloud fractions listed in Table 2.2: $(\sigma_1, \sigma_2, \sigma_3, \sigma_4)$=(0.196, 0.032, 0.244, 0.467).

To isolate the contributions from changing atmospheric (and especially cloud)

Table 2.2: Cloud profiles used in calculations with RRTM. The multiple cloud layers of *Rossow and Schiffer* (1999) are used together, and are assumed to overlap randomly. Cloud fractions are based on Table 4 of *Rossow and Schiffer* (1999), but adjusted for random overlap and observation from above (see text). Cloud-top altitudes are based on top pressures from *Rossow and Schiffer* (1999) and pressure-height profile from 1976 U.S. Standard Atmosphere. Cloud water/ice allocation uses 260 K as a threshold temperature.

Cloud Profile	fraction (-)	top altitude (km)	water path (g/m^2)	ice path (g/m^2)
Rossow and Schiffer (1999) RS99 low	0.475	2	51	0
Rossow and Schiffer (1999) RS99 medium	0.244	5	0	60
Rossow and Schiffer (1999) RS99 convective	0.032	9	0	261
Rossow and Schiffer (1999) RS99 cirrus	0.196	10.5	0	23
Stratocumulus	1.0	2	100	0

albedo as a function of μ, the surface albedo is set to a value of 0.12 for all calculations, independent of the solar zenith angle. Using RRTM calculations of albedo at 22 roughly evenly-spaced values of μ, we interpolate $f_\alpha(\mu)$ to a grid in μ with spacing 0.001, calculate the planetary albedo $\langle\alpha\rangle$ from equation (2.6), and find the value of μ_A^* whose albedo most closely matches $\langle\alpha\rangle$. The dependence of albedo on μ is shown in Figure 2-3; atmospheric absorption results in generally lower values of albedo than in the pure scattering cases above, as well as lower sensitivity of the albedo to zenith angle. For partly or fully cloudy skies, the albedo is approximately linear in the zenith angle. Note that $f_\alpha(\mu)$ here is not necessarily monotonic, as it decreases for very small μ. This implies that the inverse problem can return two solutions for μ_A^* in some cases; we select the larger result if this occurs.

For clear skies, biases in $\langle\alpha\rangle$ are nearly equal in magnitude for μ_D^* and μ_I^* (Table 2.1). For partly cloudy or overcast skies, however, biases in $\langle\alpha\rangle$ are much larger for μ_D^* than for μ_I^*; the insolation-weighted zenith angle has an albedo bias that is lower by an order of magnitude than the albedo bias of the daytime-weighted zenith angle. The bias in solar absorption for partly-cloudy or overcast skies for μ_D^* is on the order of 10 W m^{-2}. While we have only tabulated biases for the 1976 U.S. Standard Atmosphere, results are similar across reference atmospheric profiles.
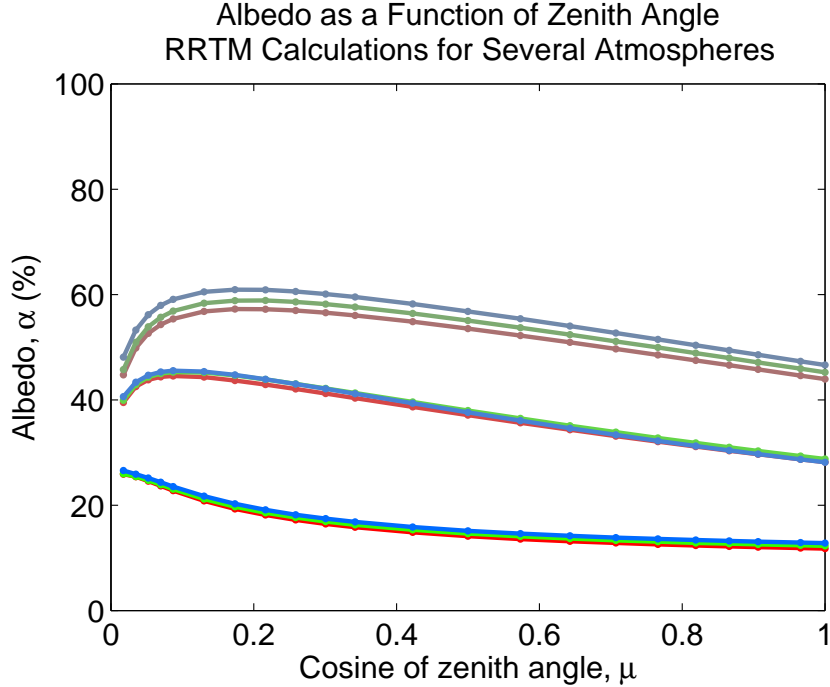
28

Figure 2-3: Plot of albedo against cosine of the zenith angle, for calculations from RRTM. Albedo is shown for three atmospheric profiles: Tropical (red), 1976 U.S. Standard (green), and Subarctic winter (blue). We also show results for clear-sky radiative transfer (bottom set of lines), as well two cloud profile assumptions: observed RS99 cloud climatology (middle set of lines), and Stratocumulus overcast (upper set of lines) – see Table 2.2 for more details on cloud assumptions. The surface albedo is set to a constant of 0.12 in all cases, independent of μ.

2.4   Diurnal and Annual Averaging

Thus far, we have presented examples of albedo biases only for the case of planetary-mean calculations. The absorption-weighted zenith angle can also be calculated and compared to daytime-weighted and insolation-weighted zenith angles for the case of diurnal- or annual-average solar radiation at a single point on the Earth's surface, using (2.5). The latitude and temporal averaging period both enter into the calculation of the probability density function $P(\mu)$, as well as the bounds of the integrals in (2.5). We will look at how μ_A^* varies as a function of latitude for two cases: an equinoctial diurnal cycle and a full average over annual and diurnal cycles. In both cases, we will use $f_\alpha(\mu)$ as calculated by RRTM, for the 1976 U.S. Standard Atmosphere, and the mixed-sky cloud profile of RS99.

For an equinoctial diurnal cycle at latitude ϕ, the cosine of the zenith angle is given by $\mu(h) = \cos\phi\cos(\pi(h-12)/12)$, where h is the local solar time in hours. Since time (h) is uniformly distributed, this can be analytically transformed to obtain the probability density function $P(\mu)$:

$$P(\mu) = \frac{2}{\pi\sqrt{\cos^2\phi - \mu^2}}, \tag{2.15}$$

which is valid for $0 \leq \mu < \cos\phi$. For the equinoctial diurnal cycle, daytime-weighting gives $\mu_D^* = (2/\pi)\cos\phi$, while insolation-weighting gives $\mu_I^* = (\pi/4)\cos\phi$. Figure 2-4 shows that the absorption-weighted zenith angle is once again much closer to the insolation-weighted zenith angle than to the daytime-weighted zenith angle for partly cloudy skies. We can also look at how the time-mean albedo $\overline{\alpha}$ compares to the albedo calculated from μ_D^* or μ_I^*. Albedo biases at the equator are -0.2% for insolation-weighting, and +2.6% for daytime-weighting, which translates to solar absorption biases of +0.9 W m^{-2} and -11.2 W m^{-2}, respectively. For clear-sky calculations (not shown), results are also similar to what we found for planetary-average calculations: the two choices are almost equally biased, with albedo underestimated by $\sim$0.5% when using μ_I^*, and overestimated by $\sim$0.5% when using μ_D^*.

For the full annual and diurnal cycles of solar insolation, $P(\mu)$ must be numerically tabulated. For each latitude band, we calculate μ every minute over a year, and construct $P(\mu)$ histograms with bin width 0.001 in μ; then we calculate the insolation-weighted, daytime-weighted, and absorption weighted cosine zenith angles and corresponding albedos (Figure 2-5). For partly cloudy skies, the insolation-weighted zenith angle is a good match to the absorption-weighted zenith angle, with biases in albedo of less than 0.2%. Albedo biases for the daytime-weighted zenith angle are generally $\sim$2-3%, with a maximum of over 3% around 60 degrees latitude. The solar absorption biases at the equator are similar to those found in the equinoctial diurnal average, though slightly smaller. Overall, these findings indicate that insolation-weighting is generally a better approach than daytime-weighting for representing annual or diurnal variations in solar insolation.
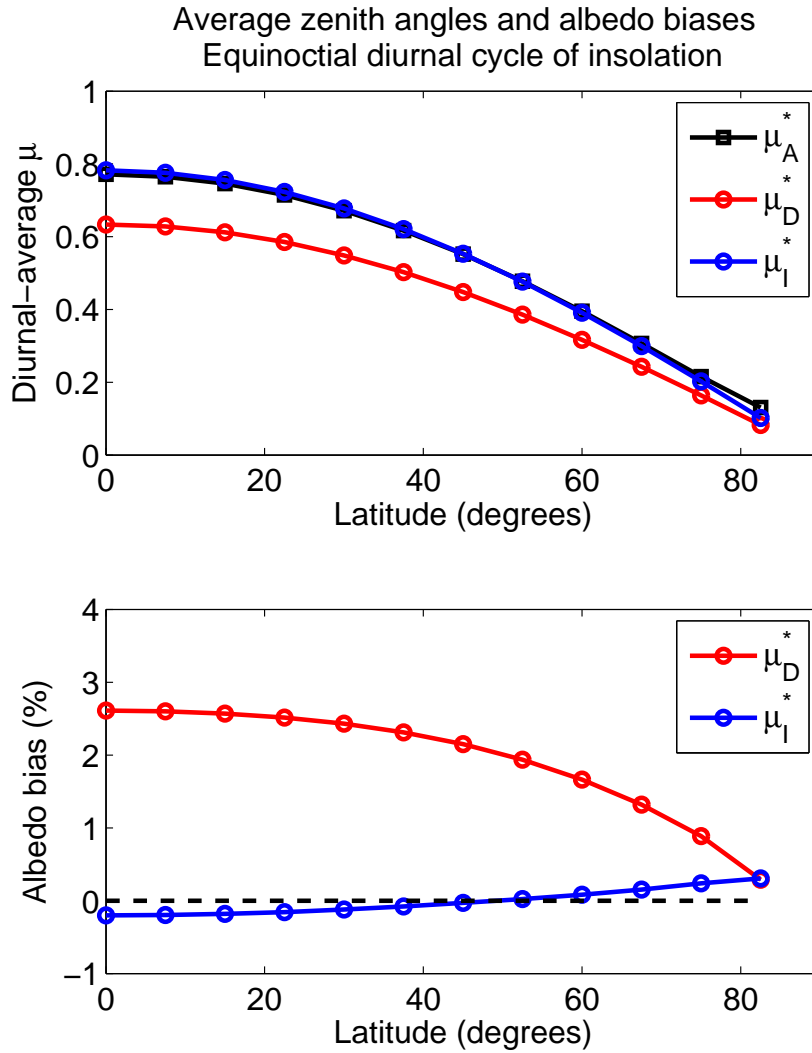
Figure 2-4: Plot of diurnal-average zenith angles (top), and biases in time-mean albedo (bottom) for equinoctial diurnal cycles, as a function of latitude. Albedo is calculated in RRTM, using the 1976 U.S. Standard Atmosphere and RS99 clouds (Table 2.2). Albedo biases for the daytime-weighted zenith angle (μ_D^*, red) and the insolation-weighted zenith angle (μ_I^*, blue) are calculated relative to the absorption-weighted zenith angle (μ_A^*, black).

Figure 2-5: Plot of annual-average zenith angles (top), and biases in time-mean albedo (bottom) for full annual and diurnal cycles of solar insolation, as a function of latitude. Albedo is calculated in RRTM, using the 1976 U.S. Standard Atmosphere and RS99 clouds (Table 2.2). Albedo biases for the daytime-weighted zenith angle (μ_D^*, red) and the insolation-weighted zenith angle (μ_I^*, blue) are calculated relative to the absorption-weighted zenith angle (μ_A^*, black).

2.5   Discussion and Conclusions
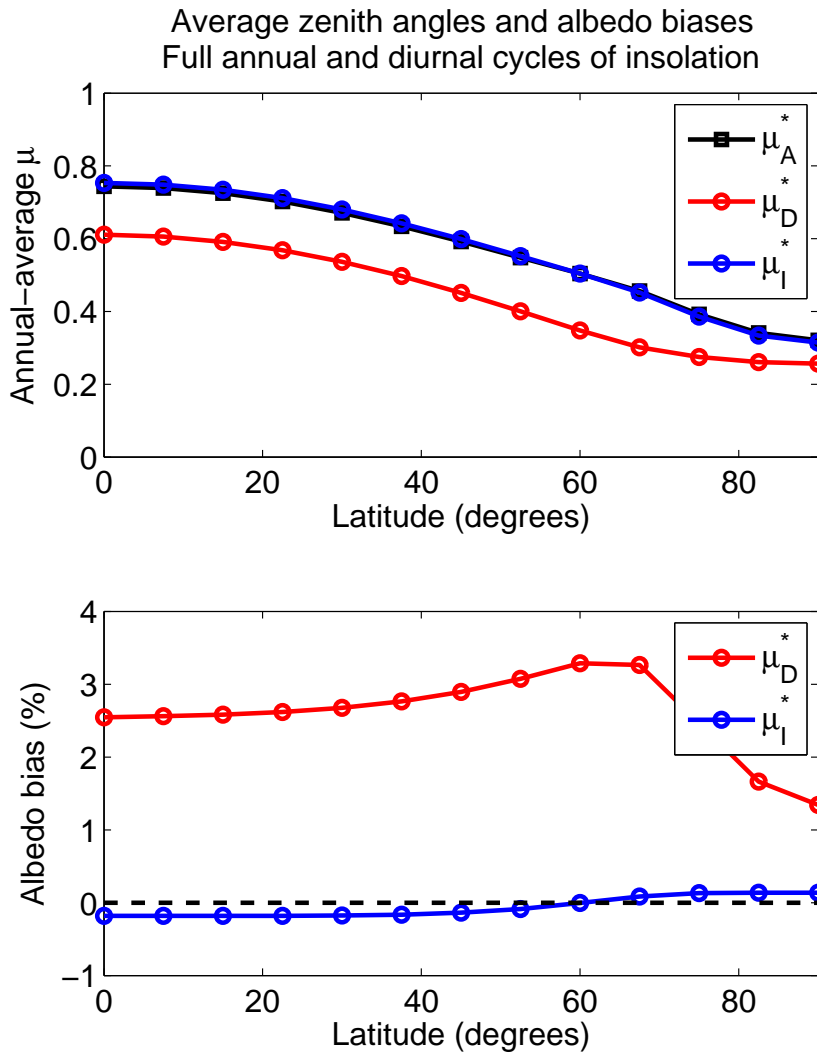
The work presented here addresses potential climate biases in two major lines of inquiry in climate science. One is the use of single-column models in radiative-convective equilibrium as a tool to simulate and understand important aspects of planetary-mean climate, such as surface temperature and precipitation. The second is the increasing use of idealized three-dimensional general circulation models (GCMs) for understanding large-scale atmospheric dynamics. Both of these categories span a broad range of topics, from understanding the limits of the circumstellar habitable zone and the scaling of global-mean precipitation with temperature in the case of single-column models, to the location of midlatitude storm tracks and the strength of the Hadley circulation in the case of idealized GCMs. Both categories of model often sensibly choose to ignore diurnal and annual variations in solar insolation, so as to reduce simulation times and avoid unnecessary complexity. Our work suggests that spatial or temporal averaging of solar radiation, however, can lead to biases in total absorbed solar radiation on the order of 10 W m^{-2}, especially if the models used have a large cloud area fraction.

Single column models are a valuable tool for understanding the controls on global-mean surface temperature, and its sensitivity to forcing by changes in solar radiation or greenhouse gases. The extent to which a single-column model with unbiased planetary albedo and relative humidity, accurately captures the global-mean surface temperature of both the real Earth, and more complex three-dimensional GCMs, is a key test of the magnitude of nonlinearities in the climate system. For instance, variability in tropospheric relative humidity, as induced by large-scale vertical motions in the tropics, can give rise to dry-atmosphere "radiator fin" regions that emit longwave radiation to space more effectively than would a horizontally uniform atmosphere, resulting in a cooling of global mean temperatures relative to a reference atmosphere with homogeneous relative humidity (*Pierrehumbert*, 1995). The relative and absolute importance of nonlinearities such as these subtropical "radiator fins," or impacts of ice on planetary albedo, or interactions between clouds and large-scale dynamics,

or spatiotemporal variability in lapse rates, represents a fundamental and unanswered question in climate science, in part because single-column models have generally been tuned in ways that makes unbiased comparison of their absolute temperature with global models difficult.

The recent work of *Popke et al.* (2013) elegantly seeks to bridge this gap, by using a global model (ECHAM6) with uniform insolation, and no rotation. They thus simulate planetary radiative-convective equilibrium over a slab ocean, allowing for organization of convection and circulations up to planetary scales. One of their findings that deserves more explanation is that their planetary albedo is $\sim$0.2, much lower than the observed value of 0.3 (e.g., *Hartmann* (1994)), and surface temperatures are $\sim$28 °C, substantially warmer than the observed surface temperatures of $\sim$14 °C. The warm temperatures and nonrotating dynamics prompt comparison of their simulated cloud and relative humidity distributions to the Earth's Tropics, but the basic question of why albedo is so low, and temperatures so warm, goes largely unanswered. While part of the answer is likely their low value of surface albedo (0.07), our work also suggests that their use of a uniform equatorial equinox diurnal cycle, with $\mu_I^* = \pi/4$, may underestimate cloud and clear-sky albedo. For RS99 clouds and an equatorial equinox diurnal cycle, we estimate a time-mean albedo of 32.7%; the same cloud field would give a planetary albedo of 34.6% if the planetary-average insolation-weighted cosine zenith angle of 2/3 were used. Thus, we estimate that the shortwave absorption in *Popke et al.* (2013) may be biased by $\sim$6.7 W m^{-2}.

Previous simulations by *Kirtman and Schneider* (2000), and *Barsugli et al.* (2005) also found very warm global-mean temperatures when insolation contrasts were removed, though planetary rotation was retained in both studies. *Kirtman and Schneider* (2000) found a global-mean surface temperature of 26 °C with a reduced global-mean insolation of only 315 W m^{-2}; realistic global-mean insolation led to too-warm temperatures and numerical instability. *Kirtman and Schneider* (2000) offer little explanation for the extreme warmth of their simulations, but apparently also chose to homogenize radiation by using an equatorial equinox diurnal cycle, with $\mu_I^* = \pi/4$. *Barsugli et al.* (2005) obtained a global-mean surface temperature of $\sim$38 °C when us-

ing a realistic global-mean insolation of 340 W m^{-2}. Similarly to *Popke et al.* (2013), *Barsugli et al.* (2005) also invoke a low planetary albedo of 0.21 as a plausible reason for their global warmth, and explain their low albedo as a consequence of a dark all-ocean surface. This work, however, suggests that their unphysical use of constant $\mu = 1$ may lead to a large albedo bias on its own. For RS99 clouds, we estimate an albedo of 28.8% for μ=1, as compared to 34.6% for μ=2/3, so their albedo bias may be as large as -5.8%, with a resulting shortwave absorption bias of +19.8 W m^{-2}. Application of these three studies (*Kirtman and Schneider*, 2000; *Barsugli et al.*, 2005; *Popke et al.*, 2013) to ask questions about the importance of climate nonlinearities may thus be impeded by biases in planetary albedo and temperature due to a sun that is too high in the sky. While it was not the primary focus of these studies to query the importance of climate nonlinearities, these studies nonetheless serve as a reminder that care is required when using idealized solar geometry in models.

Our work here has focused on matching the top-of-atmosphere absorbed shortwave radiation, but this does not guarantee unbiased partitioning into atmospheric and surface absorption. Because global-mean temperatures are quite sensitive to planetary albedo, we have focused in this work on matching the top-of-atmosphere shortwave absorption, but our methods could easily be extended to match some other quantity instead, such as the shortwave radiation absorbed by the surface. Based on our calculations with RRTM, it appears that a single value of $\mu{\sim}0.58$ will give both the correct planetary albedo and the correct partitioning of absorbed shortwave radiation for clear skies; however, for partly cloudy or overcast skies, a single value of μ cannot simultaneously match both the planetary albedo and the partitioning of absorbed shortwave radiation. Together with the correspondence between global precipitation and free-tropospheric radiative cooling (e.g., *Takahashi* (2009)), the dependence of atmospheric solar absorption on zenith angle suggests that idealized simulations could obtain different relationships between temperature and precipitation due solely to differences in solar zenith angle.

Finally, we note that the use of an appropriately-averaged solar zenith angle still has obvious limitations. Any choice of insolation that is constant in time cannot hope

to capture any covariance between albedo and insolation, which might exist due to diurnal or annual cycles of cloud fraction, height, or optical thickness. Furthermore, use of an absorption-weighted zenith angle will do nothing to remedy model biases in cloud fraction or water content that arise from the model's convection or cloud parameterizations. We hope that the methodology and results introduced in this paper will mean that future studies make better choices with regards to solar zenith angle averaging, and thus will not convolute real biases in cloud properties with artificial biases in cloud radiative effects that are solely related to zenith angle averaging.

Chapter 3

The Climate Time Scale in the Approach to Radiative-Convective Equilibrium

Abstract

In this paper, we discuss the importance of the surface boundary condition (fixed versus interactive surface temperature) for the long time scale of approach to Radiative-Convective Equilibrium (RCE). Using a simple linearized two-variable model for surface-atmosphere interaction, we derive an analytic expression for τ_C, a long climate relaxation time scale that remains well-defined and much longer than either mixing time scale of *Tompkins and Craig* (1998b), even in the limit that the heat capacity of the surface vanishes. We show that the size of τ_C is an intrinsic property of the coupling between the atmosphere and surface, and not a result of the thermal inertia of the surface alone. When the surface heat capacity is low, τ_C can be several times longer than expected, due to the effects of moisture on the effective heat capacity of the atmosphere. We also show that the theoretical expression for τ_C is a good predictor of best-fit exponential relaxation time scales in a single-column model with full physics, across a range of surface temperatures and surface heat capacities.

3.1 Introduction

Study of Radiative-Convective Equilibrium (RCE) has been foundational in our understanding of sensitivity and stability of planetary climates, and also forms the backbone of our understanding of the basic state of Earth's tropical atmosphere. The early studies of *Manabe and Strickler* (1964) and *Manabe and Wetherald* (1967), while simplistic in many ways, established quantitative estimates of the sensitivity of Earth's surface temperature to increased greenhouse gas concentrations that continue to be within the uncertainty ranges of modern general circulation models. In these studies, as well as others where changes in surface or near-surface air temperature are of primary concern, the surface temperature must be included as a prognostic variable, and surface energy balance must hold at equilibrium, in some cases including a term for prescribed subsurface heat flux convergence.

In a different context, the basic state of the tropical atmosphere has often been characterized by the assumption of RCE. Especially with the growing ability to (marginally) resolve deep convection, and the influential papers of *Held et al.* (1993) and *Tompkins and Craig* (1998a), many studies of RCE and the tropical atmosphere have opted to fix the surface temperature as a boundary condition, rather than treat it as a prognostic variable. This means that surface energy balance no longer holds, since the surface implicitly acts as an energy source or sink that adjusts in magnitude exactly as needed to hold surface temperatures fixed. *Tompkins and Craig* (1998b) explored the importance of different time scales in RCE with a fixed surface temperature, and established the importance of two mixing time scales: a fast ($\sim$2 day) time scale related to the cumulus updraft mass flux, and a slow ($\sim$20 day) time scale governed by the radiative-subsidence speed and the depth of the convecting layer.

However, the time scale of approach to RCE is much longer if the surface temperature is interactive. *Manabe and Wetherald* (1967) found relaxation time scales of $\sim$ 100 days, and pointed out that the approach to equilibrium at constant relative humidity takes longer than the approach at constant specific humidity, due not only to the impacts of water vapor as a greenhouse gas, but also to the internal

latent energy of moist air. *Held and Suarez* (1974) noted that a fundamental time scale for equilibration of planetary climate is given by the 'radiative relaxation time scale', $\tau_C = C/B$, where C is the heat capacity of a column of the atmosphere [units: J/m^2/K], and B is the change in the flux of net upward radiation at the top of the atmosphere per unit change in atmospheric temperature [units: W/m^2/K]. The time scale τ_C may be increased by inclusion of the heat capacity of the mixed layer of the ocean, which increases C, or by positive feedbacks in the climate system, which decrease B (*Held and Suarez*, 1974; *Wetherald and Manabe*, 1975). While it may seem obvious that this climate time scale τ_C is the relevant relaxation time scale towards RCE with an interactive surface, this point appears rarely in discussion of RCE, and deserves to be made more explicitly. The size of τ_C relative to the time scales of *Tompkins and Craig* (1998b) is especially germane given recent studies with cloud-resolving models that have used interactive sea surface temperatures. Neither the study of *Romps* (2011) (which is well-equilibrated), nor the study of *Khairoutdinov and Yang* (2013) (which is not), invoke τ_C as an explanation for the duration of a simulation that is required to reach equilibrium.

The goal of this paper is thus to clarify more explicitly the scaling behavior of the time scale τ_C in RCE with an interactive surface. In section 3.2, we use a simple coupled two-variable surface-atmosphere model to derive τ_C, and show that it can easily be an order of magnitude larger than the slow mixing time scale of *Tompkins and Craig* (1998b). We also find that the effective heat capacity of the atmosphere, C_A, which is relevant for the transition from one RCE state to another, can be considerably larger than the heat capacity of the dry troposphere, due to both internal latent energy and lapse rate considerations (section 3.2.1). In section 3.3, we perform simulations with a single-column model, and show that best-fit relaxation time scales are predicted quite well by τ_C.

3.2 Theory

To show that τ_C is a relevant time scale for a coupled atmosphere-surface system, we start from a simple two-variable model of atmosphere-surface interaction, which is linearized about a basic state that is in radiative-convective equilibrium (RCE, see the schematic in Figure 3-1). We construct perturbation equations for the temperature anomalies of the near-surface atmosphere, T_A', and of the surface, T_S', about basic-state values (T_A, T_S), assuming that C_A is the effective heat capacity of the troposphere, and that C_S is the heat capacity of a slab of water representing the surface (both have units of J/m^2/K). We also assume that the tropospheric relative humidity stays roughly constant as the temperature of the troposphere changes, so that T_A' is accompanied by a boundary layer specific humidity perturbation $q' = T_A' \mathcal{H} \left. (\partial q^*/\partial T) \right|_{T_A}$, where $\mathcal{H}$ is the near-surface relative humidity, and q^* is the saturation specific humidity. If the lower troposphere is opaque in the infrared, and the emission level for downwelling infrared radiation is close to the surface, then the linearization coefficients for the longwave radiative flux perturbation due to T_A' and T_S' are approximately equal in magnitude and opposite in sign. If we also follow *Barsugli and Battisti* (1998) and assume the total surface latent plus sensible heat flux linearization coefficients are equal in magnitude and opposite in sign for T_A' and T_S', then the total surface-atmosphere energy flux perturbation from the sum of changes in longwave radiation, plus latent and sensible turbulent exchange, can be parameterized by a single coefficient λ [units: W/m^2/K]. The change in outgoing longwave radiation at the top of the atmosphere per unit change in surface air temperature (i.e., the inverse of the climate sensitivity) is given by the parameter B [units: W/m^2/K], which incorporates the water vapor feedback because of our assumption of constant relative humidity (the lower troposphere is opaque to longwave radiation, so T_S' does not directly affect the top-of-atmosphere energy balance). Finally, we assume minimal changes in shortwave radiative fluxes with temperature (e.g., no shortwave cloud-radiation feedbacks). Our
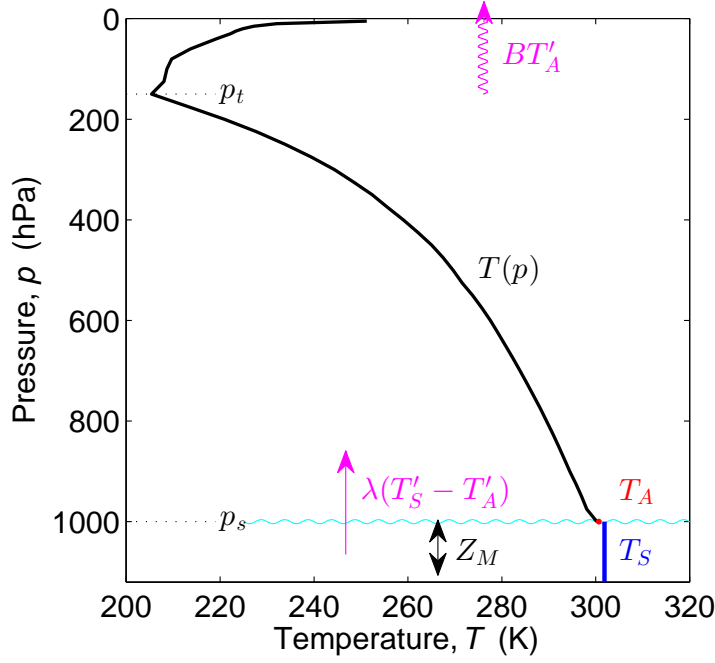
Figure 3-1: Schematic diagram of two-variable model for atmosphere-surface interaction in radiative-convective equilibrium. The surface air temperature, T_A, is the control variable for the atmosphere. Magenta lines indicate perturbation energy fluxes from the surface to the atmosphere, and from the atmosphere to space.

equations for T'_A and T'_S are then given by:

$$\begin{aligned} C_A\dot{T}'_A &= \lambda(T'_S - T'_A) - BT'_A \\ C_S\dot{T}'_S &= \lambda(T'_A - T'_S), \end{aligned} \tag{3.1}$$

where $\dot{x}$ denotes the time-derivative of x. Many of the assumptions in the derivation of (3.1) have been made for the purposes of the simplicity of subsequent algebra, and the general conclusions are robust to a more complex linearization that allows for shortwave cloud feedbacks, coefficients for perturbation latent heat flux that are unequal in magnitude, and a lower troposphere that is non-opaque in the infrared. The application of (3.1) in the presence of cloud radiative feedbacks will be discussed briefly in Section 3.4.

If either T'_A or T'_S is fixed in (3.1), the relaxation time scales are very simple. If

T'_S is held fixed, then T'_A decays towards $[\lambda/(\lambda + B)]T'_S$ with a time scale τ_A:

$$\tau_A = C_A/(\lambda + B). \tag{3.2}$$

On the other hand, if T'_A is held fixed, then T'_S decays towards T'_A with a time scale τ_S:

$$\tau_S = C_S/\lambda. \tag{3.3}$$

The coupled system can be expressed in matrix form as:

$$\begin{bmatrix} \dot{T}'_A \\ \dot{T}'_S \end{bmatrix} = \begin{pmatrix} -1/\tau_A & \eta/\tau_A \\ 1/\tau_S & -1/\tau_S \end{pmatrix} \times \begin{bmatrix} T'_A \\ T'_S \end{bmatrix}, \tag{3.4}$$

where η is the nondimensional ratio $\lambda/(\lambda + B)$. The relaxation time scales of the coupled system (3.1) are given by the eigenvalues r of the matrix in (3.4):

$$2r = -\left(\frac{1}{\tau_A} + \frac{1}{\tau_S}\right) \pm \left[\left(\frac{1}{\tau_A} + \frac{1}{\tau_S}\right)^2 - 4\frac{1-\eta}{\tau_A \tau_S}\right]^{1/2}. \tag{3.5}$$

Both values of r are negative and real, so the system is stable and nonoscillatory; the longer relaxation time scale τ_C corresponds to the smaller absolute value of r ($\tau_C = |r|^{-1}$), which occurs for the $+\sqrt{()}$ solution. Since the second term in the discriminant in (3.5) is much smaller in magnitude than the first, the binomial approximation can be applied to the radical; along with replacement of $(1 - \eta)^{-1}$ with $(\lambda + B)/B$, this results in a great deal of simplification:

$$\tau_C \approx \frac{\lambda + B}{B}(\tau_A + \tau_S). \tag{3.6}$$

It is worth noting that the long time scale τ_C is strictly greater than the sum of the two time scales $\tau_A + \tau_S$, and is typically larger by an order of magnitude; taking $\lambda \sim$ 40 W/m^2/K, and $B \sim 2$ W/m^2/K (e.g., *Nilsson and Emanuel* (1999)), we would have $\tau_C = 21(\tau_A + \tau_S)$! The mode of variability that experiences this long decay timescale corresponds to same-signed and nearly equal perturbations in T_A and T_S;

the more rapidly damped mode (which we will not discuss) corresponds to opposite-signed perturbations in T_A and T_S, which have nearly equal magnitudes of stored energy. Although it may appear from (3.6) that τ_C depends strongly on λ, plugging in (3.2) and (3.3) reveals that:

$$\tau_C \approx B^{-1}(C_A + C_S) + \lambda^{-1}C_S. \tag{3.7}$$

In general, $\lambda \gg B$, so τ_C can be approximated as $(C_A + C_S)/B$.

3.2.1 Effective Tropospheric Heat Capacity

The impacts of moisture can make C_A several times larger than the dry heat capacity of the troposphere, and can thus lead to a large increase in τ_C as temperature increases. The dry heat capacity of the troposphere is given by:

$$C_{A,\mathrm{dry}} = c_p(p_s - p_t)/g, \tag{3.8}$$

where p_s is the surface pressure, p_t the tropopause pressure, and c_p is the specific heat of dry air at constant pressure. For a tropopause around 200 hPa, $C_{A,\mathrm{dry}} \approx 8.2 \times 10^6$ J/m^2/K. However, (3.1) was based on energy conservation, so a more rigorous definition of C_A is given by:

$$C_A \equiv \frac{\partial \langle k \rangle}{\partial T_A}, \tag{3.9}$$

where $\langle k \rangle$ is the tropospheric integral of the moist enthalpy [units: J/m^2]:

$$\langle k \rangle = \int_{p_t}^{p_s} (c_p T + L_v q)dp/g = \langle c_p T \rangle + \langle L_v q \rangle. \tag{3.10}$$

As recognized by the early study of *Manabe and Wetherald* (1967), the assumption of constant relative humidity results in a substantial increase in C_A, because the latent heat capacity of the troposphere, $\partial \langle L_v q \rangle / \partial T_A$, can be large compared to $C_{A,\mathrm{dry}}$, especially at warm temperatures. We can estimate the magnitude of the latent heat capacity of the troposphere by multiplying a typical tropical value of column water

vapor $\langle q \rangle \sim 50$ kg/m^2 by L_v and by the fractional rate of change of specific humidity with temperature, $\sim 7\%$/K, which gives $\partial \langle L_v q \rangle / \partial T_A \approx 8.75 \times 10^6$ J/m^2/K. For tropical temperatures, the latent heat capacity of the troposphere can be comparable to, or larger than, the dry heat capacity of the troposphere.

We can decompose the latent heat capacity of the troposphere into two components: the first is related to changes in saturation specific humidity with temperature, and the second is related to changes in relative humidity with temperature. As in *Bretherton et al.* (2005), we define $\overline{\mathcal{H}}$ as the column relative humidity:

$$\overline{\mathcal{H}} = \langle q \rangle / \langle q^* \rangle, \tag{3.11}$$

or ratio of total column water vapor, $\langle q \rangle$, to that of a saturated column, $\langle q^* \rangle$. Then the latent heat capacity of the troposphere can be expressed as:

$$\frac{\partial \langle L_v q \rangle}{\partial T_A} = L_v \langle q^* \rangle \frac{\partial \overline{\mathcal{H}}}{\partial T_A} + L_v \overline{\mathcal{H}} \frac{\partial \langle q^* \rangle}{\partial T_A}, \tag{3.12}$$

where we have additionally assumed that the effects of temperature on L_v can be neglected.

Tropospheric moisture also has another consequence that is significant for our understanding of C_A. By constraining the thermal structure of the troposphere to be roughly moist-adiabatic, moist convection amplifies temperature changes in the upper troposphere, relative to temperature changes at the surface. If we define $\overline{T}$ as the mass-weighted average temperature of the troposphere, then $\partial \overline{T} / \partial T_A > 1$; the magnitude of this effect is more difficult to estimate, but $\partial \overline{T} / \partial T_A$ also generally increases at warmer temperatures. Taken together with the impacts of tropospheric latent heat capacity (3.12), the upper-tropospheric amplification of temperature changes implies that:

$$C_A = C_{A,\mathrm{dry}} \left(\frac{\partial \overline{T}}{\partial T_A} + \frac{L_v \langle q^* \rangle}{C_{A,\mathrm{dry}}} \frac{\partial \overline{\mathcal{H}}}{\partial T_A} + \frac{L_v \overline{\mathcal{H}}}{C_{A,\mathrm{dry}}} \frac{\partial \langle q^* \rangle}{\partial T_A} \right), \tag{3.13}$$

where we have normalized all terms by the dry heat capacity of the troposphere ($C_{A,\mathrm{dry}}$). We will use equation (3.13) to diagnose the relative importance of different

aspects of moisture for the effective tropospheric heat capacity in our simulations with a radiative convective model; note that it is only approximate when differentials are replaced by finite differences, since we have ignored correlations between changes in $\overline{\mathcal{H}}$ and changes in $\langle q^* \rangle$. In practice, however, this missing correlation term is negligible. Also, the assumption of constant relative humidity in our derivation of τ_C may seem inconsistent with our allowance for changes in relative humidity in (3.13), but in practice there is little contradiction because changes in relative humidity are quite small.

3.3 Single-Column Simulations

To test our theoretical expression for the long time scale of approach to RCE with an interactive surface, we conduct simulations with the single-column model described in *Emanuel and Sobel* (2013) (originally described in *Renno et al.* (1994), but with the convection scheme of *Emanuel and Zivkovic-Rothman* (1999), and updated radiative transfer code) across a range of solar insolation values $\overline{I}$ and surface heat capacities C_S. We will express the surface heat capacity in terms of the depth of an equivalent mixed layer of liquid water, Z_M; $C_S = c_l Z_M$, where c_l is the volumetric heat capacity of liquid water, $\approx 4.2 \times 10^6$ J/m^3/K. A mixed layer with $Z_M \approx 2$ m has about the same heat capacity as the dry troposphere (as given by $C_{A,\mathrm{dry}}$). For all simulations, we use a CO$_2$ concentration of 300 ppm, a surface albedo of 0.2, and a fixed solar zenith angle whose cosine is 2/3 (equal to the planetary-average, insolation-weighted value). Bulk formulae for surface fluxes use an enthalpy flux coefficient of $c_k = 1.5 \times 10^{-3}$, and a surface wind speed of 5 m/s. The model has 46 levels in the vertical (tropospheric resolution of 25 hPa), and a timestep of 5 minutes. For simplicity, we perform simulations without cloud-radiation interactions.

We first use the RC model to obtain equilibrium soundings, then we perturb the insolation and study the relaxation towards new equilibria. Initial equilibria are calculated from 4000-day simulations with $\overline{I} = (290, 300, 310, 320, 330, 340, 350, 360, 370)$ W/m^2. We perturb each sounding by adding 10 W/m^2 to the initial insolation,

and calculate the best-fit relaxation time scale τ_R towards the new equilibrium temperature T_f, from an initial temperature T_i, using a 3-parameter exponential curve fit in MATLAB ($T_A(t) = T_f + (T_i - T_f) \times e^{-t/\tau_R}$). For each choice of insolation, we perform perturbation simulations across a range of $Z_M = (0.5, 1.0, 2.5, 4.0, 5.0, 6.0, 7.5, 10.0, 15.0, 20.0)$ m.

The set of chosen insolation values results in simulated surface air temperatures that range from slightly below 0°C to slightly over 30°C (Table 3.1 describes the equilibria, and will be discussed over the course of this section). The relaxation time scale fit from RC model perturbation experiments can be as large as several hundred days even when $Z_M = 0.5$ m, and generally increases with both T_A and Z_M (Figure 3-2). One of the most striking features of Figure 3-2 is the large local minimum in relaxation time scale for $T_A \approx$ 10-15 °C. This minimum in τ_R occurs because B, as diagnosed from model output, is a local maximum there (Table 3.1). We suspect that this reflects a numerical issue related to the lack of variability in the model, and the related constraint that important transition levels (e.g., tropopause, boundary layer top) must change in discrete jumps. Regardless of whether the variations in B have physical or numerical origins, they result in changes in the relaxation time scales of the model that closely follow theoretical predictions.

Table 3.1: Table of equilibria for RC model simulations across the range of insolation values $\bar{I}$. Equilibria are a function of $\bar{I}$ only; C_S affects the relaxation time scale but not the properties of the equilibria. Values in row j for B, C_A, and terms in columns (i)-(v), are computed based on finite differences (denoted with δ symbols) between equilibrium states for rows j and $j-1$ (e.g., $B_j = (\text{OLR}_j - \text{OLR}_{j-1})/(T_{A,j} - T_{A,j-1})$). Columns labeled (i)-(v) are based on the decomposition of $C_A/C_{A,\text{dry}}$ given in (3.13).

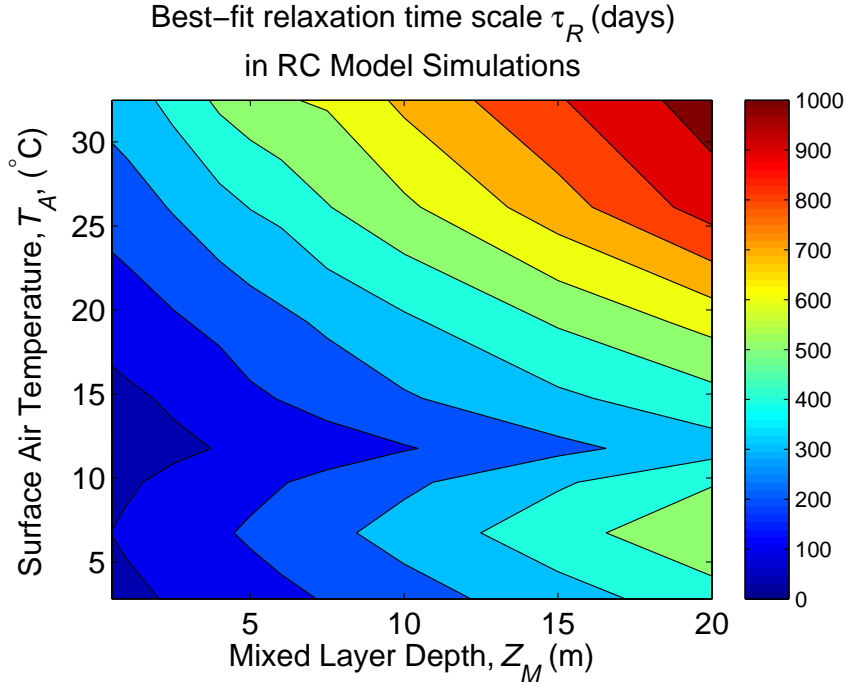| $\bar{I}$ (W/m²)	T_A (°C)	OLR (W/m²)	p_t (hPa)	$\bar{\mathcal{H}}$ (%)	B (W/m²/K)	$\dfrac{\delta\bar{T}}{\delta T_A}$ (i)	$\dfrac{L_v\langle q^*\rangle\delta\bar{\mathcal{H}}}{C_{A,\text{dry}}\delta T_A}$ (ii)	$\dfrac{L_v\bar{\mathcal{H}}\delta\langle q^*\rangle}{C_{A,\text{dry}}\delta T_A}$ (iii)	$\dfrac{L_v\delta\langle q\rangle}{C_{A,\text{dry}}\delta T_A}$ (iv)	$\dfrac{C_A}{C_{A,\text{dry}}}$ (v)	C_A (10^7 J/m²/K)
290	-1.03	232.6	325	61.6							
300	2.81	241.1	300	58.6	2.22	1.13	-0.02	0.15	0.13	1.26	0.90
310	6.73	249.9	275	60.1	2.25	1.19	0.02	0.20	0.21	1.40	1.04
320	9.75	258.5	275	59.0	2.84	1.25	-0.02	0.26	0.24	1.49	1.11
330	11.8	266.9	250	56.7	4.18	1.36	-0.07	0.32	0.24	1.60	1.23
340	14.7	275.3	225	52.7	2.81	1.39	-0.10	0.36	0.26	1.65	1.31
350	19.3	284.2	200	53.2	1.98	1.48	0.01	0.48	0.49	1.97	1.62
360	26.1	293.9	150	62.5	1.42	1.53	0.22	0.79	1.01	2.54	2.21
370	32.5	303.0	100	67.3	1.42	1.51	0.20	1.35	1.55	3.06	2.82

Figure 3-2: Contour plot of best-fit relaxation time scale in days, from RC model simulations.

We diagnose values of B and C_A based on finite differences in temperature, column relative humidity, saturation specific humidity, and outgoing longwave radiation between RC model equilibrium states (see Table 3.1). The theoretical scaling $\tau_C \approx (C_A + C_S)/B$ compares well with best-fit RC model relaxation time scales τ_R, with an R^2 value of 0.95 for a $\tau_C = \tau_R$ fit (Figures 3-3, 3-4). Figures 3-3 and 3-4 show that the theory (τ_C) slightly underestimates best-fit RC model timescales (τ_R), on average. Neglect of the term C_S/λ (from (3.7)) in our simplification of $\tau_C \approx (C_A + C_S)/B$ goes in the right direction, but not far enough, to eliminate the underestimate. Invalidity of the assumptions of the theory, or biased estimation of B and C_A, provide possible reasons for the slight underestimation of τ_R by τ_C. Since the theory captures the bulk of the variance in the relaxation time scale as T_A and C_S are varied, exploration of the small deviations of τ_C from τ_R is left as a topic for future study.

How important are increases in atmospheric heat capacity (C_A) relative to increases in climate sensitivity (B^{-1}) for the increases in relaxation timescale (τ_R) at
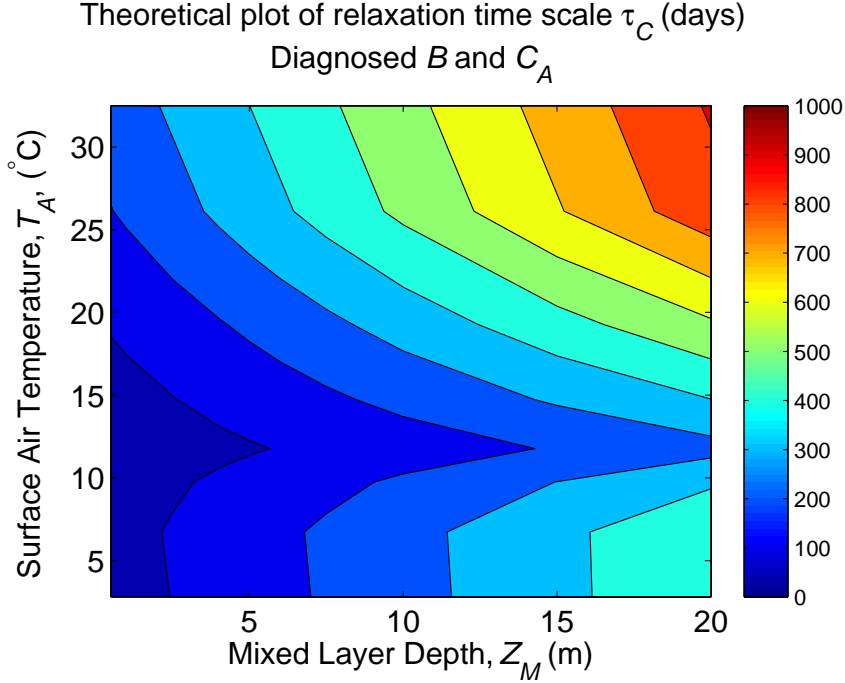
48

Figure 3-3: Contour plot of theoretical relaxation time scales in days, based on values of B and C_A as diagnosed from RC model simulations (see Table 3.1 for values of B and C_A as a function of T_A).

very warm temperatures? What are the largest contributors to the systematic increase in atmospheric heat capacity with temperature? Columns (i)-(iii) of Table 3.1 decompose C_A into the three terms of equation (3.13) (normalized by $C_{A,\mathrm{dry}}$). Column (iv) represents the normalized latent heat capacity of the troposphere, equal to the sum of columns (ii) and (iii), plus the residual term involving correlation between changes in $\overline{\mathcal{H}}$ and changes in $\langle q^* \rangle$; this residual term is very small, with magnitude at most $0.01 C_A/C_{A,\mathrm{dry}}$. Column (v) represents the normalized total heat capacity of the troposphere, or sum of columns (i) and (iv). We see that the dominant contribution to increases in $C_A/C_{A,\mathrm{dry}}$ at very warm temperatures is due to changes in $\langle q^* \rangle$ with T_A, and that changes in column relative humidity are generally a much smaller term than changes in column-integrated saturation specific humidity (see columns (ii) vs. (iii) in Table 3.1). For a range of moderate temperatures, $\sim$ 5-20°C, lapse rate effects contribute most to the elevated values of $C_A/C_{A,\mathrm{dry}}$; $(\partial \overline{T}/\partial T_A - 1)$ is larger than the normalized latent heat capacity of the troposphere (see columns (i) vs. (iv)
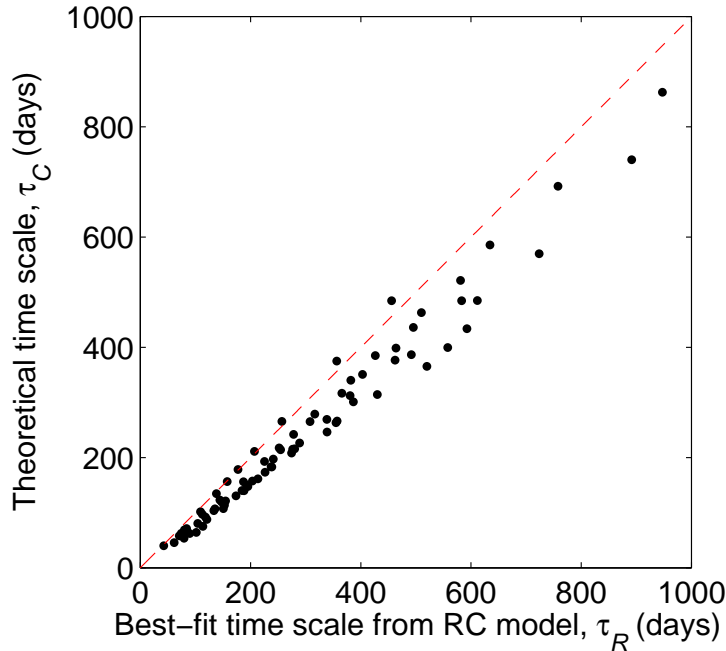
Figure 3-4: Scatter plot of theoretical versus best-fit RC model relaxation time scales (i.e., results from Figures 3-2 and 3-3), in days. Red dashed line indicates the 1-1 line; R^2=0.95 for the model=theory fit.

in Table 3.1). The tropospheric heat capacity is also affected by changes in $C_{A,\mathrm{dry}}$, which occur due to the increase in tropospheric mass as the tropopause rises with warmer temperatures; tropopause pressure p_t is diagnosed as the first level in the model, going upwards, where time-mean radiative is less than 0.05 K/day. Taken in isolation, changes in tropospheric mass are a small factor, but the interaction between changes in tropospheric mass and changes in the ratio $C_A/C_{A,\mathrm{dry}}$ makes the influence of changing tropospheric mass considerably larger. From the coldest to the warmest equilibria, C_A increases by a factor of 3.13, with $C_A/C_{A,\mathrm{dry}}$ increasing by a factor of 2.43, and tropospheric mass increasing by a factor of 1.29. Changes in B are markedly less important than changes in C_A for the systematic increase of τ_C with T_A. For the coldest simulations, $B \approx 2.2$ W/m^2/K, while for the warmest simulations, $B \approx 1.4$ W/m^2/K. Thus increases in B^{-1} only serve to increase τ_C by a factor of $\sim$1.5. For low C_S, increases in C_A with increasing temperature are the dominant contributor to the lengthening of τ_C with warming, specifically due to the large sensitivity of $\langle q^* \rangle$ to

changes in T_A.

3.4 Discussion and Conclusions

We have attempted to clarify that the long time scale of approach to radiative-convective equilibrium with an interactive surface is given by $\tau_C \approx (C_A + C_S)/B$. A close examination of the problem reveals some interesting nuances, especially related to the magnitude of the effective atmospheric heat capacity relative to its dry value. Simulations with a single-column model show good agreement with the theoretical time scale, and highlight our finding that long time scales are not a result of the thermal inertia of the surface alone. A warm atmosphere in RCE has considerable thermal inertia on its own, and can have a relaxation time scale as large as several hundred days even as $C_S \to 0$.

Although we have not explicitly considered cloud-radiation interactions, which are important in many recent studies of radiative-convective equilibrium, the results from the theory turn out to be rather flexible to changes in structural assumptions. Cloud longwave feedbacks could be incorporated into B without any changes to the structure of the theory at all. Cloud shortwave feedbacks would introduce an additional term, DT'_A, into the equation for the evolution of T'_S. This term introduces additional algebra and notation, but so long as D is small compared to λ, $\tau_C \approx (C_A + C_S)/(B - D)$, where $(B - D)$ is a climate sensitivity parameter that incorporates the impact of clouds on shortwave radiation.

The findings from this paper should help to clarify the length of a simulation that is needed to reach equilibrium with an interactive surface temperature. As found by *Khairoutdinov and Yang* (2013), even the ability to perform simulations with a 3D cloud-resolving model for 700 days may not be enough to reach equilibrium with an interactive surface. Since τ_C is a function of both the climate sensitivity, B^{-1}, and the tropospheric heat capacity, C_A, which both generally vary among models, a precise estimate of τ_C depends on the specific behavior of a given model. But determination of B for a given model also seems to require several long simulations with interactive

T_S across a range of forcing conditions. As noted by *Held et al.* (1993), in principle one can resolve this conundrum by conducting simulations across a range of fixed T_S values, and studying the dependence of the net energy flux into the surface on the surface temperature. In practice, this approach seems to be underused as a means of characterizing the sensitivity of 3D cloud-resolving models. Our work points to the value of this approach, even if the ultimate goal is to conduct simulations with an interactive surface.

It is possible that the long relaxation time scale, τ_C, has implications for the interpretation or understanding of climate variability, which have not been fully considered. The two-variable model we have used is very similar to that of *Barsugli and Battisti* (1998), who explored the importance of atmosphere-ocean coupling for the redness of the spectrum of midlatitude climate variability. More recently, and with application to the tropics, *Clement et al.* (2011) suggested that a dynamically active ocean is not necessary to produce interannual- to decadal- time scale variability in the tropical Pacific; an 'ENSO-like' mode of tropical Pacific climate variability appears to operate in many thermally coupled atmosphere-slab ocean models independent of any ocean dynamical response. If variability in the zonal location of convection and T_S anomalies is only weakly damped by heat export to the extratropics, then our work suggests that a null model for such a mode may not need to even invoke large-scale atmospheric dynamics; the long decorrelation time and red spectrum found by *Clement et al.* (2011) for thermally coupled atmosphere-slab ocean models may simply be related to the size of τ_C.

The increase in effective atmospheric heat capacity as temperatures warm may also be relevant to understanding recent findings that global warming can lead to delayed monsoon onset, and an increased lag in the seasonal cycle of tropical precipitation relative to the seasonal cycle of insolation (*Bordoni and Merlis*, 2013; *Dwyer et al.*, 2013). Other things equal, we would expect increased atmospheric heat capacity with warmer temperatures to lead to an increase in the lag between peak solar forcing and peak large-scale ascent and rainfall. The dependence of C_A on temperature may thus provide a simple thermodynamic mechanism to explain delayed monsoon onset in a

warmer climate. Clearly, many of the assumptions of our theory may break down when applied to the seasonal cycle (e.g., seasonal changes in temperature may not occur with a moist-adiabatic vertical structure); we simply wish to suggest here the possibility that systematic changes in tropospheric heat capacity with temperature may be important for understanding the response of the seasonal cycle to climate change.

A final open question relates to the time scales of approach to equilibrium for a coupled surface-atmosphere model where the atmospheric column is constrained by the weak temperature gradient (WTG) approximation (*Sobel et al.*, 2001). A better understanding of the time scales in the WTG atmosphere-land system could be particularly relevant for the important problem of understanding persistence time scales of precipitation anomalies over tropical land.

Chapter 4

A Sensitivity Theory for the Equilibrium Boundary Layer Over Land

Abstract

Due to the intrinsic complexities associated with modeling land-atmosphere interactions, global models typically use elaborate land surface and boundary layer physics parameterizations. Unfortunately, it is difficult to use elaborate models, by themselves, to develop a deeper understanding of how land surface parameters affect the coupled land-atmosphere system. At the same time, it is also increasingly important to gain a deeper understanding of the role of changes in land cover, land use, and ecosystem function as forcings and feedbacks in past and future climate change. To improve the foundation of our understanding, we outline a framework for boundary layer climate sensitivity based on surface energy balance, just as global climate sensitivity is based on top-of-atmosphere energy balance. We develop an analytic theory for the boundary layer climate sensitivity of an idealized model of a diurnally-averaged well-mixed boundary layer over land (*Betts*, 2000). This analytic sensitivity theory identifies changes in the properties of the land surface — including moisture availability, albedo, and aerodynamic roughness — as forcings, and identifies strong negative feedbacks associated with the surface fluxes of latent and sensible heat. We show that our theory

can explain nearly all of the sensitivity of the *Betts* (2000) full system of equations. Favorable comparison of the theory and the simulation results from a two-column radiative convective model suggests that the theory may be broadly useful for unifying our understanding of how changes in land use or ecosystem function may affect climate change.

4.1   Introduction

Global-mean surface air temperature is controlled primarily by planetary energy balance, in which greenhouse gas concentrations and the planetary albedo play a dominant role. Simple models of the sensitivity of planetary energy balance to greenhouse gas concentrations form the foundation of our understanding of how well-mixed greenhouse gases, such as anthropogenic CO_2, affect global climate. Land surface properties, such as moisture availability and roughness, play less of a role in determining the global-mean surface temperature, but they can strongly affect local surface temperatures, with disproportionately large impacts on society. The potential importance of climate change forced by land surface changes ought to be a concern in any comprehensive study of climate change, because the human footprint on the land surface is large, and rapidly changing.

In order to both simulate and understand important problems related to the climate system, *Held* (2005) argues for the importance of model hierarchies, with models that span a range of complexity levels. Since the early and influential studies of *Charney* (1975) and *Shukla and Mintz* (1982), much valuable work has been done to simulate the impacts of the land surface on the climate (and vice-versa) with highly complex General Circulation Models (GCMs). Towards the simpler end of the complexity spectrum, idealized models of the coupled surface-boundary layer system have done a great deal to advance our understanding of land-atmosphere interactions (e.g., *McNaughton and Spriggs* (1986), *Jacobs and De Bruin* (1992), *Brubaker and Entekhabi* (1995), *Kim and Entekhabi* (1998)). One of the central motivations of this work is our belief that the existing model hierarchies in the field of land-atmosphere interactions do not extend down to models that are sufficiently simple so as to be

analytically tractable, and that the lack of analytic models and frameworks impedes the understanding and synthesis of results from more complex models. Despite the large body of work with both simple and complex models, there remains no widely-accepted corollary to climate sensitivity when it comes to understanding the impact of land surface properties on changes in near surface temperatures.

In this study, we attempt to define such a corollary to climate sensitivity, by introducing the framework of boundary layer climate sensitivity. We suggest that daily-average regional temperature response due to changes in surface moisture availability, albedo, and roughness can be understood within a context of forcings and feedbacks, similar to the case of global climate response to a radiative perturbation, but based on surface energy balance, rather than top-of-atmosphere energy balance. Many of the aspects of our work are not new; numerous other studies have used the language of sensitivity theory to describe feedbacks (and occasionally forcings) in the coupled land-atmosphere system. Because of the importance of the diurnal cycle for land-atmosphere exchanges of water, energy, and momentum, such studies have often focused on the role of feedbacks in the evolution of temperature and evaporation over only a single day (*Jacobs and De Bruin*, 1992; *van Heerwaarden et al.*, 2009, 2010). In such work, initial conditions are often of major importance, and model results are compared to observations of weather, rather than climate.

Our work focuses on longer time scales, emphasizing the importance of land surface properties in determining daily-average surface and boundary layer temperatures. Because of the relative unimportance of the diurnal cycle for ocean-atmosphere coupling, the equilibrium climate of the surface-boundary layer system over the ocean is more easily defined, observed, and modeled (*Betts and Ridgway*, 1988, 1989). The problem of the daily-average state of the coupled surface-boundary layer system over land was tackled later, first by models with fixed boundary layer depth (*Brubaker and Entekhabi*, 1995; *Entekhabi and Brubaker*, 1995; *Brubaker and Entekhabi*, 1996), then by models with variable boundary layer depth (*Kim and Entekhabi*, 1998; *Betts*, 2000). The elegant studies of *Entekhabi and Brubaker* (1995) and *Brubaker and Entekhabi* (1996) used an idealized model to explore the feedbacks that serve to amplify

or dampen forced soil moisture and temperature variability over time scales of days to months. However, the temperature variability in their work was forced by wind speed, rather than any changes in land surface properties, and their assumption of constant boundary layer height cuts the important connection between warming and boundary layer deepening, as well as any control on boundary layer temperatures exerted by the free troposphere. Our work will build off the diurnally-averaged mixed layer-surface model of *Betts* (2000), which has a very simple treatment of radiation and surface turbulent exchange, but relaxes the constant-height assumption of *Brubaker and Entekhabi* (1995) and the constant specific humidity assumption of *Kim and Entekhabi* (1998).

Based on the model of *Betts* (2000), we derive analytic expressions for the response of surface temperature and boundary layer potential temperature to forcing by perturbations in surface moisture availability, albedo, and roughness. As in the studies of *Brubaker and Entekhabi* (1996) and *Kim and Entekhabi* (1998), our theory associates the strongest negative feedback with the dependence of the surface latent heat flux on saturation vapor pressure. We compare the results from our analytic theory to the full model of *Betts* (2000), and show that our theory can explain nearly all of the sensitivity of the *Betts* (2000) full system of equations. As in the case of the nonlinear (approximately logarithmic) radiative forcing by CO_2, we find that allowance for nonlinear forcing functions is important, especially for large changes in surface moisture availability and roughness. We find that the theory agrees well with simulation results from a more complex two-column radiative-convective model, and discuss limitations of the theory. We conclude by discussing how our theory may allow for a more unified understanding of the boundary layer climate response to disparate problems such as urbanization, deforestation, drought, and CO_2-induced stomatal closure.

4.2 Theory

4.2.1 Framework for Boundary Layer Sensitivity

Top-of-atmosphere radiative energy balance serves as the guiding principle in the theory of global climate sensitivity:

$$R_S - R_L = 0, \tag{4.1}$$

where R_S is the top-of atmosphere net downwards shortwave radiation absorbed by the Earth, and R_L is the top-of-atmosphere net longwave radiation emitted by the Earth. To understand how an arbitrary forcing parameter, A (e.g., CO_2), affects the climate near a known reference state, we take the total derivative of top-of-atmosphere energy balance with respect to A:

$$\frac{dR_S}{dA} - \frac{dR_L}{dA} = 0. \tag{4.2}$$

We expand the total derivatives into forcings (e.g., $\partial R_L/\partial A$), plus products of feedbacks and responses (e.g., $(\partial R_L/\partial T)(dT/dA)$, where T represents global temperature), and then solve for the response as the sum of forcings divided by the sum of feedbacks. Such a decomposition of the climate response to increasing concentrations of well-mixed greenhouse gases has helped us to standardize model simulations, focus study on key mechanisms that mediate the strength of the climate response, and identify ways in which models resemble or differ from one another.

We propose a similar framework for boundary-layer climate sensitivity, with a guiding principle of surface energy balance. Assuming a long-term equilibrium with no subsurface heat flux, surface energy balance is given by:

$$Q_S - Q_L - H - E = 0, \tag{4.3}$$

where Q_S is the net shortwave radiation at the surface (positive downwards), Q_L is the net longwave radiation at the surface (positive upwards), E is the latent heat flux

and H is the sensible heat flux (both defined to be positive upwards). To apply a sensitivity framework to the problem, we begin by taking the total derivative of (4.3) with respect to the arbitrary variable A, near a well-defined reference state of the surface-boundary layer system, where surface energy balance holds:

$$\frac{dQ_S}{dA} - \frac{dQ_L}{dA} - \frac{dH}{dA} - \frac{dE}{dA} = 0. \tag{4.4}$$

Expansion of each of these total derivatives by the chain rule is algebraically complicated, and requires us to define which controlling variables to include in our expansion of (4.4). We suggest that the set of controlling variables should include at least the ground temperature, T_S, the near-surface potential temperature of the boundary layer, θ_M, and the near-surface specific humidity of the boundary layer, q_M (these are also three of the prognostic variables in the idealized model of *Brubaker and Entekhabi* (1995)). Variables related to cloudiness, especially low-level cloud fraction and water path, may also be quite important, but we will not consider them explicitly in our example case below.

Once such a set of controlling variables is defined, we can define a boundary layer climate sensitivity by:

1. Eliminating all but one controlling variable by identifying relationships among them (e.g., by linearly relating changes in T_S and q_M to changes in θ_M)

2. Evaluating, theoretically or empirically, the partial derivatives of the surface fluxes with respect to the controlling variables (terms such as $\partial E/\partial T_S$)

3. Algebraically rearranging to solve for how changes in a controlling variable are affected by changes in a forcing variable, δA

The framework proposed here may seem abstract and somewhat open-ended, but this is intended for generality. In order to apply this framework to a GCM, one would likely have to conduct a suite of perturbation experiments. The relationships among controlling variables, as well as the partial derivatives of surface fluxes with respect to controlling variables, could be evaluated by multiple linear regression.

In order to provide a more concrete example of the proposed framework, the remainder of the theory section will be devoted to deriving the boundary layer sensitivity of a highly idealized model of the equilibrium boundary layer, as presented by *Betts* (2000). With appropriate simplifications and assumptions, it will turn out that we can actually arrive at an analytic expression for the sensitivity of the equilibrium boundary layer to forcing by changes in various surface parameters. For the convenience of a reader who is interested in our ideas but not our detailed derivation, we include the key equations from the analytic sensitivity theory (sections 4.2.2-4.2.7) in Tables 4.1 and 4.2.

4.2.2 Equilibrium Boundary Layer Model of *Betts* (2000)

Following the work by *Betts* (2000) (hereafter B00), we seek to understand the problem of the surface-atmosphere interaction by considering equations for the time-mean surface temperature T_S, and the time-mean boundary layer potential temperature and specific humidity, θ_M and q_M, in a well-mixed boundary layer (ML) (see Figure 4-1 for a schematic of the thermal structure). Here, we review some of the key model assumptions from B00.

Following commonly used conventions (e.g., (*Allen et al.*, 1998; *Jones*, 1992)), B00 defines bulk formulae for the latent and sensible heat fluxes E and H as follows:

$$E \;=\; \rho L_v \frac{g_a g_v}{g_a + g_v}(q^*(T_S) - q_M), \tag{4.5}$$

$$H \;=\; \rho c_p g_a (T_S - \theta_M), \tag{4.6}$$

where ρ is the density of air, L_v is the latent heat of vaporization of water, c_p is the specific heat capacity of air, $q^*(T_S)$ is the saturation mixing ratio of water vapor at surface temperature (for simplicity, we assume that the surface pressure equals the reference pressure in the definition of θ). The surface conductance to sensible heat flux, g_a (units: m/s), can be written as the product of a nondimensional enthalpy
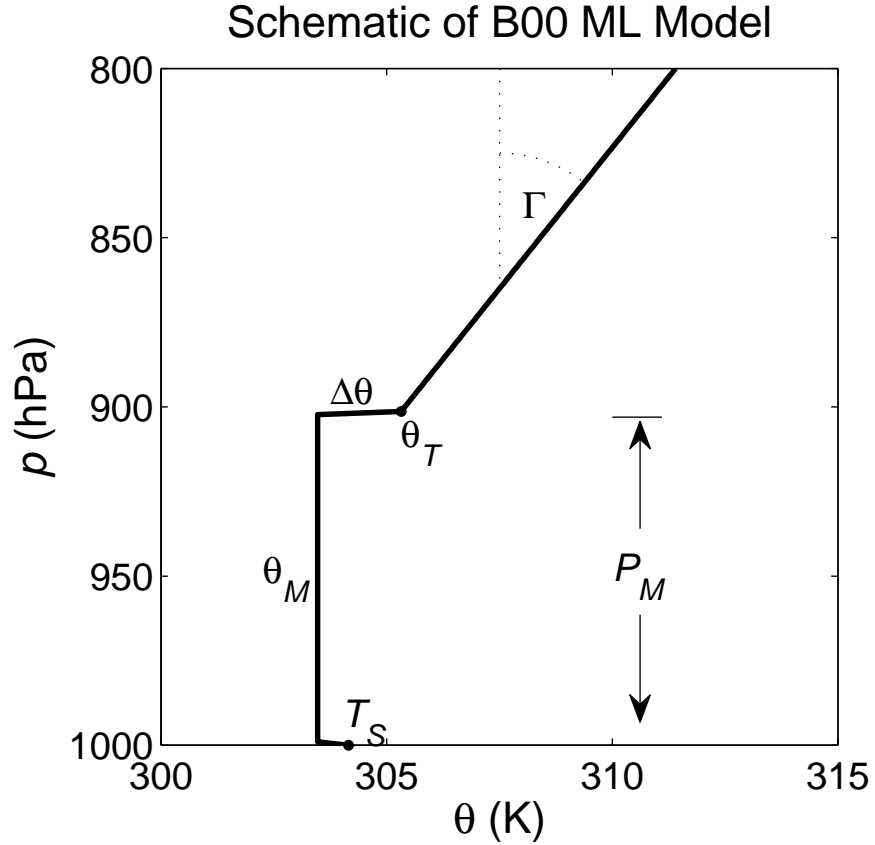
61

Figure 4-1: Schematic of thermal structure in *Betts* (2000) Equilibrium Boundary Layer model.

flux coefficient, c_k, and a surface windspeed, $|\mathbf{v_s}|$:

$$g_a = c_k|\mathbf{v_s}|. \tag{4.7}$$

The surface conductance to water vapor, g_v (units: m/s), represents the limited availability of water for evaporation over land; viewed as a resistance, g_v^{-1} describes the additional path though which water within a leaf (or under the soil) must diffuse in order to arrive at the outermost layer of the leaf (or soil surface) and enter the atmosphere. The total conductance to latent heat flux, $g_a g_v/(g_a + g_v)$, is equivalent to the total conductance of two conductors in series, and can alternatively be viewed as a product of the conductance to sensible heat flux, g_a, and a dimensionless evaporative efficiency:

$$\beta \equiv g_v/(g_a + g_v). \tag{4.8}$$

The evaporative efficiency β can vary between limits of 0 ($g_v = 0$, completely dry surface, no latent heat flux) and 1 ($g_v \to \infty$, completely wet surface, identical exchange coefficients for sensible and latent heat fluxes). Over a vegetated surface, g_v is primarily determined by the number, size, and openness of the numerous leaf pores, or stomata, of the canopy. If the atmospheric inputs, including the surface radiative fluxes, are considered as given, the three equations ((4.3), (4.5), and (4.6)) can be solved simultaneously for the three unknowns: the two components of the surface enthalpy flux and the surface temperature. By assuming the surface-air temperature difference is small, the latent heat flux equation can be linearized, and the system can be solved analytically; this gives the well-known Penman-Monteith equation (*Monteith*, 1965).

In addition to equations for bulk fluxes and surface energy balance, B00 uses equations for ML moisture and energy balance, and two equations for the jumps $\Delta\theta$ and Δq just above the top of the ML. A key difference between the model of B00 and that of *Brubaker and Entekhabi* (1995) is that B00 prescribes boundary conditions just above the top of the ML for θ and q, which depend on the pressure thickness of the ML (ML height in *Brubaker and Entekhabi* (1995) is fixed). The upper boundary condition on θ is important to our theory, and discussed below in more detail. The upper boundary condition on q is relatively unimportant to our theory, and we only mention it here briefly: air just above the top of the ML, with potential temperature and specific humidity (θ_T, q_T), is assumed to have a prescribed saturation point deficit $\mathcal{P}_\mathcal{T}$, or pressure distance that it must be lifted to reach its LCL. B00 also uses two closures that are important for our theory; one relates the ML-top downward buoyancy flux to the surface buoyancy flux, and the other states that the ML extends upward to the lifted condensation level (LCL) of air in the ML (both are discussed below in more detail). Our derivation in Section 4.2.3 requires the energy balance equation, upper boundary condition on θ, and the LCL closure; we also use the buoyancy flux closure, but apply it without the virtual temperature correction for simplicity, as in *Tennekes* (1973).

In the absence of advective tendencies, the leading-order energetic balance in

the ML is between sensible heat flux convergence and net radiative cooling (B00, *Takahashi* (2009)). However, since we want to allow for deep precipitating convection over land in our simulations, we follow B00 and also include a term for convective cooling of our reference state ML, which consists of the combination of latent cooling by evaporating rainfall, and sensible cooling by penetrative downdrafts. Defining $\overline{Q_C}$ as the ML average convective cooling rate, and $\overline{Q_R}$ as the ML average radiative cooling rate, we introduce a total convective plus radiative average cooling rate (units: K/s) for the boundary layer:

$$\overline{Q_\Sigma} = \overline{Q_R} + \overline{Q_C}. \tag{4.9}$$

Then, using the *Tennekes* (1973) closure of linking ML-top sensible heat flux to surface sensible heat flux, we can write the ML thermal balance as:

$$(1+k)H = \frac{c_p \overline{Q_\Sigma} P_M}{g}, \tag{4.10}$$

where k is a coefficient relating the downward sensible heat flux at the top of the ML to the surface sensible heat flux (typically ~ 0.2; *Tennekes* (1973)), and P_M is the pressure thickness of the ML. As in B00, P_M is assumed to be given by the difference between the surface pressure (p_s) and the pressure at the lifted condensation level of air in the boundary layer:

$$P_M = p_s - p_{LCL}(\theta_M, q_M). \tag{4.11}$$

The closure that the top of the ML lies at the LCL is consistent with a shallow cumulus mass flux (out of the ML) which is nearly zero if the top of the ML is subsaturated, but increases very strongly as the top of the ML reaches supersaturation. This closure also assumes that a nonzero shallow cumulus mass flux out of the ML is required to balance the ML water budget; this assumption may break down if the ML is very deep and dry, or if subsidence very strong, or if the air above the top of the ML is extremely dry. We also assume that the potential temperature just above the top of

the ML, θ_T, has a known profile:

$$\theta_T = \theta_{00} + \Gamma(P_M - P_{00}), \tag{4.12}$$

where θ_{00} is the potential temperature of the free troposphere just above a ML with reference thickness P_{00}, and Γ is the absolute value of the lapse rate of potential temperature in pressure coordinates (K/Pa). The boundary layer potential temperature is related to θ_T by:

$$\theta_M = \theta_T - \Delta\theta. \tag{4.13}$$

Equations (4.10), (4.11), (4.12), and (4.13) correspond to B00 equations (16), (21), (12), and (10), respectively.

   To solve for the ML thermal structure and fluxes, B00 further requires a moisture budget equation, as well as equations for ML-top jumps and fluxes that result in a balance between mass addition to the ML by entrainment, and mass removal from the ML by the combination of subsidence and a shallow convective mass flux. The mass balance requirement warms and dries the ML by replacing ML air (θ_M, q_M) with free-tropospheric air (θ_T, q_T). We will proceed without these additional expressions in our sensitivity theory, due to the observation that in the results of B00, changes in $\Delta\theta$ are much smaller than changes in θ_M, typically by roughly a factor of 10 (see B00 Figure 4a as compared to 3a). This observation can be used to outline the route to the analytic sensitivity theory that we will take. Informally, based on (4.13), the smallness of changes in the jump $\Delta\theta$ implies that $\delta\theta_M \approx \delta\theta_T$, and together with (4.12), we have $\delta\theta_M \approx \Gamma\delta P_M$. Along with (4.10) and (4.11), this allows us to link changes in θ_M to changes in T_S and q_M. With the enthalpy flux definitions and surface energy balance, we can then determine the sensitivity of θ_M to changes in an arbitrary variable A that affects the surface energy budget. Before assuming anything specific about the forcing agent A, we will first proceed through most of this derivation (section 4.2.3), and also discuss the key feedbacks in the system (section 4.2.4). We will then discuss the specific cases of forcing by changes in surface conductance to water vapor, surface albedo, and surface aerodynamic conductance (sections 4.2.5, 4.2.6, and 4.2.7,

65

respectively). Our specific choice of three land surface parameters stems in part from past studies; *McNaughton and Spriggs* (1986) and *Jacobs and De Bruin* (1992) both explored the sensitivity of boundary layer growth and evaporation over a single day to the surface resistance (r_s), net radiation ($Q^* = Q_S - Q_L$), and aerodynamic resistance (r_a). Each of these parameters maps cleanly to one of our land surface parameters; surface resistance is the reciprocal of vegetation conductance ($r_s = 1/g_v$), surface net radiation is directly affected by albedo ($Q^* = (1 - \alpha)Q_S^\downarrow - Q_L$), and surface aerodynamic resistance is the reciprocal of aerodynamic conductance ($r_a = 1/g_a$).

4.2.3   Analytic Sensitivity Theory for B00 Model

We expand the total derivative of surface energy balance with respect to A (4.4) using the chain rule (see Appendix 4.7.2; (4.49)-(4.52)). This expansion yields terms containing factors of dT_S/dA and dq_M/dA; we seek to eliminate both of these in favor of $d\theta_M/dA$, thus allowing us to solve for $d\theta_M/dA$.

To obtain the relationship between dT_S/dA and $d\theta_M/dA$, we differentiate (4.10) with respect to A (also using the chain rule expansion of dH/dA):

$$\frac{\partial H}{\partial A} + \rho c_p g_a \left(\frac{dT_S}{dA} - \frac{d\theta_M}{dA} \right) = \frac{c_p \overline{Q_\Sigma}}{g(1 + k)} \frac{dP_M}{dA}. \tag{4.14}$$

Here, we have assumed that k does not depend on A, and (as in B00) that the changes in integrated cooling of the boundary layer are dominated by changes in the pressure depth of the boundary layer, P_M, rather than by changes in the average ML cooling rate, $\overline{Q_\Sigma}$. This is a somewhat inaccurate assumption in a model with full radiative transfer and convection parameterizations, as the ML depth typically affects its cooling rate by both radiation and convection; this limitation will be discussed later. As discussed above, we next assume that changes in the jump $\Delta\theta_M$ are small, so that:

$$\frac{d\theta_M}{dA} = \frac{d\theta_T}{dA} - \frac{d\Delta\theta}{dA} \approx \frac{d\theta_T}{dA} = \Gamma \frac{dP_M}{dA}, \tag{4.15}$$

Applying (4.15) to (4.14) to eliminate dP_M/dA, and rearranging to isolate dT_S/dA,

gives the relationship we sought between dT_S/dA and $d\theta_M/dA$:

$$\frac{dT_S}{dA} = -\frac{1}{\rho c_p g_a}\frac{\partial H}{\partial A} + (1+\gamma)\frac{d\theta_M}{dA}, \qquad (4.16)$$

where we have defined γ as follows for notational convenience:

$$\gamma \equiv \frac{\overline{Q_\Sigma}}{\rho g_a g \Gamma(1+k)}. \qquad (4.17)$$

This nondimensional parameter, γ, relates changes in T_S and θ_M (typically $\gamma \sim 0.2$). If A does not directly affect H, then changes in T_S are just linearly related to changes in θ_M, with the proportionality constant $(1+\gamma)$.

Obtaining the relationship between dq_M/dA and $d\theta_M/dA$ simply involves careful application of the closure (4.11) from B00, which assumes the top of the ML coincides with the LCL. First, we note that that q_M is equal to $q^*(T_b, p_b)$, where T_b is the temperature at the top of the ML, and p_b is the pressure at the top of the ML ($p_b = p_s - P_M$):

$$T_b = \theta_M(p_b/p_s)^{(R/c_p)} \qquad (4.18)$$

This means that:

$$\frac{dq_M}{dA} = \frac{d}{dA}\left(\frac{\epsilon e^*(T_b)}{p_b}\right), \qquad (4.19)$$

where e^* is the saturation vapor pressure at T_b. Using (4.15), we can eliminate $dp_b/dA = -dP_M/dA$ from the expansion of (4.19) (see Appendix 4.7.1 for details):

$$\frac{dq_M}{dA} = \xi\frac{d\theta_M}{dA}, \qquad (4.20)$$

where for notational purposes we have defined ξ as follows:

$$\xi \equiv \left[\frac{\partial q^*}{\partial T}\bigg|_{T_b}\left(\frac{p_s}{p_b}\right)^{\frac{R}{c_p}}\left(1 - \frac{R\theta_M}{c_p p_b \Gamma}\right) + \frac{q_M}{p_b \Gamma}\right]. \qquad (4.21)$$

Our definition of ξ includes the reminder that the partial derivative of q^* with respect to T is evaluated at (T_b, p_b), because other instances of $\partial q^*/\partial T$ that will later

appear are evaluated at surface temperature and pressure. While the expression for ξ is cumbersome, all of the terms in it should be known straightforwardly from the reference state. Unless the atmosphere is extremely stable (i.e., Γ is very large), ξ is negative; so long as free-tropospheric temperatures decrease with height, a deeper, warmer ML still has colder ML-top temperature. Since ML-top temperature is the primary control on saturation mixing ratio, this implies q_M must decrease as θ_M increases. If the lapse rate above the ML is approximately moist adiabatic, then saturation static energy $(L_v q^* + c_p T + gz)$ is nearly constant with height, and it follows that $\xi \approx -c_p/L_v$.

We can now return to (4.4), applying (4.16) and (4.20) to solve for $d\theta_M/dA$; as the algebra is somewhat cumbersome, details of the derivation are given in Appendix 4.7.2. We can then cast the expression into finite-difference form to get $\delta\theta_M \equiv \theta_M - \theta_{M0}$ in terms of $\delta A \equiv A - A_0$, giving forcings that are linear in the perturbation δA ($_0$s represent reference-state values; linear forcings are defined by (4.60)). Alternatively, we can integrate to obtain forcings that are nonlinear functions of A and A_0 (nonlinear forcings are defined by (4.23)). Either way, we can rearrange our solution for $d\theta_M/dA$ to obtain a response-forcing-feedback expression:

$$\delta\theta_M = \frac{F_{Q_S}^A - F_{Q_L}^A - F_E^A}{\lambda_H + \lambda_E + \lambda_{Q_L} - \lambda_{Q_S}}. \tag{4.22}$$

The terms in the numerator of (4.22) (e.g., F_E^A) are shorthand for forcings, have units of W/m^2, and are fundamentally dependent on the choice of A. Generally we will opt to use nonlinear forcings, because they capture the largest nonlinearities in the system, allowing our theory to be useful much further from a reference state than would be true of the completely linear theory. Note that this is directly analogous to the case of global climate sensitivity, where the radiative forcing of a well-mixed greenhouse gas is often nonlinear in its concentration change, but the rest of the sensitivity theory is linear (e.g., feedbacks are assumed constant). A well-known specific example of nonlinear forcing is the approximately logarithmic dependence of radiative forcing on the CO_2 concentration ratio (e.g., Table 6.2 of *Ramaswamy*

(2001)). In our case, general expressions for the nonlinear forcings are:

$$F_{Q_S}^A \equiv \int_{A_0}^A \left(\frac{\partial Q_S}{\partial A'} - \frac{1}{\rho c_p g_a} \frac{\partial Q_S}{\partial T_S} \frac{\partial H}{\partial A'} \right) dA'$$

$$F_{Q_L}^A \equiv \int_{A_0}^A \left(\frac{\partial Q_L}{\partial A'} - \frac{1}{\rho c_p g_a} \frac{\partial Q_L}{\partial T_S} \frac{\partial H}{\partial A'} \right) dA'$$

$$F_E^A \equiv \int_{A_0}^A \left(\frac{\partial E}{\partial A'} - \frac{1}{\rho c_p g_a} \frac{\partial E}{\partial T_S} \frac{\partial H}{\partial A'} \right) dA'. \qquad (4.23)$$

Each of these is modified from the direct forcing of a surface flux (e.g., $\int (\partial Q_S/\partial A') dA'$) by an additional term, dependent on $\partial H/\partial A$, that arises because of the dependence of dT_S/dA on $\partial H/\partial A$ in (4.16). This additional term always causes F_H^A to equal zero, but in effect transmits the impacts of $\partial H/\partial A$ to the other forcing terms.

The λ terms in the denominator of (4.22) (e.g., λ_E) represent feedbacks, have units of $W/m^2/K$, and are independent of the choice of A:

$$\lambda_{Q_S} \equiv (1+\gamma)\frac{\partial Q_S}{\partial T_S} + \frac{\partial Q_S}{\partial \theta_M} + \xi \frac{\partial Q_S}{\partial q_M}$$

$$\lambda_{Q_L} \equiv (1+\gamma)\frac{\partial Q_L}{\partial T_S} + \frac{\partial Q_L}{\partial \theta_M} + \xi \frac{\partial Q_L}{\partial q_M}$$

$$\lambda_H \equiv (1+\gamma)\frac{\partial H}{\partial T_S} + \frac{\partial H}{\partial \theta_M} + \xi \frac{\partial H}{\partial q_M}$$

$$\lambda_E \equiv (1+\gamma)\frac{\partial E}{\partial T_S} + \frac{\partial E}{\partial \theta_M} + \xi \frac{\partial E}{\partial q_M}. \qquad (4.24)$$

Thus, before we choose a specific variable to assign as A, we can generally investigate the feedbacks λ_{Q_S}, λ_{Q_L}, λ_H, and λ_E. The sign convention for feedbacks in (4.22) has anticipated that surface enthalpy fluxes and longwave radiation will act as negative feedbacks, and shortwave radiation will act as a positive feedback (in the absence of cloud radiative effects, λ_{Q_S} will be nearly zero).

If we can solve for all the terms in (4.22), then we can use (4.16) to determine changes in T_S, or (4.20) to determine changes in q_M. It is also straightforward to then calculate the sensitivity of surface fluxes to changes in A (using (4.53)-(4.56) and (4.22)). For example, changes in the latent heat flux (δE) are given generally by $\delta E = F_E^A + \lambda_E \delta \theta_M$; if F_E^A were the only nonzero forcing, then this would simplify to

$\delta E = F_E^A \times (\lambda_H + \lambda_{Q_L} - \lambda_{Q_S})/(\lambda_H + \lambda_E + \lambda_{Q_L} - \lambda_{Q_S})$. Though we will not discuss the sensitivity of surface fluxes further, the solutions we will give below for $d\theta_M/dA$ contain all of the terms necessary to calculate surface flux sensitivities to an arbitrary variable.

4.2.4 Feedbacks: λ_H, λ_E, λ_{Q_S}, and λ_{Q_L}

The enthalpy flux feedbacks are typically most important, and can be simply calculated from our bulk formulae:

$$\lambda_H = \rho c_p g_a \gamma \tag{4.25}$$

$$\lambda_E = \rho L_v \frac{g_a g_v}{g_a + g_v} \frac{\partial q^*}{\partial T} \left[1 + \gamma - \xi \left(\frac{\partial q^*}{\partial T} \right)^{-1} \right], \tag{4.26}$$

where $\partial q^*/\partial T$ is considered to be evaluated at the reference state surface temperature. For a relatively moist reference land surface with $g_a = 0.025$ m/s, $g_v = 0.008$ m/s, with $\gamma \sim 0.2$, $\xi/(\partial q^*/\partial T) \sim$-0.31 (using the moist-adiabatic approximation for $\xi \approx -c_p/L_v$), and a surface temperature of ~ 300 K, $\lambda_H \sim 5.8$ W/m^2/K, and $\lambda_E \sim 34$ W/m^2/K. As we will soon show, this implies that λ_E is generally the dominant feedback for warm and moist land surfaces. Since λ_E decreases as g_v drops, the surface-ML system is typically more sensitive for a dry reference state than a moist one.

In the work of B00, the radiative feedbacks are both assumed to be zero, since the surface net radiation is a prescribed parameter. As we will soon show, this is likely a fine approximation for λ_{Q_L}. However, changes in shortwave forcing associated with changes in cloud properties may be quite important. Despite this potential importance, since we do not have a straightforward physical basis for understanding sensitivities such as $\partial Q_S/\partial q_M$, we will generally take the shortwave radiative feedback λ_{Q_S} to be zero. We will later attempt to empirically evaluate λ_{Q_S} in the two-column model simulations with cloud-radiation interactions enabled.

The longwave flux feedback is typically weak; consider the limit of a ML that is optically thick in most of the infrared, so that we can assume that both surface and

ML emit as blackbodies. Then, the net longwave radiation from the surface simply increases with the thermal contrast between the surface and the boundary layer:

$$\lambda_{Q_L} = 4\sigma_B T_{S0}^3 \gamma, \tag{4.27}$$

where σ_B is the Stefan-Boltzmann constant, and we have linearized the longwave emission from the surface and atmosphere about a reference state surface temperature T_{S0}. For the reference conditions mentioned above, this implies $\lambda_{Q_L} \sim 1.2$ W/m^2/K. As compared to λ_H of 5.8 W/m^2/K and λ_E of 34 W/m^2/K, longwave feedbacks are relatively insignificant.

In the opposite limit of a ML that is optically thin in the IR, as might be the case under much cooler conditions, λ_{Q_L} rises to $4\sigma_B T_{S0}^3(1+\gamma) \approx 5.7$ W/m^2/K for T_{S0}=275 K. Because λ_E decreases rapidly as surface temperature drops (to ~ 15 W/m^2/K for a 275 K surface and the same assumptions as above), λ_{Q_L} can rise considerably in relative importance for colder situations, but it generally is not the dominant feedback unless λ_H and λ_E are also lowered due to weak reference-state surface winds or low surface roughness.

The study of *Brubaker and Entekhabi* (1996) suggests nearly the same order of importance of feedbacks as we have estimated here, though the differences in their model structure as compared to ours translates to different analytic feedback expressions, and the magnitude of their turbulent feedbacks is generally weaker, because their effective value of g_a is only 0.004 for forced turbulent enthalpy fluxes (as opposed to our $g_a = 0.025$). As a result of the relative weakness of turbulent transfer, and the lower infrared optical thickness of the ML, radiation may be a slightly stronger negative feedback in their results than sensible heat fluxes. They also include a free-convective enhancement of turbulent enthalpy fluxes that depends on the buoyancy velocity scale, with the result that additional feedbacks emerge beyond what we have discussed. The most significant common finding between our study and the work of *Brubaker and Entekhabi* (1996) is the strong negative temperature feedback on soil temperatures due to the dependence of evaporation on the saturation specific

Table 4.1: Key equations from the analytic sensitivity theory of sections 4.2.2-4.2.7

Description	Expression	Eqn. (#)
General Sensitivity Equation	$\delta\theta_M = -\frac{F_{Q_L}^A + F_E^A - F_{Q_S}^A}{\lambda_H + \lambda_E + \lambda_{Q_L} - \lambda_{Q_S}}$	(4.22)
Sensible Heat Flux Feedback	$\lambda_H = \rho c_p g_a \gamma$	(4.25)
Evaporative Feedback	$\lambda_E = \rho L_v \frac{g_a g_v}{g_a + g_v} \left.\frac{\partial q^*}{\partial T}\right|_{T_{S0}} \left[1 + \gamma - \xi\left(\frac{\partial q^*}{\partial T}\right)^{-1}\right]$	(4.26)
Longwave Feedback	$\lambda_{Q_L} = 4\sigma_B T_{S0}^3 \gamma$	(4.27)
Relationship between δT_S and $\delta\theta_M$	$\delta T_S = -\frac{1}{\rho c_p g_a}\frac{\partial H}{\partial A}\delta A + (1+\gamma)\delta\theta_M$	(4.16)
Relationship between δq_M and $\delta\theta_M$	$\delta q_M = \xi \delta\theta_M$	(4.20)
Parameter relating δT_S to $\delta\theta_M$	$\gamma = \frac{\overline{Q_\Sigma}}{\rho g_a g \Gamma(1+k)}$	(4.17)
Parameter relating δq_M to $\delta\theta_M$	$\xi = \left[\left.\frac{\partial q^*}{\partial T}\right|_{T_b} \left(\frac{p_s}{p_b}\right)^{\frac{R}{c_p}}\left(1 - \frac{R\theta_M}{c_p p_b \Gamma}\right) + \frac{q_M}{p_b \Gamma}\right]$	(4.21)

humidity at the surface (strength $\sim$12.66 W/m^2/K in their work); this mechanism is included in our evaporative feedback λ_E.

4.2.5 Forcing by surface conductance to water vapor $(A \to g_v)$

We will now demonstrate how the theory applies to three specific cases of A. First, we consider $A \to g_v$, the bulk surface conductance to water vapor. In this case, Q_S, Q_L, and H do not depend explicitly on g_v, so the only nonzero forcing in the numerator of (4.22) is $F_E^A \to F_E^{g_v}$. Furthermore, since $\partial H/\partial g_v = 0$, $F_E^{g_v}$ contains only the contribution from $\partial E/\partial g_v = g_a E_0/(g_v(g_a + g_v))$, where E_0 is the reference-state latent heat flux:

$$F_E^{g_v} = \int_{g_{v0}}^{g_v} \frac{g_a E_0}{g_v'(g_a + g_v')} dg_v'. \tag{4.28}$$

If the latent heat flux varies much more slowly than g_v itself, then we can assume E_0 is a constant, and the integrated forcing is given by:

$$F_E^{g_v} = E_0 \ln\left(\frac{g_v}{g_{v0}}\frac{g_a + g_{v0}}{g_a + g_v}\right). \tag{4.29}$$

Plugging (4.29) into (4.22) and (4.16), and dropping λ_{Q_S} for brevity, we have:

$$\delta\theta_M = \frac{-E_0}{\lambda_{Q_L} + \lambda_H + \lambda_E} \ln\left(\frac{g_v}{g_{v0}}\frac{g_a + g_{v0}}{g_a + g_v}\right) \tag{4.30}$$

$$\delta T_S = (1 + \gamma)\delta\theta_M. \tag{4.31}$$

We see that reducing g_v leads to warming of the surface and boundary layer, in direct proportion to changes in the logarithm of the evaporative efficiency $\beta = g_v/(g_a + g_v)$ (4.8). A boundary layer warming scale in response to a reduction in surface conductance to water vapor is given by the quantity $\Theta_{g_v} \equiv E_0/(\lambda_{Q_L} + \lambda_H + \lambda_E)$. For the aforementioned reference parameters, which pertain to a moist surface at warm temperatures, and a reference state latent heat flux of $E_0 \sim 120$ W/m², this gives a warming scale of $\Theta_{g_v} \sim 2.9$ K. Thus we expect a 10% change in β to result in a temperature change of ~ 0.29 K.

4.2.6 Forcing by surface albedo $(A \to \alpha)$

The forcing for albedo changes is even more straightforward, since as in the case of g_v, three of the four terms in the surface energy budget (Q_L, H, and E) do not depend explicitly on the albedo, and thus the only nonzero forcing in the numerator of (4.22) is $F^A_{Q_S} \to F^\alpha_{Q_S}$. Furthermore, the forcing in this case is linear in albedo changes. The surface net shortwave radiation is given by $Q_S = (1 - \alpha)Q^\downarrow_S$, so:

$$F^\alpha_{Q_S} = \int_{\alpha_0}^{\alpha} \frac{\partial Q_S}{\partial \alpha'} d\alpha' = -Q^\downarrow_S(\alpha - \alpha_0) = -\frac{Q_{S0}}{1 - \alpha_0}\delta\alpha, \tag{4.32}$$

Where Q_{S0} and α_0 are the reference state net surface shortwave radiation and albedo, respectively, and we have used $\alpha - \alpha_0 \equiv \delta\alpha$. As in section 4.2.5, we can plug (4.32) into (4.22) and (4.16), and we obtain:

$$\delta\theta_M = \frac{-Q_{S0}/(1 - \alpha_0)}{\lambda_{Q_L} + \lambda_H + \lambda_E}\delta\alpha \tag{4.33}$$

$$\delta T_S = (1 + \gamma)\delta\theta_M. \tag{4.34}$$

Increasing albedo thus leads to cooling, and decreasing albedo leads to warming. If we assume $\alpha_0 \sim 0.2$ and $Q_{S0} \sim 200$ W/m^2, then a large change in albedo of $\delta\alpha \sim 0.1$ would lead to a temperature change of only ~ 0.6 K.

4.2.7 Forcing by surface aerodynamic conductance $(A \to g_a)$

Consideration of the case where $A \to g_a$ is considerably more complex, since E depends explicitly on g_a, and the explicit dependence of H on g_a further suggests that $F_{Q_S}^{g_a}$ and $F_{Q_L}^{g_a}$ may be nonzero. First, we note that:

$$\frac{\partial H}{\partial g_a} = \rho c_p (T_{S0} - \theta_{M0}) = \frac{H_0}{g_a}, \tag{4.35}$$

Where H_0 is the reference state sensible heat flux. Taking $\partial Q_S / \partial T_S = 0$ implies that $F_{Q_S}^{g_a} = 0$; Q_L does not depend explicitly on g_a, but since $\partial Q_L / \partial T_S$ is nonzero, we find that:

$$
\begin{aligned}
F_{Q_L}^{g_a} &= \int_{g_{a0}}^{g_a} -\frac{4\sigma_B T_{S0}^3 H_0}{\rho c_p g_a'^2} dg_a' \\
&= \frac{4\sigma_B T_{S0}^3 H_0}{\rho c_p} \left(\frac{1}{g_a} - \frac{1}{g_{a0}} \right).
\end{aligned} \tag{4.36}
$$

The forcing of latent heat flux by changes in g_a has contributions from both the explicit dependence of E on g_a, and the part of $F_E^{g_a}$ that depends on $\partial H / \partial g_a$:

$$
\begin{aligned}
F_E^{g_a} &= \int_{g_{a0}}^{g_a} \left(\frac{\partial E}{\partial g_a'} - \frac{1}{\rho c_p g_a'} \frac{\partial E}{\partial T_S} \frac{H_0}{g_a'} \right) dg_a' \\
&= \int_{g_{a0}}^{g_a} \left[\rho L_v \frac{g_v^2 (q^*(T_{s0}) - q_{b0})}{(g_a' + g_v)^2} - \frac{\rho L_v \frac{g_v g_a'}{g_a' + g_v} \frac{\partial q^*}{\partial T} H_0}{\rho c_p g_a'^2} \right] dg_a' \\
&= \int_{g_{a0}}^{g_a} \frac{g_v}{g_a'(g_a' + g_v)} \left(E_0 - \frac{H_0}{B_e} \right) dg_a' \\
&= \left(E_0 - \frac{H_0}{B_e} \right) \ln \left(\frac{g_a}{g_{a0}} \frac{g_{a0} + g_v}{g_a + g_v} \right),
\end{aligned} \tag{4.37}
$$

where B_e is the equilibrium Bowen ratio (e.g., *Hartmann* (1994)):

$$B_e = \frac{c_p}{L_v \frac{\partial q^*}{\partial T}}. \tag{4.38}$$

To obtain surface temperature changes, we must also integrate the portion of (4.16) that depends directly on $\partial H/\partial A$. Putting the results of (4.36) and (4.37) into (4.22) and (4.16), and performing this extra integration for δT_S, we obtain:

$$\delta\theta_M = \frac{-\left(E_0 - \frac{H_0}{B_e}\right)\ln\left(\frac{g_a}{g_{a0}}\frac{g_{a0}+g_v}{g_a+g_v}\right) - \frac{4\sigma_B T_{S0}^3 H_0}{\rho c_p}\left(\frac{1}{g_a} - \frac{1}{g_{a0}}\right)}{\lambda_{Q_L} + \lambda_H + \lambda_E} \tag{4.39}$$

$$\delta T_S = \frac{H_0}{\rho c_p}\left(\frac{1}{g_a} - \frac{1}{g_{a0}}\right) + (1+\gamma)\delta\theta_M. \tag{4.40}$$

The sensitivity expressions in this case are more complex than in the cases of changes in albedo and surface conductance to water vapor – the sign of $\delta\theta_M/\delta g_a$ is ambiguous, and δT_S is not simply related to $\delta\theta_M$ by the multiplicative factor $(1+\gamma)$. Because terms in the numerator of (4.39) have opposing signs, changes in θ_M due to changes in g_a are typically small; the largest changes in temperature are often associated with the term $H_0/(\rho c_p)(g_a^{-1} - g_{a0}^{-1})$ in the expression for δT_S. If the aerodynamic conductance is halved from a normal value of 0.025 m/s, to 0.0125 m/s, and the reference-state sensible heat flux is 20 W/m^2, then θ_M would increase by $\sim$0.25 K, but T_S would rise by a much larger $\sim$1 K.

4.3 Comparison with B00 Results

The first question we should ask of this theory is: does it reasonably approximate the sensitivities obtained with the full set of equations from B00? To answer this question, we have written a MATLAB script to numerically solve the full set of equations from B00, available at: http://mit.edu/~twcronin/www/code/Betts2000_EBLmodel.m. Our solutions reproduce the results from B00 to within 0.01 K and 0.01 g/kg (Betts, 2013, personal communication), and we can compare the theoretical sensitivities to the numerical solutions for all 3 choices of forcing parameter, $A \rightarrow (g_v, \alpha, g_a)$. B00 does not

Table 4.2: Nonlinear forcings from sections 4.2.5-4.2.7

Forcing Term	$A \to g_v$	$A \to \alpha$	$A \to g_a$
Longwave Forcing ($F_{Q_L}^A$)	0	0	$\frac{4\sigma_B T_{S0}^3 H_0}{\rho c_p}\left(\frac{1}{g_a}-\frac{1}{g_{a0}}\right)$ (4.36)
Shortwave Forcing ($F_{Q_S}^A$)	0	$-\frac{Q_{S0}}{1-\alpha_0}\left(\alpha-\alpha_0\right)$ (4.32)	0
Evaporative Forcing (F_E^A)	$E_0 \ln\left(\frac{g_v}{g_{v0}}\frac{g_{a0}+g_{v0}}{g_a+g_v}\right)$ (4.29)	0	$\left(E_0-\frac{H_0}{B_e}\right)\ln\left(\frac{g_a}{g_{a0}}\frac{g_{a0}+g_{v0}}{g_a+g_v}\right)$ (4.37)

explicitly use an albedo in his equations, but by assuming a fixed Q_L of 50 W/m^2, and a surface albedo of 0.2, his default surface net radiation Q^* of 150 W/m^2 implies $Q_S^\downarrow = $ 250 W/m^2, enabling us to define the forcing $F_{Q_S}^\alpha$ from (4.32). We obtain sensitivities by comparing reference state and perturbation solutions with g_v and g_a varied by factors of 1.1^n, where $n = \pm(1, 2, 3, ..., 9, 10)$, and α modified by $\pm(5, 10, 15, ..., 45, 50)\%$. Reference-state values are $g_{v0} = 0.008$ m/s, $\alpha_0 = 0.2$, and $g_{a0} = 0.025$ m/s. The range of g_v spanned is 0.0031 to 0.0207 m/s, which corresponds to most of the range of values covered in B00.

Figure 4-2 shows a comparison of our theory with the solutions to the full equations from B00, using the reference state parameters from Table 1 of B00 (also see the 'Normal values' column of Table 4.3). We see that the sensitivity theory with linear forcings (dot-dashed lines in Figure 4-2; equation 4.61) is accurate only very close to the reference state for $\pm g_v$ and $\pm g_a$ perturbations, and that the usage of nonlinear forcings (solid lines in Figure 4-2; see Table 4.2) significantly extends the validity of the theory. Note that the shortwave forcing due to albedo changes is linear in α, so there is no difference between linear and nonlinear forcings. In the model of B00 at least, the dominant nonlinearity in the sensitivity of temperature to g_v or g_a is due to nonlinear forcing of the surface energy budget by changing g_v or g_a, rather than non-constancy of the feedbacks. As noted above, the importance of nonlinear forcing is directly analogous to the problem of climate sensitivity, where radiative forcing from greenhouse gases is generally a nonlinear function of concentration changes; it even turns out that the evaporative forcing due to changing g_v is logarithmic in the ratio of evaporative efficiencies β/β_0, just as the radiative forcing due to changing CO_2 is approximately logarithmic in the ratio of final to initial CO_2 concentrations.

To assure that the theory compares well with the B00 model across a range of reference states, and not merely the one shown in Figure 4-2, we can plot the theoretical temperature change ordinates against the B00 model temperature change abscissas, for many reference states. In such a plot, collapse onto the 1-1 line would indicate robustness of the theory across the full set of reference states tested. Figure 4-3 shows that such collapse indeed occurs; for each of 20 different reference-states described
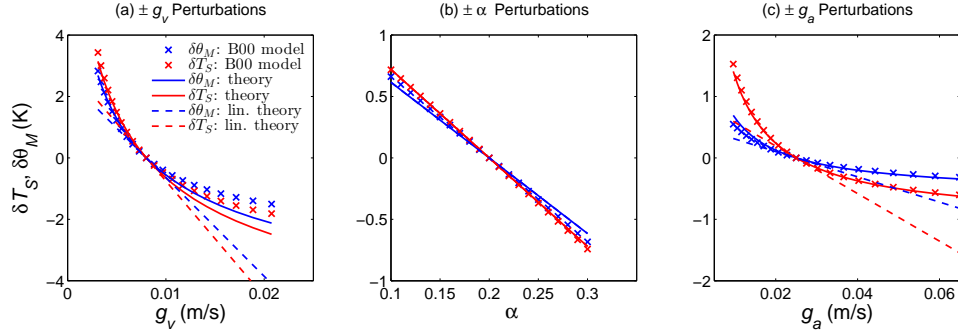
Figure 4-2: Comparison of changes in surface temperature (δT_S, red) and ML potential temperature ($\delta\theta_M$, blue) for the theory (solid and dashed lines) and full numerical solutions from the B00 model ('x'-symbols), for perturbations in individual surface parameters (a) $\pm g_v$, (b) $\pm\alpha$, and (c) $\pm g_a$. Theoretical values of δT_S and $\delta\theta_M$ and are calculated using the fully nonlinear forcing expressions based on (4.23) (solid lines), and using the linear forcing expressions of (4.60) (dashed lines).

Table 4.3: Reference-state parameters used in comparison of theory and solutions to full equation set of B00 (Figure 4-3). Aside from the reference state that uses the normal value for all parameters, each of 19 other reference states is calculated by varying one of the six parameters (Γ, $\mathcal{P}_\mathcal{T}$, Q^*, $\overline{Q_R}$, $\overline{Q_C}$, or θ_{00}) to one of the alternate values listed below, while holding the other five parameters fixed at normal values. Alternate values of all parameters but θ_{00} are taken from B00 (see Table 1 of B00).

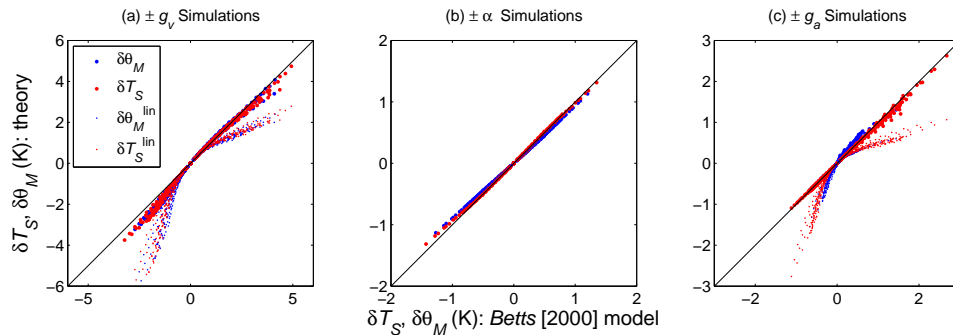| Parameter	Normal value	Alternative values	Units
Stability, Γ	0.06	0.04,0.05,0.07	K/hPa
Subsaturation just above ML, $\mathcal{P}_\mathcal{T}$	100	60,140	hPa
Surface net radiation, Q^*	150	110,130,170	W/m^2
Radiative cooling rate, $\overline{Q_R}$	3	1,2	K/day
Evaporative cooling rate, $\overline{Q_C}$	0	1,2,3	K/day
Potential temperature at 940 hPa, θ_{00}	303	283,288,293,298,308,313	K

Figure 4-3: Comparison of changes in surface temperature (δT_S, red) and ML potential temperature ($\delta \theta_M$, blue) for the theory and full numerical solutions from B00, for perturbations of individual land surface parameters (a) $\pm g_v$, (b) $\pm \alpha$, and (c) $\pm g_a$. Changes in surface temperature δT_S and boundary layer potential temperature $\delta \theta_M$ are computed from the full equation set of B00 (abscissas), and based on the theory of Section 4.2 (ordinates). Theoretical values of $\delta \theta_M$ and δT_S are calculated using the fully nonlinear forcing expressions based on (4.23) (large solid points), and using the linear forcing expressions of (4.60) (small points). A 1-1 line is drawn in black on each subfigure for reference, and each subfigure includes points from 20 reference states, each with 20 perturbations to g_v, α, or g_a — see text and Table 4.3 for details.

in Table 4.3, the theory very nearly matches the changes in temperature given by numerical solutions to the full equation set of B00. Once again, the use of nonlinear forcings vastly improves the fidelity of the theory to its parent model, especially for large perturbations to g_v and g_a; hereafter we will show comparisons only using the nonlinear-forcing theory.

4.4 Two-Column Radiative-Convective Model Simulations

4.4.1 Model Setup

To further evaluate the theory described in Section 4.2, we use a two-column radiative convective (RC) model, which is described in *Abbot and Emanuel* (2007); a schematic of the model is shown in Figure 4-4. The model uses the convection scheme of

Emanuel and Zivkovic-Rothman (1999), and the cloud scheme of *Bony and Emanuel* (2001). In all simulations, the model has one column over land, and a second column over ocean. In an attempt to ensure that the free-tropospheric temperatures do not change very much as a land surface parameter is varied, we perform simulations with fixed SST in the ocean column. Together with nonrotating dynamics, the fixed SST lower boundary strongly constrains the average tropospheric temperature profile of both columns, approximately enforcing the key assumption of Equation (4.12). Lateral boundary conditions are periodic, so that air exiting the land column in either direction enters the ocean column, and the system is not subjected to any time-varying large-scale forcing. For all simulations, we use a CO_2 concentration of 360 ppm, and a fixed solar zenith angle whose cosine is 2/3 (equal to the planetary-average, insolation-weighted value); all but one set of simulations are performed with no diurnal cycle of solar radiation.

We perform simulations with and without interactions between clouds and the radiation scheme. We use a relatively fine vertical resolution of 10 hPa, and a short timestep of 1 minute, but horizontal resolution is extremely coarse, with column widths of 4000 km. The intent of such wide columns is to ensure the weakness of horizontal advective tendencies – this only breaks down if the land is extremely dry and warm. Simulations are typically spun up for 100 days, and then run to collect data for an additional 100 days.

The land surface parameters that we vary are the bulk surface conductance to water vapor, g_v, the surface albedo, α, and the bulk aerodynamic conductance over land, g_a. We actually modify g_a by varying c_k, and using a fixed value of $|\mathbf{v_s}|$ within each set of reference plus perturbation simulations, so that $\delta g_a/g_{a0} = \delta c_k/c_{k0}$ (see equation (4.7)). We use the background oceanic drag coefficient $c_{D0} = 0.0015$ ($\neq c_k$) for calculating surface stresses, which act to dissipate overturning circulations.

4.4.2 Reference Simulations

A particular reference state has two separable components: the choice of land surface parameters $(g_{v0}, \alpha_0, c_{k0})$, and the choice of atmospheric boundary conditions. In the
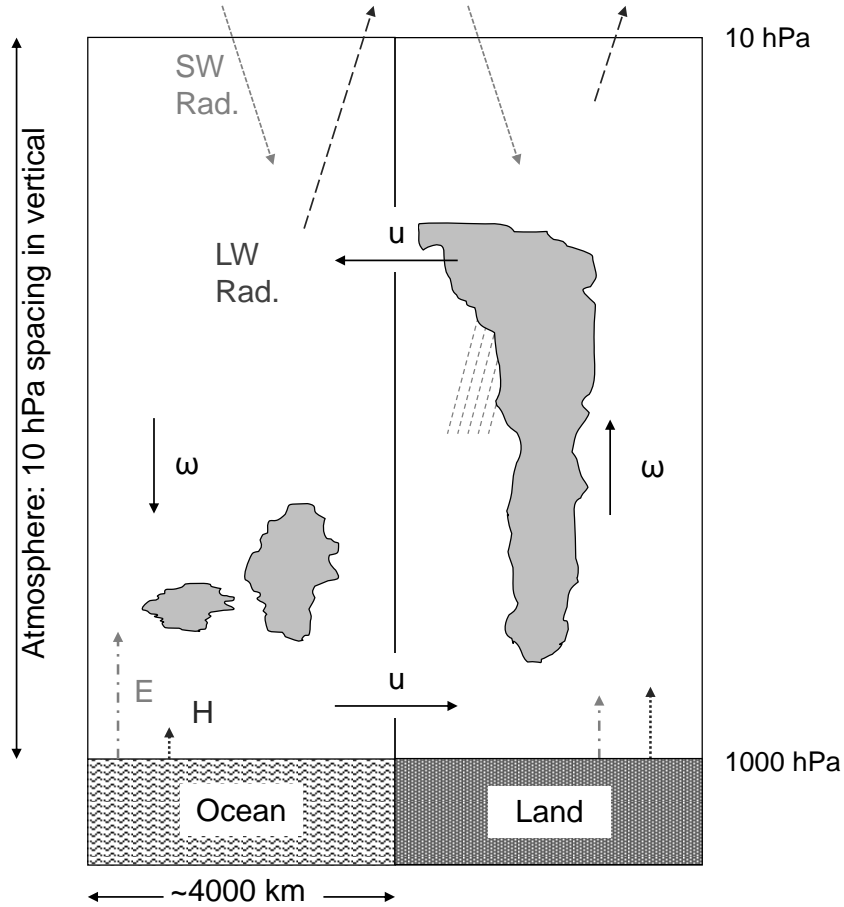
Figure 4-4: Schematic of two-column Radiative-Convective (RC) model used in this study, described in *Abbot and Emanuel* (2007) and *Nilsson and Emanuel* (1999). Dynamics of the overturning circulation are determined by solving prognostic vorticity equations in the direction orthogonal to the model domain.

radiative-convective model, it is no longer possible to directly impose values for any of the six reference-state parameters that were externally specified in Section 4.3 (these parameters were described in Table 4.3). For the radiative-convective model, we will use three external atmospheric boundary conditions: the surface windspeed for enthalpy fluxes $|\mathbf{v_s}|$ (units: m/s), the surface temperature in ocean column T_{SS} (units: K), and the top-of atmosphere insolation I_{TOA} (units: W/m^2).

Due to the absence of well-studied reference surfaces for many vegetation types, we will focus our attention on a single reference surface, with $g_{v0} = 0.008$ m/s, $\alpha_0 = 0.23$, and $c_{k0} = 0.0048$. These parameters are based on the reference grass surface

Table 4.4: Atmospheric boundary conditions used in two-column RC model simulations.

Simulation	$|\mathbf{v_s}|$ m/s	T_{SS} °C	I_{TOA} W/m^2
Standard	5.0	28.0	400.0
V$--$	1.5	32.0	400.0
V$-$	2.5	28.0	400.0
V$+$	10.0	28.0	400.0
V$++$	15.0	28.0	400.0
T$---$	5.0	4.0	280.0
T$--$	5.0	16.0	320.0
T$-$	5.0	24.0	360.0
T$+$	5.0	32.0	420.0
T$++$	5.0	40.0	440.0

described by *Allen et al.* (1998) in UN FAO working paper 56. Since the *Allen et al.* (1998) surface is typically used to calculate a reference evapotranspiration for the purpose of estimating crop water requirements, it has a value of g_v near the upper range of observations for real land surfaces (0.0143 m/s). In order to span a broader range of realistic conditions, we use a somewhat reduced value of g_{v0}, but the same values of α and c_k as in *Allen et al.* (1998) (the value of c_k is derived from Box 4 of *Allen et al.* (1998), assuming that surface enthalpy flux bulk formulae use the 2-meter windspeed).

For our reference surface parameters, we perform 10 sets of sensitivity experiments with a broad range of combinations of the three external atmospheric parameters $|\mathbf{v_s}|$, T_{SS}, and I_{TOA} (see Table 4.4 for details). In all but one set of simulations, we do not include the radiative effects of clouds in model calculations, as the convective parameterization produces mostly high clouds, which do not have much effect on the results, but require longer simulations to attain clean results, due to the greater variability of simulations with interactive clouds.

4.4.3 Perturbation Simulations

For each reference simulation, we test the theory by performing simulations with perturbations to g_v, α, and c_k. As in Section 4.3, we vary g_v and c_k by factors of 1.1^n, where $n = \pm(1, 2, 3, ..., 9, 10)$, and we vary α by $\pm(5, 10, 15, ..., 45, 50)\%$. Our perturbation simulations thus span a very broad range of g_v and c_k (0.0031-0.0207 m/s, and 0.0019 to 0.0124, respectively), and most of the range of α observed for non-snowy land surfaces (0.115-0.345). We compute forcing and feedback terms near each reference state (based on reference-state fluxes, temperatures, and boundary layer cooling rates), and then compare simulated changes in surface temperature δT_S and boundary layer potential temperature $\delta\theta_M$ to the predictions of the theory from Section 4.2. Results in all figures show simulated changes δT_S and $\delta\theta_M$ for the land column only.

To provide a quantitative figure of merit, we also define the R^2 for a variable X as:

$$\mathrm{R}^2(\mathrm{X}) = 1 - \frac{\Sigma(X_{\mathrm{model}} - X_{\mathrm{theory}})^2}{\Sigma(X_{\mathrm{model}} - \overline{X_{\mathrm{model}}})^2}, \qquad (4.41)$$

i.e., as unity minus the fraction of the model variance that remains after comparison with the theory. Note that this is the value of R^2 conditioned on the assumption that $X_{\mathrm{model}} = X_{\mathrm{theory}}$, and not based on a best linear fit ($X_{\mathrm{model}} = mX_{\mathrm{theory}} + b$). Values of R^2 are shown in the corresponding figures.

4.4.4 Results

We first discuss the three-way comparison of the RC model results with both the predictions of the theory and the numerical solutions to the full equations from B00, for the case of no cloud-radiation interactions, and the 'Standard' set of atmospheric boundary conditions from Table 4.4. Figure 4-5 shows that RC model simulations where g_v or c_k are varied (Figures 4-5 (a) and 4-5 (c), respectively) support the theory quite well; RC model results also compare well with the B00 model results for these surface parameters. Both the theory and the B00 model have less skill with albedo variations (Figure 4-5 (b)); though the functional form of temperature changes as a
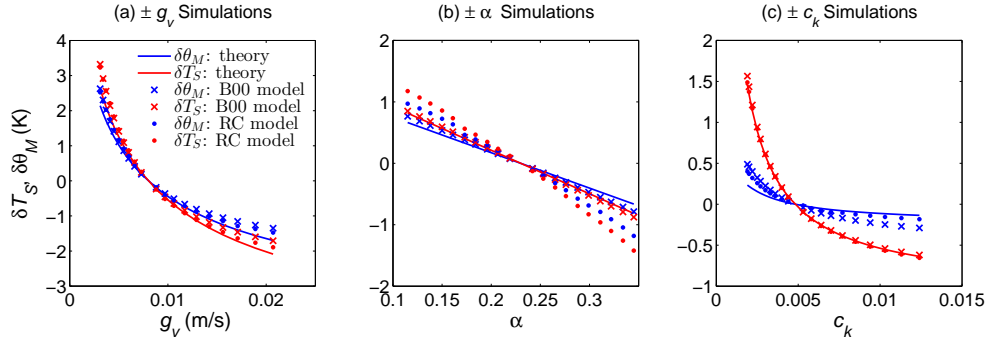
Figure 4-5: Comparison of changes in surface temperature (δT_S, red) and ML potential temperature ($\delta\theta_M$, blue) for the theory (solid lines), RC model simulations (filled circles), and full numerical solutions from the B00 model ('x'-symbols). Subfigures show results for perturbations of individual surface parameters (a) $\pm g_v$, (b) $\pm\alpha$, and (c) $\pm c_k$. All of the reference-state parameters for the sensitivity theory and the B00 model are calculated from the RC model simulation using the 'Standard' atmospheric boundary conditions from Table 4.4.

function of albedo is correctly predicted to be nearly linear, the theory and B00 model results significantly underestimate changes in temperature produced by the RC model simulations. The reasons for this underestimation will soon be discussed in detail. Figure 4-5 also shows that in general, the solutions to the full set of equations from B00 are a slightly better fit to the RC model results than is the analytic theory. This is especially evident at low values of g_v (Figure 4-5 (a)), all values of albedo (Figure 4-5 (b)), and low values of c_k (Figure 4-5 (c)). The better match between the B00 model results and the RC model results at low values of g_v, where temperatures increase more rapidly than the theory predicts, is likely due to reduction in the evaporative feedback λ_E, which the theory assumes to be a constant.

Similarly to section 4.3, we test robustness of the theory across the range of reference states described in Table 4.4, by plotting theoretical temperature change ordinates against RC model temperature change abscissas, with a perfect fit reflected by collapse onto the 1-1 line. Such collapse nearly occurs for $\pm g_v$ and $\pm c_k$ perturbation simulations, where the theory explains from 83%-99% of the deviations in both T_S and θ_M from the reference state (Figures 4-6 (a) and (c)). The theory has less skill with
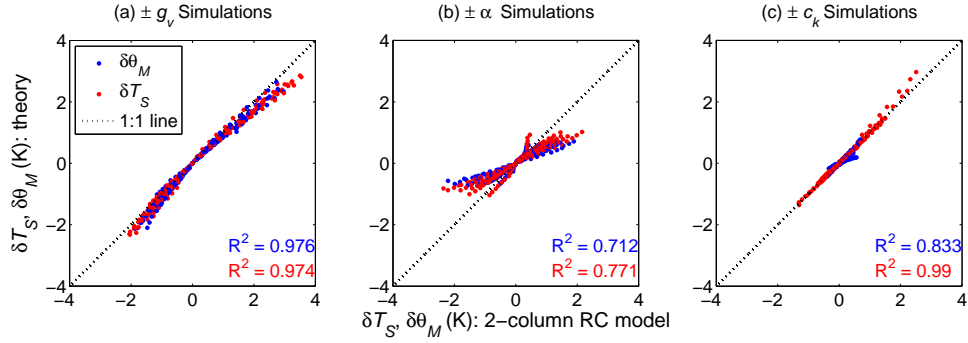
Figure 4-6: Comparison of changes in surface temperature (δT_S, red) and ML potential temperature ($\delta\theta_M$, blue) for the theory, and the $\pm(g_v, \alpha, c_k)$ perturbation simulations with the RC model, for the ten atmospheric boundary conditions listed in Table 4.4. Subfigures show results for perturbations of individual surface parameters (a) $\pm g_v$, (b) $\pm\alpha$, and (c) $\pm c_k$, as described in the text. Values of R^2 as defined in Equation (4.41) are indicated in text for the model-theory comparison for $\delta\theta_M$ (blue) and δT_S (red).

albedo variations; as in the 'Standard' reference state result shown in Figure 4-5(b), the theory tends to underestimate the magnitude of warming or cooling produced by the RC model (Figure 4-6 (b)). However, even for $\pm\alpha$ simulations, the theory still captures between over 70% of the RC model variance in $\delta\theta_M$ and δT_S.

The lower skill of the theory for $\pm\alpha$ simulations, as compared to $\pm(g_v, c_k)$ simulations, is largely due to the violation of constant free-tropospheric temperatures (equation (4.12)). As in the real tropics, the non-rotating dynamics in our RC model allow only very weak horizontal temperature gradients above the boundary layer (*Sobel et al.*, 2001). This dynamical constraint on temperature gradients, together with the fixed-SST lower boundary in the ocean column, strongly constrains the free-tropospheric thermal profile in both columns. With only one buffering ocean column, however, the large changes in convection over land due to changes in albedo can significantly impact the modeled thermal structure above the well-mixed boundary layer. For simulations where α is varied, changes in θ at 700 hPa ($\delta\theta_{700hPa}$) are of the same magnitude as, and well-correlated with, changes in θ_M (Figure 4-7). This is consistent with a two-column RC model sensitivity $|d\theta_M/d\alpha|$ which is greater than
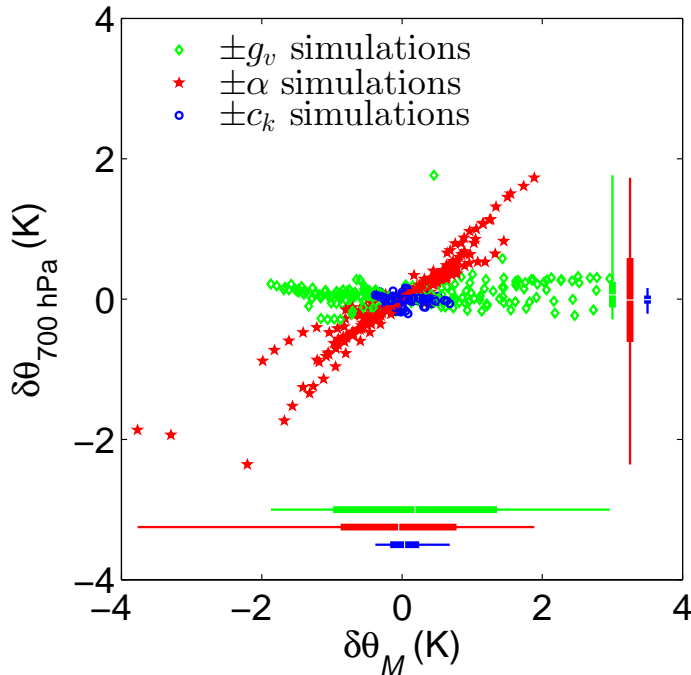
Figure 4-7: Scatter plot of changes in boundary layer and free-tropospheric potential temperatures, $\delta\theta_M$ and $\delta\theta_{700\text{hPa}}$, in the RC model simulations. Significant changes in free-tropospheric potential temperature ($\delta\theta_{700\text{hPa}}$) violate the assumption of (4.12) for $\pm\alpha$ simulations. Thick lines indicate ± 1 standard deviation from the mean, thin lines indicate the range of the data, and white hashes indicate means.

the theory would predict, as is generally the case in our results (Figures 4-5(b) and 4-6(b)). We would expect the addition of more buffering ocean columns in the RC model to decrease the sensitivity of free-tropospheric temperatures to albedo, and thus improve the agreement between RC model results and theory. For simulations where g_v or c_k are varied, Figure 4-7 shows that changes in free-tropospheric potential temperature ($\delta\theta_{700\text{hPa}}$) are small and relatively uncorrelated with changes in boundary layer potential temperature ($\delta\theta_M$), so the assumption of (4.12) is roughly valid; changes in the thermal structure of the lower free troposphere may merely add noise to our results.

We can also use RC model simulation results to attempt to assess the importance of cloud-radiation interactions, as well as the diurnal cycle, for the validity of the theory; we will assess each of these effects separately for a single reference state corresponding to the 'Standard' set of atmospheric boundary conditions.

We find that longer RC model simulations are generally needed to obtain clean results when cloud-radiation interactions are enabled. To obtain the results shown in Figure 4-8, data were collected over 800 days of model time (rather than 100). Generally speaking, the theory still captures a great deal of the behavior of the RC model results, especially for simulations where g_v is perturbed. Departure from good fits in the $\pm\alpha$ and $\pm c_k$ simulations seems to reveal aspects of unexpected behavior in the RC model, rather than illuminating deficiencies in the theory. Cloud-radiation interactions introduce random noise, as well as systematic changes, to the RC model simulations, and sometimes these systematic changes can occur abruptly as a land surface parameter is varied. For example, the abrupt deviation of the RC model results from the predictions of the theory as c_k is increased past about 0.007 coincides with an abrupt change in surface net shortwave radiation, by about 5 W/m^2. The large drop in temperatures at the highest value of albedo coincides with an abrupt decrease in the sensible heat flux by about 7 W/m^2, and a drop in the LCL by over 15 hPa, as compared to results at the next-highest albedo value. We believe that such behavior is artificial, and perhaps represents a constraint of discretization (important transition levels like the tropopause, ML-top, or top of a cloud layer, are sometimes forced to change in discrete jumps), especially with a model that has a limited number of degrees of freedom (i.e., only two columns) and no external sources of variability. Regardless of whether they are physical or not, abrupt changes are not anticipated by our sensitivity theory, and consequently the RC model results are fit less well by the theory when cloud-radiation interactions are enabled. From the standpoint of the sensitivity theory, the principal effects of cloud-radiation interactions are to slightly reduce the reference-state values of Q_{S0} and E_0 due to cloud shading of the surface, and to introduce λ_{Q_S} as a small feedback in the denominator of (4.22). We will discuss the importance of cloud feedbacks in Section 4.5.2.

To look at the impacts of the diurnal cycle, we perform RC model simulations with time-varying solar radiation corresponding to a perpetual spring equinox on the equator, with a slightly reduced value of the solar constant (1256.64 W/m^2) to give a time-mean insolation comparable to the 400 W/m^2 'Standard' choice in Table
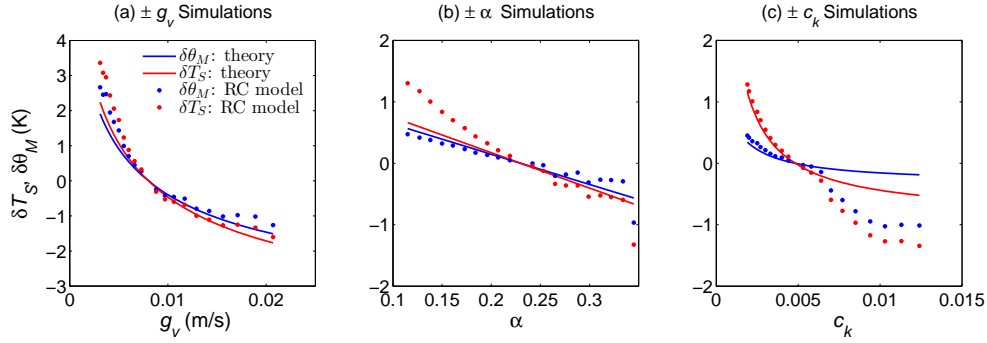
Figure 4-8: As in Figure 4-5, but using RC model simulations with cloud-radiation interactions enabled (and no comparison with B00 model). Subfigures are for perturbations of individual surface parameters (a) $\pm g_v$, (b) $\pm \alpha$, and (c) $\pm c_k$.

4.4. The land surface is treated as a slab with a heat capacity of 2.1×10^5 J/m^2/K, which is slightly lower than the $\sim 3 \times 10^5$ J/m^2/K soil heat capacity in *Brubaker and Entekhabi* (1995). In the reference state, the diurnal cycle of surface temperatures has a maximum of ~ 37.5°C, a minimum of ~ 23.5°C, and a time-mean of 29.2°C, which is slightly lower than the 29.6°C in the comparable reference simulation that uses diurnally-averaged radiation. The RC model does not have a stable boundary layer parameterization — some discrete number of model levels always is well-mixed by hard dry adjustment. The ML depth (P_M, given by the number of dry-adjusted levels) varies between a minimum of 10 hPa at night (1 level) to a maximum of 100 hPa during the early afternoon (10 levels), with gradual growth in the morning and a rapid collapse in the evening. Figure 4-9 shows that the theory is still somewhat successful at predicting the sensitivity of time-mean temperatures from RC model simulations with a diurnally varying boundary layer. The fit is strikingly good for $\pm g_v$ simulations, suffers from similar issues of sensitivity underestimation for $\pm \alpha$ simulations, and is markedly poorer for $\pm c_k$ simulations. The degradation of the fit for $\pm c_k$ simulations, for both θ_M and T_S, is likely related to the large changes in sensible heat flux that occur, and the assumption of small changes in H that went into the derivation of (4.39) and (4.40). From the lowest to the highest values of c_k, H varies from 30.6 to 50.2 W/m^2; these changes are too large to be neglected
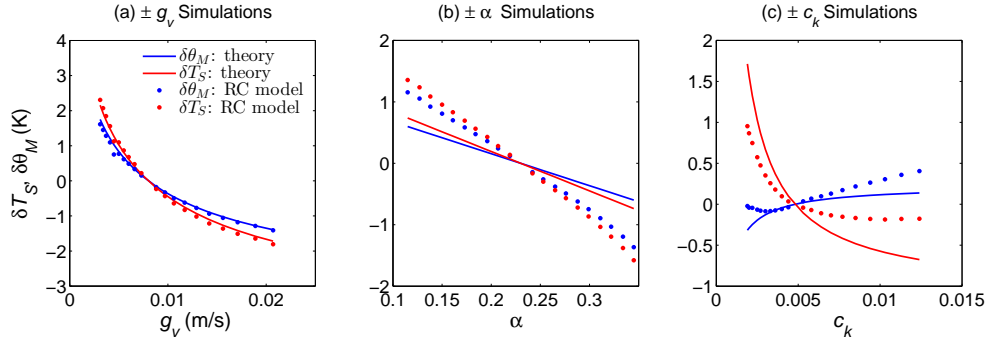
Figure 4-9: As in Figure 4-5, but using RC model simulations with a diurnal cycle of insolation (and no comparison to the B00 model). Subfigures are for perturbations of individual surface parameters (a) $\pm g_v$, (b) $\pm \alpha$, and (c) $\pm c_k$, as described in the text. See text for details on the diurnal cycle.

without consequence, and they are much larger than the changes in H that occur in simulations with diurnally-averaged radiation. This raises the question of how the $\pm g_v$ simulations can be so well captured by the theory, when E varies across the range of g_v perturbation simulations by an even larger amount. The answer to this question likely lies in the covariance of E and λ_E, which makes the term $E/(\lambda_H + \lambda_E + \lambda_{Q_L})$ more constant than either its numerator or denominator.

4.5   Discussion

We believe that the results from Sections 4.3 and 4.4 generally show the theory to be a useful tool by which to understand the sensitivity of the equilibrium boundary layer over land. However, it is worth taking a step back to discuss some of the important limitations and open questions that relate to the applicability of our results.

4.5.1   Limitations of the Theory

Neglect of horizontal advection is a major limitation of the theory, and restricts our attention to regions that are large enough in spatial scale, and weak enough in horizontal gradients, for horizontal advective tendencies to be unimportant in the ML.

Brubaker and Entekhabi (1995) suggest that thermal advection may be unimportant for regions with roughly homogeneous surface conditions that span areas of $\sim 10^4$ to 10^5 km^2, though horizontal moisture advection is always required to balance the water budget in their model. To the extent that the flow in a thermally-driven, linearly damped low-level circulation scales with the temperature gradient (e.g., Section 3c of *Nilsson and Emanuel* (1999)), such circulations generate an advective cooling tendency that scales as the square of the temperature gradient. Thus, if ML temperature gradients in the reference state are weak, a linear sensitivity analysis should ignore changes in horizontal advective cooling as a higher-order term $- (\delta\theta_M)^2 -$ in the ML thermal balance. An interesting subject for future work would be to study how the ML response scales with the horizontal scale of the forcing, which would be relevant for understanding the applicability of the theory to real-world changes in land surface properties.

Another significant limitation, as alluded to above, is the oversimplified treatment of the sensitivity of ML thermal balance involved in deriving (4.14). A full treatment of the change in ML thermal balance requires differentiation of the total ML cooling $(P_M\overline{Q_\Sigma})$:

$$\frac{d}{dA}\left(P_M\overline{Q_\Sigma}\right) = (\overline{Q_{R0}} + \overline{Q_{C0}})\frac{dP_M}{dA} + P_{M0}\left(\frac{d\overline{Q_R}}{dA} + \frac{d\overline{Q_C}}{dA}\right). \tag{4.42}$$

We can quantify the relative importance of changes in ML thickness versus ML average cooling rates by looking at the logarithmic derivative of (4.42):

$$\frac{d}{dA}\ln\left(P_M\overline{Q_\Sigma}\right) = P_{M0}^{-1}\frac{dP_M}{dA} + \overline{Q_{\Sigma 0}}^{-1}\frac{d\overline{Q_R}}{dA} + \overline{Q_{\Sigma 0}}^{-1}\frac{d\overline{Q_C}}{dA} \tag{4.43}$$

We plot the three terms on the RHS of (4.43) against changes in θ_M across the full set of simulations to diagnose their relative importances (Figure 4-10). In general, radiative cooling $(\overline{Q_R})$ decreases with increasing temperature, and convective cooling $(\overline{Q_C})$ increases with increasing temperature, but their relative rates of change per degree of boundary layer warming differ among forcings. The decrease in radiative cooling (the $\overline{Q_R}/\overline{Q_{\Sigma 0}}$ term) with increasing θ_M is consistent with increased heating of the ML by surface longwave radiation, which increases more rapidly than downward

longwave radiation from the ML itself, because the surface warms more than the ML does. This is particularly important in the case of $\pm c_k$ simulations, where the surface warms much more than the ML, strongly decreasing the average radiative cooling rate of the ML. The increase in convective cooling (the $\overline{Q_C}/\overline{Q_{\Sigma 0}}$ term) with increasing θ_M is consistent with more evaporation of rain in a deeper, drier ML. Only in the case of $\pm g_v$ simulations do changes in ML depth (the $\delta P_M/P_{M0}$ term) dominate changes in cooling rate of the ML, which helps to explain why $\pm g_v$ simulations are fit best by the theory. Ultimately, these significant deviations from constant ML cooling rate do not present an insurmountable problem for the validity of our theory, because the constant cooling rate assumption is largely embedded in the value of γ. Despite the appearance of γ in a number of places throughout the theory, it rarely dominates the full expression for the sensitivity of T_S or θ_M, since it is generally small (~ 0.2) compared to the factor of 1 to which it is added in the expression for λ_E. For the $\pm \alpha$ simulations, the nontrivial changes in θ above the ML (as discussed in Section 4.4.4) help to explain why $\delta P_M/P_{M0}$ in Figure 4-10(b) has a lower slope as a function of $\delta \theta_M$ than in Figures 4-10(a,c). A significant part of the change in θ_M for the $\pm \alpha$ simulations is unrelated to changes in P_M, and occurs simply due to warming of the lower free troposphere.

Another limitation is less visible in the simulation results we have shown, but has somewhat constrained our exploration of parameter space. Generally speaking, the key assumption of a constant θ_T profile is violated in the RC model if there is an abrupt change between deep convection and no deep convection in one column or the other; with similar but more dramatic results than the abrupt changes that were shown when cloud-radiation interactions were enabled. In order to attempt to avoid such cases (which we view as somewhat artificial, related to discretization and the limited number of columns), we have filtered our results for active deep convection in both columns (as diagnosed by a significantly nonzero time-mean updraft mass flux at 700 hPa), and we have also attempted to choose parameters and reference states that ensure some deep convection in both columns. This requirement unfortunately limits the accessibility of surfaces with very low values of g_v, which would theoretically have
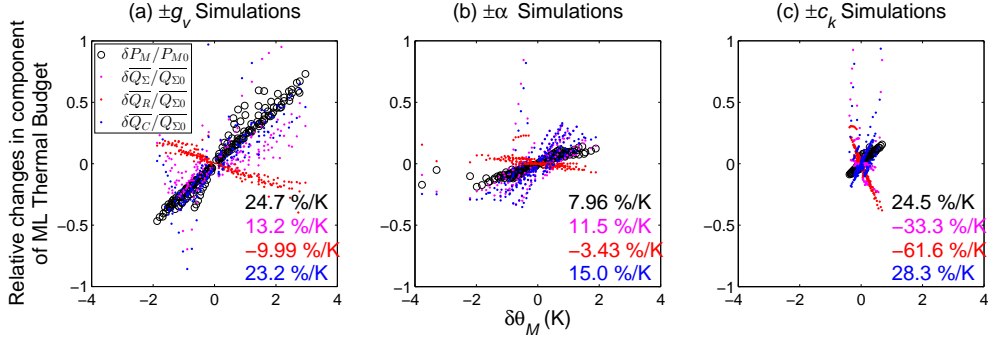
Figure 4-10: Fractional changes in the components of ML thermal balance, $\delta P_M/P_{M0}$ and $\delta\overline{Q_\Sigma}/\overline{Q_{\Sigma0}}$, as given by Equation (4.43), plotted against changes in θ_M, for RC model simulations with no cloud-radiation interactions or diurnal cycle. The change in total ML cooling rate per unit mass, $\delta\overline{Q_\Sigma}/\overline{Q_{\Sigma0}}$, is made up of radiative ($\delta\overline{Q_R}/\overline{Q_{\Sigma0}}$) and convective ($\delta\overline{Q_C}/\overline{Q_{\Sigma0}}$) components. Subfigures are for perturbations of individual surface parameters (a) $\pm g_v$, (b) $\pm\alpha$, and (c) $\pm c_k$, as described in the text. Linear regression of fractional changes of each of the plotted variables provides the slopes given in colored text at bottom right of each subfigure.

high sensitivity to further drying (or other surface parameter changes).

The assumption of a constant θ_T profile, including constant Γ, also prevents the theory from being applied in its present state to perturbations that cause warming or cooling, or affect the lapse rate, of the free troposphere. This means that changes in ML structure due to the long-term effects of CO_2 as a global greenhouse gas will not be captured by the theory we have presented. Sensitivity of boundary layer temperatures to free-tropospheric temperatures is an important problem not only from the standpoint of climate change, but also from a standpoint of understanding how the coupled surface-ML system acts to amplify or dampen synoptic variability, as in heat waves. In its current form, the theory may be useful for understanding the fast component of CO_2-driven greenhouse warming, where land warms but sea surface temperatures remain nearly fixed (*Dong et al.*, 2009; *Wyant et al.*, 2012). Since such warming is driven by a simple longwave radiative perturbation to the surface energy budget, we could calculate the theoretical response by simply plugging in the surface longwave radiative forcing of a step change in CO_2 to the general

sensitivity equation (4.22). As we will discuss later, the theory may also be useful for understanding the non-radiative implications of changes in CO_2 on the surface energy balance (i.e., physiological forcing). It is possible to modify the theory to allow for forcings that impact the free-tropospheric temperature profile, by modifying Equation (4.15) to include a term $\partial \theta_T / \partial A$. We have not included this term because it makes the subsequent derivation more algebraically cumbersome (dq_M / dA is no longer related to $d\theta_M / dA$ by a simple multiplicative factor) than is considered worthwhile for this paper. The calculation of equilibrium boundary layer sensitivity to free-tropospheric temperature represents less an inherent limitation of theory than an opportunity for future valuable work.

A final limitation of the theory is likely evident: by using as the basis for our theory an equilibrium model with diurnally-averaged solar forcing, we do not take into account any nonlinearities associated with the diurnal cycle, which could alter the quantitative sensitivities of the time-mean thermal structure of the boundary layer to the time-mean of the surface fluxes. This might occur in a meaningful way for our theory, for example, if forcings and feedbacks covaried in time (over the course of the day) significantly enough that the covariance terms were large compared to the time-mean terms (our theory considers only the time-mean terms). As noted by B00, it appears that the equilibrium mixed layer model can explain a substantial amount of the variability in daily-average surface temperatures across two basins in the midwestern United States, so there is reason to hope that diurnal nonlinearities are not overwhelming. We have also shown that the sensitivity theory still appears to compare favorably with the time-mean solutions from RC model simulations obtained with diurnally varying radiation, though the theory as applied to $\pm\alpha$ and $\pm c_k$ simulations has reduced skill (Figure 4-9). The similarity of the climatic and diurnal cycle equilbria from *Brubaker and Entekhabi* (1995) lends additional support to the hypothesis that diurnal nonlinearities are not of critical importance for daily-average temperatures. While these are all encouraging signs, neither our simulations with diurnally-varying radiation, nor the work of *Brubaker and Entekhabi* (1995), adequately parameterizes many important aspects of the stable nocturnal boundary

layer. The importance of diurnal nonlinearities for our theory, especially those associated with the stable nocturnal boundary layer, remains an important and open question for future research.

4.5.2 Precipitation, Convection, and Clouds

Plotting changes in precipitation against changes in evaporation reveals a great deal of similarity among the set of simulations with no cloud-radiation interactions and no diurnal cycle (Figure 4-11). Simulations where g_v or c_k are varied roughly obey the simple scaling that $\delta P \approx \delta E$ — precipitation changes approximately equal evaporation changes. This rough equality holds because changes in moisture convergence by the 2-column overturning circulation are small for $\pm g_v$ and $\pm c_k$ simulations. Rough equality of changes in precipitation and evaporation fails to hold for $\pm \alpha$ simulations, where δP changes much more rapidly than δE. Changes in land surface albedo affect atmospheric column energy balance, and thus the moisture converged by overturning circulations, much more strongly than do changes in surface roughness or vegetation conductance. Figure 4-11 also helps to show the typical scales of sensitivity of precipitation to the three land surface parameters. Changes in precipitation are quite small for $\pm c_k$ simulations, intermediate for $\pm g_v$ simulations, and large for $\pm \alpha$ simulations, with the standard deviation of $\sigma_{\delta P} \sim 0.1$, 0.5, and 1.5 mm/day for the three surface parameters, respectively (averaged across all atmospheric boundary conditions).

In simulations where albedo is varied, subcloud quasiequilibrium (*Raymond*, 1995) provides a useful theory with which to diagnose changes in cumulus mass fluxes and, to some extent, precipitation rates. Specifically, we expect that the updraft mass flux at cloud base M_u should equal the large-scale vertical mass flux at cloud base, $-\omega/g$, plus a term related to the surface fluxes divided by the column-average saturation static energy (SSE) deficit:

$$M_u = -\omega/g + \frac{H + E}{b(h^* - h)}. \tag{4.44}$$

Here, b is an unknown factor relating the average SSE deficit in the free troposphere,

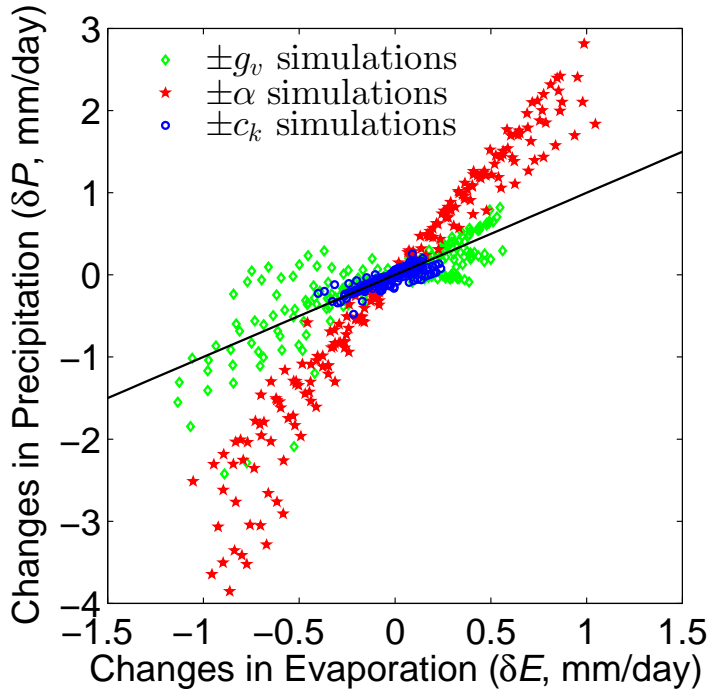Figure 4-11: Scatter plot of changes in precipitation (δP, mm/day) against changes in evaporation (δE, mm/day), for RC model simulations with no cloud-radiation interactions or diurnal cycle. The black diagonal line indicates $\delta P = \delta E$, which is followed roughly for $\pm g_v$ and $\pm c_k$ simulations, but not $\pm \alpha$ simulations, where precipitation changes much more rapidly than evaporation due to changes in overturning circulation strength.

$\overline{h^* - h}$, to the average SSE deficit in downdrafts. With $b \sim 2$, the RHS and LHS of (4.44) agree, as diagnosed from model output. In simulations with varying albedo, we find empirically that we can diagnose changes in precipitation by the approximation:

$$\delta P \sim \delta(M_u q_M). \tag{4.45}$$

In other words, for $\pm \alpha$ simulations, changes in precipitation, δP, appear to scale with changes in the product of cloud base mass flux (M_u) — itself dependent on the total turbulent surface enthalpy flux $H + E$ via 4.44 — and boundary layer specific humidity (q_M).

The RC model simulations with interactions between clouds and radiation allow us to estimate the shortwave feedback λ_{Q_S}, and to understand whether our null

assumption regarding it has significantly affected our theory. We diagnose λ_{Q_S} by linear regression of δQ_S against $\delta\theta_M$ (correcting for any changes in Q_S that are due to changes in α). We find that shortwave feedbacks are a modest but significant positive feedback for $\pm g_v$ and $\pm c_k$ simulations, but a strongly negative feedback for $\pm\alpha$ simulations. A linear model $\delta Q_S = \lambda_{Q_S}\delta\theta_M$ explains the vast majority (80-95%) of the variance in δQ_S, and gives $\lambda_{Q_S} \approx (+6.8, -36.5, +8.6)$ W/m^2/K, for $\pm(g_v, \alpha, c_k)$ simulations, respectively. These results suggest that warming due to reduced g_v or c_k leads to less cloudiness, and that warming due to decreased α leads to more cloudiness. Clearly, the concept of forcing-independent feedbacks does not apply in the case of λ_{Q_S}. For both g_v and c_k, the inferred values for λ_{Q_S} are considerably smaller than typical values of λ_E, so the theory still captures most of the variance in $\delta\theta_M$ and δT_S, even with the assumption $\lambda_{Q_S} = 0$. For α, the value of λ_{Q_S} is quite large, and would tend to make changes in θ_M smaller than our theory would predict with $\lambda_{Q_S} = 0$. We instead see the opposite bias: our theory underestimates the magnitude of $\delta\theta_M$ in Figure 4-8, because of the compensating effects of free-tropospheric temperature changes in $\pm\alpha$ simulations, a somewhat fortuitous cancellation. These results regarding shortwave effects of cloud changes warrant some skepticism, because there is no separate parameterization of shallow cumulus convection in the model; it is likely unrealistic that simulated changes in net shortwave radiation occur principally due to changes in deep clouds.

4.5.3   Applications

The theory presented here potentially has broad quantitative applications to changes in climate driven by land cover changes. Whether land cover change is anthropogenic or natural, it will almost invariably result in concurrent changes in conductance to water vapor, albedo, and surface roughness. Here we will discuss one application, to the subject of changes in climate driven by stomatal closure under elevated CO_2, which has been termed "physiological forcing" of CO_2 by *Betts et al.* (2004) and others (e.g., *Boucher et al.* (2009), *Cao et al.* (2009), *Cao et al.* (2010), *Betts and Chiu* (2010), *Andrews et al.* (2011)).

Numerous experimental studies have found that stomata, the pores in the leaves of plants through which water vapor and CO_2 are exchanged with the atmosphere, tend to close, or reduce in number, as the atmospheric CO_2 concentration increases (e.g., *Field et al.* (1995), *Medlyn et al.* (2001), *Lammertsma et al.* (2011)). Other things equal, this implies a decrease in g_v as CO_2 rises. Several studies have used GCMs to address the question of how much of the warming signal due to elevated CO_2 in model projections can be attributed to the physiological effects of changes in CO_2, typically by contrasting two simulations, both with elevated CO_2. In one simulation, the radiation module of the code sees the elevated CO_2, but the plant physiology module does not; this gives the temperature change due to radiative forcing by CO_2 (ΔT_r in Table 4.5). In the other simulation, both the radiation and plant physiology modules see the elevated CO_2; this gives the temperature change due to both radiative and physiological forcing of CO_2 (ΔT_{rp} in Table 4.5). The difference between these two simulations is considered the climate response to the physiological forcing of elevated CO_2, and is denoted ΔT_{rp-r} in in the bolded column of Table 4.5). *Cao et al.* (2010) cite a subset of the studies summarized in Table 4.5 as representing "an emerging consensus" on the climate impacts of physiological forcing, with the physiological forcing due to a doubling of CO_2 leading to a rise in average surface air temperatures over land of ∼0.4 K; the multi-model mean from the bolded column of Table 4.5 is 0.35 K (halving the result from *Andrews et al.* (2011) from a 4xCO_2 perturbation). Our estimate at the end of section 4.2.5 suggested that a 10% change in $\beta = g_v/(g_a + g_v)$ might be expected to lead to roughly a 0.29 K warming over a moist surface. Using reference-state values of g_v=0.008 m/s and g_a=0.025 m/s, the 20% decrease in g_v under elevated CO_2 reported by *Medlyn et al.* (2001) would translate to a 16% reduction in β, and thus to roughly a 0.5 K warming, similar to the set of GCM results. This, of course, is an extremely crude estimate, as it ignores many of the details of geographic structure that are found in GCM simulations, and no calculation of average g_v over land has been made to justify use of a moist surface, rather than a dry one. The recent studies of *Doutriaux-Boucher et al.* (2009) and *Vila-Guerau de Arellano et al.* (2012) also suggest that changes in clouds can be an

Table 4.5: Survey of studies examining the climate impacts of physiological forcing of elevated CO_2, as in Table 2 of *Cao et al.* (2010). ΔT_r: average warming (K) over land due to radiative effects of elevated CO_2; ΔT_{rp}: average warming (K) over land due to radiative plus physiological effects of elevated CO_2. Difference ΔT_{rp-r} (K) is attributed to physiological forcing of CO_2, with values set in bold for emphasis. *: *Notaro et al.* (2007) also includes changes in leaf area index and vegetation cover **: *Andrews et al.* (2011) is for fast response (limit of no change in SST) only, for $4{\times}CO_2$

Study, Models Used	ΔT_r	ΔT_{rp}	ΔT_{rp-r}	$\%\frac{\Delta T_{rp-r}}{\Delta T_{rp}}$
Sellers et al. (1996), SiB2-CSU GCM	2.6	2.8	**0.2**	7
Cox et al. (1999), MOSES-HadCM2	3.06	3.45	**0.39**	11
Notaro et al. (2007) *, LPJ-PCCM3	2.3	2.7	**0.4**	15
Boucher et al. (2009), MOSES-HadCM3	3.51	4.03	**0.52**	13
Cao et al. (2009), CLM3.0-CAM3.1	2.35	2.47	**0.12**	5
Cao et al. (2010), CLM3.5-CAM3.5	2.86	3.33	**0.47**	14
Andrews et al. (2011) **, HadCM3LC	0.49	1.31	**0.82**	63

important aspect of the global response to physiological forcing by CO_2; we have not considered such changes here.

We also may be able to use our theory to understand why the results of *Betts and Chiu* (2010) — approximately a 4 K increase in a doubled-CO_2 scenario — are so much larger than the "emerging consensus" suggested by Table 4.5. First, the reduction in g_v in their study is quite large — roughly $60 - 70\%$ – compared to what typically is found by GCMs. Second, in spite of a low reference-state $g_v \sim 0.003$ m/s, their model still has a value of $E_0 \approx 113$ W/m^2. This results in an extremely large forcing of ~ 115 W/m^2 (note that for very large changes in g_v, the forcing can exceed the reference-state latent heat flux, since the magnitude of the logarithmic term in (4.29) can exceed 1). Because the reference value of g_{v0} in *Betts and Chiu* (2010) is so small, their evaporative feedback is relatively weak; we estimate $\lambda_E \sim 19$ W/m^2/K. Together with a sensible heat flux feedback of ~ 6 W/m^2/K (as above), this gives a very large expected warming, of ~ 4.6 K. This is larger than the additional warming of 4 K that they simulate, likely because of differences in the values of γ and ξ, and the potential for numerical errors in estimation from graphs. Our theory thus suggests that a combination of a large forcing, together with a relatively weak evaporative feedback, is likely the essential mechanism that gives rise to the "unrealistically large"

98

climate response to physiological forcing in the study of *Betts and Chiu* (2010).

4.6 Conclusions

We have briefly presented a framework for calculating the boundary layer climate sensitivity, and then developed in detail a analytic theory of boundary layer climate sensitivity, based on the diurnally-averaged model of B00. The theory is developed analogously to climate sensitivity, but based on surface energy balance, rather than top-of-atmosphere energy balance. The theory identifies forcings associated with changes in land surface properties, including conductance to water vapor, albedo, and aerodynamic roughness, and identifies feedbacks associated with each of the four components of surface energy balance (latent and sensible turbulent heat fluxes, long-wave and shortwave radiative fluxes). As in the work of *Brubaker and Entekhabi* (1996) and *Kim and Entekhabi* (1998), we find that a strongly negative evaporative feedback (λ_E), related to the dependence of saturation specific humidity on temperature, usually plays the dominant role in limiting the response of surface temperatures to a perturbation in surface properties. We find extremely good agreement between the theory and the more complex set of equations from B00 on which it is based, and find that allowing for forcings that are nonlinear functions of surface properties is key to obtaining good agreement for large perturbations in surface properties. The importance of nonlinear forcings represents an interesting further analogy to climate sensitivity. We have also performed simulations with a two-column RC model with many more degrees of freedom, which supports the general utility of the theory even when many of the assumptions upon which it is based are no longer strictly enforced.

Although the theory has a number of limitations, we believe that it may be broadly useful for unifying our understanding of how changes in land use or ecosystem function may affect changes in climate. As an example case, we explore the application of the theory to the problem of climate change driven by suppression of surface conductance to water vapor under elevated CO_2 (physiological forcing). We find that our theory provides a reasonable estimate of the warming simulated by past studies that have

used global models, and may help to explain why the warming in the simpler study of *Betts and Chiu* (2010) is so large. Directions for future work include application to problems such as urbanization, agricultural expansion, and afforestation, as well as extension of the theory to examine forcing by free-tropospheric temperature change. Even if the quantitative expressions for feedbacks and forcings presented here prove to be quite different from those calculated from GCMs, we hope that the framework of boundary layer climate sensitivity will help to standardize how climate changes induced by land cover changes are assessed in modeling studies.

4.7 Appendix: Details of Sensitivity Theory

4.7.1 Derivation of ξ

Here, we derive ξ, the parameter relating changes in q_M to changes in θ_M in Equation (4.20). Expanding (4.19) gives:

$$\frac{dq_M}{dA} = \frac{\epsilon}{p_b} \left. \frac{\partial e^*}{\partial T} \right|_{T_b} \frac{dT_b}{dA} - \frac{\epsilon e^*(T_b)}{p_b^2} \frac{dp_b}{dA}. \tag{4.46}$$

Using (4.15), and the definition of $p_b = p_s - P_M$, we can replace dp_b/dA with $-\Gamma(d\theta_M/dA)$. Using the definition of T_b from (4.18), we have:

$$\begin{aligned}
\frac{dT_b}{dA} &= \left(\frac{p_b}{p_s}\right)^{\frac{R}{c_p}} \left(\frac{d\theta_M}{dA} + \frac{R\theta_M}{c_p p_b} \frac{dp_b}{dA}\right) \\
&= \left(\frac{p_b}{p_s}\right)^{\frac{R}{c_p}} \left(1 - \frac{R\theta_M}{c_p p_b \Gamma}\right) \frac{d\theta_M}{dA}.
\end{aligned} \tag{4.47}$$

Putting this back into (4.46) gives:

$$\frac{dq_M}{dA} = \left[\left. \frac{\partial q^*}{\partial T} \right|_{T_b} \left(\frac{p_b}{p_s}\right)^{\frac{R}{c_p}} \left(1 - \frac{R\theta_M}{c_p p_b \Gamma}\right) + \frac{q_M}{p_b \Gamma}\right] \frac{d\theta_M}{dA}, \tag{4.48}$$

where we have again used $q^* = \epsilon e^*/p$ and $q_M = q^*(T_b, p_b)$ to simplify the expression. The term in square brackets in (4.48) is defined as ξ.

4.7.2 Expansion of Surface Energy Balance

The total derivatives in (4.4) can be expanded by the chain rule:

$$\frac{dQ_S}{dA} = \frac{\partial Q_S}{\partial A} + \frac{\partial Q_S}{\partial T_S}\frac{dT_S}{dA} + \frac{\partial Q_S}{\partial \theta_M}\frac{d\theta_M}{dA} + \frac{\partial Q_S}{\partial q_M}\frac{dq_M}{dA} \tag{4.49}$$

$$\frac{dQ_L}{dA} = \frac{\partial Q_L}{\partial A} + \frac{\partial Q_L}{\partial T_S}\frac{dT_S}{dA} + \frac{\partial Q_L}{\partial \theta_M}\frac{d\theta_M}{dA} + \frac{\partial Q_L}{\partial q_M}\frac{dq_M}{dA} \tag{4.50}$$

$$\frac{dH}{dA} = \frac{\partial H}{\partial A} + \frac{\partial H}{\partial T_S}\frac{dT_S}{dA} + \frac{\partial H}{\partial \theta_M}\frac{d\theta_M}{dA} + \frac{\partial H}{\partial q_M}\frac{dq_M}{dA} \tag{4.51}$$

$$\frac{dE}{dA} = \frac{\partial E}{\partial A} + \frac{\partial E}{\partial T_S}\frac{dT_S}{dA} + \frac{\partial E}{\partial \theta_M}\frac{d\theta_M}{dA} + \frac{\partial E}{\partial q_M}\frac{dq_M}{dA}. \tag{4.52}$$

For a typical choice of A, many of these terms vanish, but all are retained here for generality. We can eliminate dT_S/dA and dq_M/dA from these expressions in favor of $d\theta_M/dA$, using (4.16) and (4.20). After rearranging to move the differential dA to the right hand side, this gives:

$$
\begin{aligned}
dQ_S &= \left(\frac{\partial Q_S}{\partial A} - \frac{1}{\rho c_p g_a}\frac{\partial Q_S}{\partial T_S}\frac{\partial H}{\partial A}\right)dA \\
&+ \left((1+\gamma)\frac{\partial Q_S}{\partial T_S} + \frac{\partial Q_S}{\partial \theta_M} + \xi\frac{\partial Q_S}{\partial q_M}\right)d\theta_M \\
&\equiv dF_{Q_S}^A + \lambda_{Q_S}d\theta_M \tag{4.53} \\
dQ_L &= \left(\frac{\partial Q_L}{\partial A} - \frac{1}{\rho c_p g_a}\frac{\partial Q_L}{\partial T_S}\frac{\partial H}{\partial A}\right)dA \\
&+ \left((1+\gamma)\frac{\partial Q_L}{\partial T_S} + \frac{\partial Q_L}{\partial \theta_M} + \xi\frac{\partial Q_L}{\partial q_M}\right)d\theta_M \\
&\equiv dF_{Q_L}^A + \lambda_{Q_L}d\theta_M \tag{4.54} \\
dH &= \left(\frac{\partial H}{\partial A} - \frac{1}{\rho c_p g_a}\frac{\partial H}{\partial T_S}\frac{\partial H}{\partial A}\right)dA \\
&+ \left((1+\gamma)\frac{\partial H}{\partial T_S} + \frac{\partial H}{\partial \theta_M} + \xi\frac{\partial H}{\partial q_M}\right)d\theta_M \\
&\equiv dF_H^A + \lambda_H d\theta_M \tag{4.55} \\
dE &= \left(\frac{\partial E}{\partial A} - \frac{1}{\rho c_p g_a}\frac{\partial E}{\partial T_S}\frac{\partial H}{\partial A}\right)dA \\
&+ \left((1+\gamma)\frac{\partial E}{\partial T_S} + \frac{\partial E}{\partial \theta_M} + \xi\frac{\partial E}{\partial q_M}\right)d\theta_M \\
&\equiv dF_E^A + \lambda_E d\theta_M, \tag{4.56}
\end{aligned}
$$

Where the terms including a factor of dA (4.53)-(4.56) have been defined as differential forcings ($dF_{Q_S}^A$, $dF_{Q_L}^A$, dF_H^A, and dF_E^A); and the terms multiplying the differential change in potential temperature, $d\theta_M$, have been defined as feedbacks (λ_{Q_S}, λ_{Q_L}, λ_H, and λ_E). Note that we have kept the symmetry of the equations for clarity, but we can make one general simplification immediately from the definition of H: $dF_H^A = 0$, since $\partial H/\partial T_S = \rho c_p g_a$. However, the impacts of $\partial H/\partial A$ are distributed over the other terms $dF_{Q_S}^A$, $dF_{Q_L}^A$, and dF_E^A.

Now, applying surface energy balance (4.3), we can obtain:

$$dQ_S - dQ_L - dH - dE = 0 \tag{4.57}$$

$$dF_{Q_S}^A - dF_{Q_L}^A - dF_E^A + (\lambda_{Q_S} - \lambda_{Q_L} - \lambda_H - \lambda_E)d\theta_M = 0 \tag{4.58}$$

$$\frac{dF_{Q_S}^A - dF_{Q_L}^A - dF_E^A}{\lambda_{Q_L} + \lambda_H + \lambda_E - \lambda_{Q_S}} = d\theta_M, \tag{4.59}$$

where the last step has assumed the feedbacks are nearly constant, so that we can rearrange them before integration. Integration of $d\theta_M$ simply yields $\theta_M - \theta_{M0} \equiv \delta\theta$. Full integration of the differential forcings gives the results quoted in the main text, Equation (4.23). We could also assume that the forcings were linear in $A - A_0 \equiv \delta A$, so that:

$$F_{Q_S,lin}^A \equiv \left(\frac{\partial Q_S}{\partial A} - \frac{1}{\rho c_p g_a} \frac{\partial Q_S}{\partial T_S} \frac{\partial H}{\partial A} \right) \delta A$$

$$F_{Q_L,lin}^A \equiv \left(\frac{\partial Q_L}{\partial A} - \frac{1}{\rho c_p g_a} \frac{\partial Q_L}{\partial T_S} \frac{\partial H}{\partial A} \right) \delta A$$

$$F_{E,lin}^A \equiv \left(\frac{\partial E}{\partial A} - \frac{1}{\rho c_p g_a} \frac{\partial E}{\partial T_S} \frac{\partial H}{\partial A} \right) \delta A \tag{4.60}$$

In parallel with the nonlinear-forcing derivations of Sections 4.2.5-4.2.7, expressions for total linear forcings with $A \to (g_v, \alpha, g_a)$ are given by:

$$F_{lin}^{g_v} = \frac{g_a}{g_a + g_{v0}} E_0 \frac{\delta g_v}{g_{v0}}$$

$$F_{lin}^{\alpha} = -\frac{Q_{S0}}{1 - \alpha_0} \delta\alpha$$

$$F_{lin}^{g_a} = \frac{g_v}{g_{a0} + g_v}\left(E_0 - \frac{H_0}{B_e}\right)\frac{\delta g_a}{g_{a0}} - \frac{4\sigma_B T_{S0}^3 H_0}{\rho c_p g_{a0}}\frac{\delta g_a}{g_{a0}}. \tag{4.61}$$

For brevity here, we have summed the forcings from different surface fluxes. As discussed in Section 4.3, the usage of linear forcings is generally inferior to the use of the fully nonlinear forcings described in detail in Sections 4.2.5-4.2.7 and Table 4.2. We include the expressions for linear forcings here to clarify the methodology underlying the calculation of the results shown in Figures 4-2 and 4-3.

Chapter 5

Island Precipitation Enhancement and the Diurnal Cycle in Radiative-Convective Equilibrium

Abstract

Tropical islands are observed to be rainier than nearby ocean areas, yet reasons for this island rainfall enhancement remain unclear. Here, we explore how a highly idealized island, which differs from the surrounding ocean only in heat capacity, could rectify the diurnal cycle and influence the tropical climate, especially the spatial distribution of rainfall. To explore these issues, we perform simulations of radiative-convective equilibrium with the System for Atmospheric Modeling (SAM) cloud-system-resolving model, with interactive surface temperature, where a highly idealized, low heat capacity circular island is embedded in a slab-ocean domain. We find that the precipitation rate over the island can be more than double the domain average value, with island rainfall occurring primarily in an intense, regular thunderstorm system that occurs in the afternoon to early evening each day. Island size affects the magnitude of simulated island rainfall enhancement, the intensity of the convection, and the timing of the rainfall maximum relative to solar noon. We discuss both dynamic and thermodynamic mechanisms for the enhancement of island rainfall, including the important finding that that the upper troposphere typically warms with the inclusion of an island, which may have implications for large-scale overturning circulations in the tropics. We also extend

---

This chapter is in preparation for submission to the *Journal of the Atmospheric Sciences.*

previous work on the linear theory of the land-sea breeze to use as a tool for understanding our results.

5.1   Introduction

Across a range of time scales, ranging from brief and intense convective rainfall, to annual climatology, tropical islands are some of the rainiest places in the world. *Sobel et al.* (2011) examined a high-resolution dataset of satellite observations from the Tropical Rainfall Measurement Mission (TRMM), and found that small islands are typically climatologically rainier than nearby ocean areas, with this contrast increasing with both island size and island elevation. In general, land is rainier than ocean in the deep tropics; *Wang et al.* (2014) find that in the latitudinal band from 10°S-10°N, rainfall over ocean averages 4.28 mm/day, while rainfall over land is 12% higher, at 4.79 mm/day. The land-ocean contrast in rainfall rises in both an absolute and relative sense when considering the islands and shallow seas of the Maritime Continent (MC) in the Western Pacific. In a study of rainfall over the MC region, *As-syakur et al.* (2013) found an average rainfall of 5.47 mm/day over ocean, but a 40% higher average value of 7.62 mm/day over islands. Though small islands tend to have higher rainfall rates when they have substantial topography, no correlation between elevation and mean rainfall was found over the islands of the MC by *As-syakur et al.* (2013), in agreement with previous findings of *Dayem et al.* (2007).

Because atmospheric convective heating and mean ascent over the MC plays a major role in the atmospheric general circulation, it is slightly troubling that this observed land-ocean contrast in mean rainfall is poorly represented in general by global models, which often suffer a dry bias over the MC region (*Neale and Slingo*, 2003). The timing of the observed diurnal cycle of convective rainfall over islands and tropical land (e.g., *Yang and Slingo* (2001), *Biasutti et al.* (2012)) is also generally poorly reproduced by global models (e.g., *Liu and Zipser* (2008), *Guichard et al.* (2004), *Dirmeyer et al.* (2012)). Connecting these ideas has led to hypotheses that the diurnal cycle may be important for the enhancement of time-mean precipitation

or convective intensity over islands (*Neale and Slingo*, 2003; *Qian*, 2008; *Robinson et al.*, 2008), and that this may also be a missing factor in climate models. The mechanisms responsible for such "rectification" of the diurnal cycle, however, remain somewhat murky, and the hypotheses of different authors are somewhat divergent.

Neale and Slingo (2003) conducted a General Circulation Model (GCM) experiment, with a GCM that systematically underestimates precipitation over the MC, and found that even a threefold increase in resolution did not ameliorate the problem. Replacing islands in the MC with ocean, however, improved the simulation, both locally and remotely; deficiencies in model physics and parameterizations are likely at least equal culprits with inadequate resolution. On the other hand, *Qian* (2008) performed a regional climate simulation (with parameterized convection) of Java and found that precipitation was substantially underestimated in model runs with flat topography, and was reduced even further in runs where the island was replaced with ocean, suggesting that topography, and thus at least moderately high resolution, is key to capturing the distribution of precipitation over the islands of the MC, and that the physics and parameterizations are adequate – essentially the opposite conclusion from that of *Neale and Slingo* (2003). The study of *Robinson et al.* (2008) is more theoretical, and is based on the idea that the diurnally oscillating sensible heat flux over islands could lead to a resonance for islands of a certain spatial scale, leading to locally enhanced convective intensity. A common thread in all three of these studies, as well as other work on modeling of precipitation over tropical islands (*Sato et al.*, 2009; *Robinson et al.*, 2011), is invocation of the importance of dynamical convective forcing due to low-level convergence of land-sea and mountain-valley breezes. However, the complexity of such circulations in real terrain, especially in concert with other differences between the land and ocean lower boundaries, makes it difficult to precisely identify whether or not such forcing is a primary or essential mechanism of rectification. The goal of this paper is to explore rectifying mechanisms due to interaction of the diurnal cycle of solar insolation and the low heat capacity of an island surface, which can lead to a time-mean precipitation enhancement and ascent over islands.

A related motivation for studying island rainfall, and particularly rainfall over the islands such as those that constitute the MC, lies in the potential for linkage between the tectonic and climatic changes of the past several million years. One of the most notable tectonic changes of the past few million years is the steady northward motion of New Guinea and the Australian plate, and the related emergence of many small islands in the MC (*Hall*, 2002). The climate of the early Pliocene may have resembled a "permanent El Niño" state, with much higher sea surface temperatures in the East and Central Pacific, warmer global-mean surface air temperatures, and much smaller global ice volume (*Fedorov et al.*, 2006). *Dayem et al.* (2007) found that precipitation over the MC, rather than precipitation over the pacific warm pool, best correlates with variability in the strength of the Walker Circulation, and thus hypothesized that reorganization of the MC could have "provided a necessary condition for the onset of the Walker Circulation," contributing to a shift out of the "permanent El Niño" regime of the early Pliocene. The extent to which changes in island area and configuration could have contributed to the large-scale atmospheric circulation changes of the past few million years remains a largely unanswered question.

We should note that extensive study of rainfall over islands has been conducted before, with our understanding of the dynamics of deep convection and rainfall over flat islands greatly improved by the Maritime Continent Thunderstorm Experiment (MCTEX). MCTEX was conducted in late 1995 over the Tiwi Islands of northern Australia, which are relatively flat, and about 150 km long by 50 km wide. MCTEX focused on the remarkable regular convective system known as Hector, which is one of the most intense and predictable mesoscale convective systems in the world; Hector occurred every day during the 2-week intensive observational period from 20 November to 4 December 1995 (*Keenan et al*, 2000). Studies of Hector have considered the problem of island rainfall from observational, theoretical, and numerical modeling standpoints, and have considered the importance of many processes, including cumulus merger (*Simpson et al.*, 1993), convective triggering by sea breezes (*Carbone et al.*, 2000; *Crook*, 2001), aerosol-cloud-precipitation interactions (*Connolly et al.*, 2006), and surface energy budget (*Beringer and Tapper*, 2002). But studies relat-

ing to Hector, as well as other less geographically specific work on island convection (*Robinson et al.*, 2008, 2011, 2013), has generally shared a focus on weather time scales, where island convection is an initial value problem. We would like to consider climate time scales, where island rainfall becomes a boundary value problem. Thus, we will generally opt to focus on the time-mean impacts of an island on the atmospheric thermal structure and distribution of rainfall, rather than on the dynamics of individual mesoscale convective systems.

In this paper, we perform simulations of Radiative-Convective Equilibrium (RCE), where a low-heat capacity island is embedded in a slab-ocean domain. By varying island size, this experimental setup allows us to explore several aspects of the problem of island rainfall, including mechanisms for enhancement of time-mean rainfall, differences in convective intensity over land and ocean, and controls on the afternoon timing of the rainfall peak over land. In the context of our simulations, we also explore whether the dynamics of the linear land and sea breeze can be used as tools to understand any of these effects. We first describe the details of the design of simulation experiments (Section 5.2), and then present results, first for a reference-case island (Section 5.3.1), and then across a range of island sizes (Section 5.3.2). We then discuss in detail mechanisms for time-mean rainfall enhancement over the island, and the finding that the troposphere typically warms with the inclusion of an island (Sections 5.4 and 5.5). We develop and extend the theory of the linear land and sea breeze, including a comparison of linear and nonlinear terms in the budget equation for surface winds (Section 5.6). We also examine the diurnal phase relations among key variables, including simple models for important phase lags (Section 5.7). Finally, in Section 5.8, we review our key findings, and discuss possible directions for future work.

5.2 Methods

We conduct simulations of statistical radiative-convective equilibrium (RCE) using version 6.8.2 of the System for Atmospheric Modeling (SAM, *Khairoutdinov and Ran-*

dall (2003)) cloud-system-resolving model. In all of our simulations, the domain is doubly-periodic, 384 by 384 km in size, and has a stretched grid with 64 levels in the vertical. We perform simulations with a relatively coarse horizontal resolution of 3 km, with non-rotating dynamics, and no background flow. We use the CAM radiation package, with the mixing ratio of CO_2 fixed at 355 ppm, and the SAM 1-moment microphysics parameterization.

We break from the traditional setup of RCE by using interactive surface temperatures everywhere in the domain; the model explicitly solves a prognostic equation for slab surface temperature T_S in each grid cell:

$$C_S \frac{\partial T_S}{\partial t} = Q_S - Q_L - H - E, \tag{5.1}$$

where Q_S is the net shortwave radiation at the surface (positive downwards), Q_L is the net longwave radiation at the surface (positive upwards), H is the surface sensible heat flux, and E is the surface latent heat flux (turbulent fluxes positive upwards). Spatial variation in surface heat capacity, C_S, defines the geometry of the island; we set $C_{SO} =1$ meter-water-equivalent (m.w.e.) for ocean grids (4.2×10^6 J m^{-2} K^{-1}), and $C_{SL} =0.05$ m.w.e. for land grids (2.1×10^5 J m^{-2} K^{-1}). Our choice of C_{SO} is much smaller than the $\sim$50 m.w.e. that ought to be used to represent the ocean mixed layer, but use of such a deep slab would result in excessively long equilibration times, and 1 m.w.e. is sufficiently large to limit the amplitude of the diurnal cycle of T_S over the ocean to $\sim$ 1 K (see Chapter 3 for a discussion of the time scale of approach to radiative-convective equilibrium with an interactive surface). The choice of C_{SL} is based on the product of the penetration depth of an oscillating thermal forcing into a uniform diffusive medium, and the volumetric heat capacity of the medium. For soil, the penetration depth scale is $z(\omega) = \sqrt{2D/\omega} \approx 11$ cm (based on an angular frequency of $\omega = 2\pi/\text{day}$ and a soil thermal diffusivity $D = 5 \times 10^{-7}$ m^2/s), and the volumetric heat capacity is $\sim 2 \times 10^6$ J m^{-3} K^{-1} (typical soil values from *Ochsner et al.* (2001)).

Simulation of RCE with interactive surface temperatures and a realistic choice of

110

tropical insolation (e.g., $\overline{I} \sim 420$ W m^{-2}) is likely to result in a runaway greenhouse, since net solar absorption, $(1 - \alpha_P)\overline{I}$, far exceeds the threshold of roughly 310 W m^{-2} for Earth's dry atmospheric composition and surface gravity (see section 4.6 of *Pierrehumbert* (2010)). This problem is rarely broached in the literature, because in the context of tropical meteorology, RCE is usually computed with a fixed surface temperature, and thus the surface implicitly acts as an energy sink that adjusts in magnitude exactly as needed to hold surface temperatures fixed. There are three broad methods by which we can lower the energy input to the system and avoid thermal runaway. The first is to artificially raise the planetary albedo, α_P; this could be accomplished in SAM by increasing the surface albedo considerably. This option is not as straightforward as it might seem, due to the requirement that one must account for the shortwave opacity of the atmosphere (itself a function of temperature in RCE, and dependent on cloud properties) in calculating the surface albedo required to change the planetary albedo by a specified amount (*Donohoe and Battisti*, 2011). Modification of surface albedo also has the potential to lead to biases in the net energy balance of the atmosphere by increasing shortwave absorption, which could be problematic for large $\overline{I}$. The second approach, as taken by *Romps* (2011), is to prescribe a surface energy sink, based on an initial simulation with surface temperatures fixed near desired values. This is likely a better option in general, as it parameterizes the real heat export that occurs in the tropical atmosphere-ocean system, but it makes little sense in our case to prescribe a surface energy sink over land. The third approach, which we take, is to dial down the insolation considerably. For calculations of solar zenith angle, we use a latitude of 45° N on the spring equinox (julian day 80), resulting in a time-mean insolation $\overline{I}$ =310.3 W m^{-2}. While this choice still has the potential to lead to biases (e.g., in cloud radiative effects), we think it is the best option of the three that are available. With these choices, the sun rises at 6 hours local solar time (LST), top-of atmosphere insolation is maximum at 974.4 W/m^2 at 12 hours LST, and the sun sets at 18 hours LST.

We generally perform simulations for 250 days, and the time-mean of output variables such as precipitation indicates an average over the last 125 days of the

simulation. In all of the simulations that will be shown here, we use islands that are approximately circular – to the extent allowed by a cartesian grid – but earlier simulations with a square island (not shown here), suggested that our major results are not qualitatively sensitive to details of island geometry. Our reference-case island has a radius $r_I = 48$ km, and thus occupies less than 5% of the total area of domain.

5.3 Results

Many of the features of the statistical RCE states we simulate over mixed land-ocean surfaces can be summarized by visualizations of the evolution of the cloud and surface air temperature fields over a period of a few days. Here, we briefly describe the phenomenology of the convection in the statistical RCE state, before moving on to discuss some of the results in detail for the reference-case island (Section 5.3.1), and then across a range of island sizes (Section 5.3.2).

The island disrupts the background RCE state, of pseudo-random convection over the remote ocean, where clouds of different size and separation scales grow and decay at all times of day. Over the island, clouds and surface air temperature have a distinct, repeating pattern from day to day (see movie of cloud and surface air temperature evolution over a 2-day "intensive observation period" at: `http://mit.edu/~twcronin/Public/IPEmovie.mp4`). This pattern is at least superficially consistent with the "cumulus merger" hypothesis of *Qian* (2008), which ascribes increased island rainfall to merging of individual cumulus cells over the course of the day. Clouds initially form at around noon at low levels, around the perimeter of the island, likely in association with the sea breeze. In the early afternoon, these shallow clouds develop into deeper isolated precipitating convective cells. In the late afternoon to early evening, these isolated cells appear to merge together near the center of the island, forming a large, heavily raining, continuously cloudy region of deep convection and strong updrafts. As rainfall over the island peaks in the early evening, a mesoscale cold pool forms and spreads offshore, abruptly reversing the sea breeze, and propagating as much as 100 km before decaying into the background

112

RCE state of distributed random convection. Overnight, there are few clouds over the island, and the boundary layer over the island cools, with a land breeze peaking in strength near dawn. As the sun rises, and boundary layer over the island is again heated and moistened by turbulent enthalpy fluxes, the cycle repeats. The regular island thunderstorm in our simulations shares many features with real-world convection over flat islands, especially as observed in the regular convective system known as "Hector" over the Tiwi Islands off Australia, which has been the subject of intensive observational study in the Maritime Continent Thunderstorm Experiment (*Keenan et al*, 2000; *Carbone et al.*, 2000).

5.3.1 Reference-Case Island

Regular afternoon convection over the island is associated with a marked change in the time-mean distribution of rainfall across the domain. The simulation with the reference-case island ($r_I = 48$ km) shows a strong enhancement of the time-mean rainfall rate over the island (6.17 mm/day), as compared to the time-mean rainfall rate over the ocean (2.94 mm/day; see Figure 5-1). Figure 5-1(b) suggests that the moisture to supply this enhanced rainfall is "stolen" from an annular ocean region just surrounding the island, forming a dry ring with markedly lower rainfall rates than the domain-average. Along with the enhancement of mean rainfall over the island, there is also mean ascent over the island in the mid-troposphere; the compensating subsidence mostly occurs in the nearby dry ring, but about a quarter of the subsidence occurs remotely, in the regions furthest away from the island. The time-mean circulation has ascent over the island in the mid-troposphere, but subsidence near the surface, where the divergent mesoscale cold pool and land breeze overwhelm the convergent sea breeze. Convection over the island is thus associated with a circulation that has multiple components, with different spatial scales in both the vertical and the horizontal.

Convection over the island is also considerably more intense than convection over the ocean. We define metrics of convective intensity as high quantiles of surface precipitation rate P, cloud-top height Z_{top}, and vertical velocity at 500 hPa w_{500}
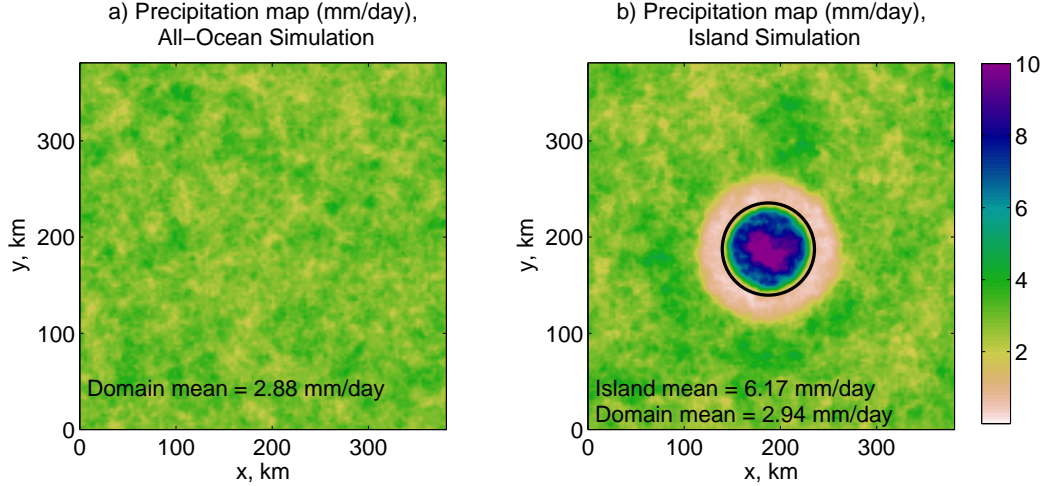
113

Figure 5-1: Map of time-mean precipitation rate at the surface for a) control simulation with a homogeneous slab-ocean surface, and b) the reference-case island simulation with r_I =48 km (the spatial extent of the island is denoted by the black circle on subfigure b)). Text on a) indicates the time-and spatial-mean precipitation rate for all grid cells; corresponding text on b) also includes the time-and spatial-mean precipitation rate for island grid cells only.

(Table 5.1). The contrast is particularly sharp at the upper tail of the distributions: the 1-in-10,000 hour ocean precipitation event is nearly matched by the 1-in-1,000 hour island precipitation event, and similar statements hold for cloud-top height and vertical velocities. The values in Table 5.1 for high quantiles of P, Z_{top}, and w_{500} for the ocean have been determined based on the ocean grid cells in the reference-case island simulation, but values from the all-ocean control simulation do not differ very much. The contrast between island and ocean convective intensity in our reference-case island simulation is consistent with the study of *Williams* (2004), who noted that lightning flash rates typically increase with island size, and the transition from maritime to continental lightning regimes occurs for an island size around 100-1000 km^2; our reference-case island, with an area of 7308 km^2, is well above this transition point.

The timing of precipitation over the island is dominated by the recurring afternoon convective system. Figure 5-2 shows the average hourly distribution of rainfall and clouds over the island, ocean, and entire domain; nearly all of the precipitation over

114

Table 5.1: Convective intensity metrics for reference-case island simulation, as measured by high quantiles of surface precipitation rate P (mm/hour), cloud-top height Z_{top} (km), and 500-hPa vertical velocity w_{500} (m/s). Note that while P and w_{500} have continuous distributions, Z_{top} is quantized by the position of model levels. Cloud-top height is defined in SAM as the first model level, marching downwards, where the total overhead cloud ice plus water path exceeds 10 g/m^2.

Quantile	P, mm/hour		Z_{top}, km		w_{500}, m/s	
	Island	Ocean	Island	Ocean	Island	Ocean
90%	0.078	0.0068	10.5	8.96	0.121	0.098
99%	6.99	3.67	13.0	11.5	0.902	0.369
99.9%	17.9	10.7	14.0	13.0	2.66	1.59
99.99%	30.4	18.0	15.0	13.5	4.17	2.86

the island falls in the late afternoon to early evening. The sky over the island is nearly devoid of clouds until noon, and then cloud fraction increases abruptly in the afternoon, peaking just after sunset, roughly an hour after the peak in island-average precipitation rate. The diurnal cycle of rainfall and clouds is less dramatic over the ocean, but oceanic rainfall has a nocturnal maximum, and is markedly suppressed during the afternoon-evening island convective maximum.

5.3.2   Island Size Sensitivity Experiments

Simulations for islands of different sizes show many similar features, though the mean rainfall enhancement, convective intensity, and timing of the peak rainfall, all vary considerably with island radius. The simulated island rainfall enhancement is due to both an increase in time-mean evaporation from the island surface, as well as a larger component of time-mean atmospheric moisture convergence (Figure 5-3). Most of the scaling of evaporation enhancement with island radius is related to the timing of clouds and convective rainfall over the island: when cloud fraction peaks closer to sunset, as for the larger islands, clouds trap outgoing longwave radiation more effectively than blocking incoming shortwave radiation, enhancing evaporation; when cloud fraction peaks closer to noon, clouds block incoming shortwave radiation more effectively than trapping outgoing longwave radiation, suppressing evaporation. This scaling of evaporation with island size will be elaborated upon later. The enhance-
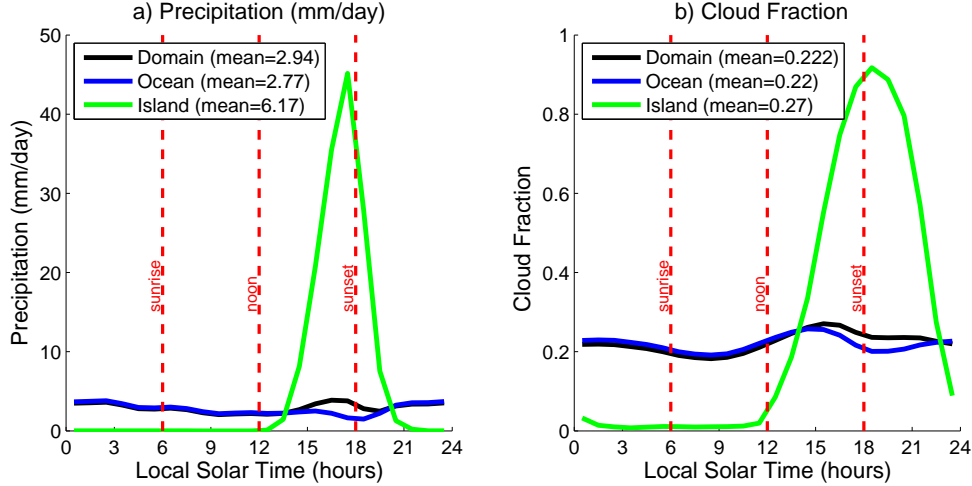
115

Figure 5-2: Composites for each hour of the day for island grid cells (green), ocean grid cells (blue), and all grid cells (black), in the reference-case island simulation with r_I =48 km. Subplots show a) average precipitation rate (mm/day), and b) average fraction of grid cells that are cloudy. Red dashed vertical lines indicate timing of sunrise, sunset, and local solar noon.

ment of evaporation for most island sizes can also be readily explained, but the finding is somewhat counterintuitive and will be discussed below (see Section 5.4). The dominant component of precipitation enhancement, atmospheric moisture convergence, does not scale, as might be expected, with the column-integrated atmospheric energy surplus over the island. Rather, the shape of the $P - E$ curve as a function of r_I strongly resembles the shape of the "resonant" response of convective intensity to island size in *Robinson et al.* (2008), suggesting that sea-breeze dynamics may be important to the time-mean atmospheric moisture convergence. We will explore this hypothesis in more detail below (see Section 5.4).

Looking at extremes of vertical velocity and surface precipitation rate as metrics of convective intensity, we see that although both metrics agree that island convection is more intense than convection over the ocean over a large range of island radii, the two measures of convective intensity do not scale in quite the same way with island size (Figure 5-4). Specifically, the extremes of 500-hPa vertical velocity peak at a relatively small island radius, of ∼20-30 km, while the extremes of precipitation rate peak for almost the largest island; the decline in precipitation rate extremes from
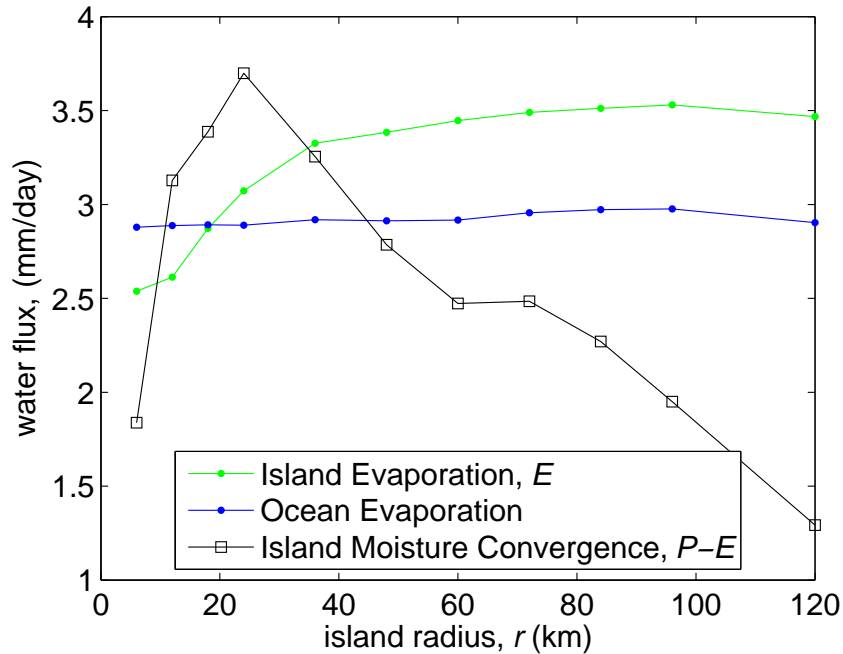
116

Figure 5-3: Plot of island evaporation, E (green), atmospheric moisture convergence over the island, $P - E$ (black), and ocean evaporation rate (blue), all in mm/day, against island radius, r_I. Evaporation from the island surface is generally slightly larger than evaporation from the surrounding ocean, though this inequality is reversed for the smallest islands.

r_I=96 km to 120 km may be related to the finite domain size.

We quantify the timing of the maxima of a variable as the phase of the first Fourier component of a diurnal composite of that variable. This represents a more synthetic measure of the timing of a variable like rainfall, than the alternative of simply taking the hour of maximum precipitation; this latter choice would be resolution-limited by the frequency of our data output (1/hour), and would thus shift abruptly.

For all island sizes, a chain of lags connects peak solar insolation to peak precipitation and clouds: surface shortwave radiation peaks at nearly noon, the surface turbulent fluxes respond by peaking some time later, precipitation lags the surface enthalpy flux maximum, and then cloud fraction lags peak rainfall (Figure 5-5). Surface solar radiation peaks slightly before noon, because cloud fraction is greater in the afternoon than in the morning, blocking solar energy from reaching the surface. The phase lag of surface enthalpy fluxes relative to surface shortwave radiation is
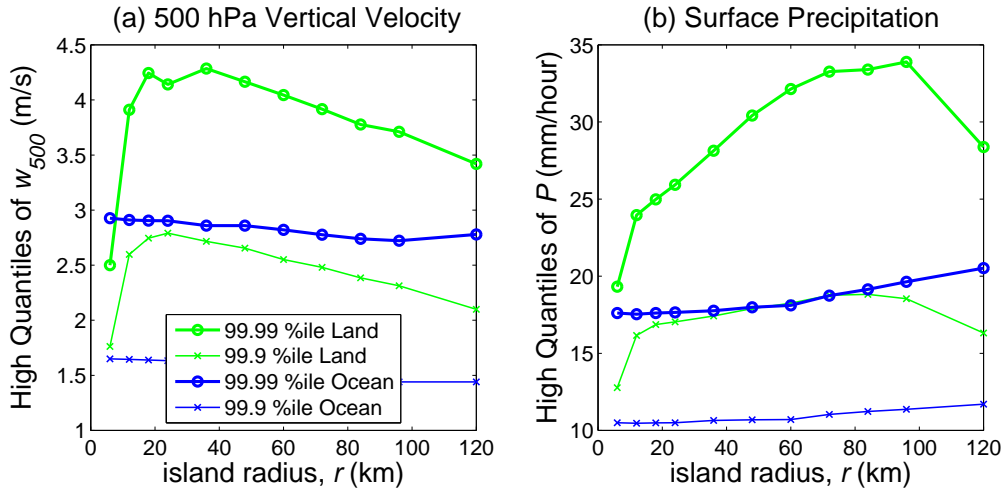
Figure 5-4: Plot of two measures of convective intensity: (a) extremes of w_{500}, m/s; (b) surface precipitation rate, mm/hour. The 99.99% (open circles) and 99.9% (x symbols) quantiles over both island (green) and ocean (blue) are plotted; convection over the island is considerably more intense by both vertical velocity and precipitation rate metrics, but the two do not show the same scaling with island size.

sizable, on the order of 2-3 hours; this is likely somewhat large compared to the real world, and the controls on this phase lag will be discussed further in Section 5.7. The major lag that depends on island size is the lag between surface enthalpy fluxes and precipitation. For the smallest islands, the rainfall maximum is in the early afternoon, nearly in phase with peak surface enthalpy fluxes; for the largest islands, the rainfall maximum occurs near sunset, lagging the peak in enthalpy fluxes by nearly four hours. The phase lag of precipitation relative to surface enthalpy fluxes increases rapidly with island radius for small islands, then saturates as island size increases further. We will also discuss this phase lag, between the surface enthalpy flux forcing, and the rainfall response, in Section 5.7. Finally, the phase lag between rainfall and cloud fraction is on the order of an hour, and increases modestly with increasing island size. This time scale is consistent with a convective life cycle of air-mass showers where heavy rainfall comes from strong updrafts that take on the order of an hour to reach the tropopause and detrain into high anvil clouds (*Emanuel*, 1994).
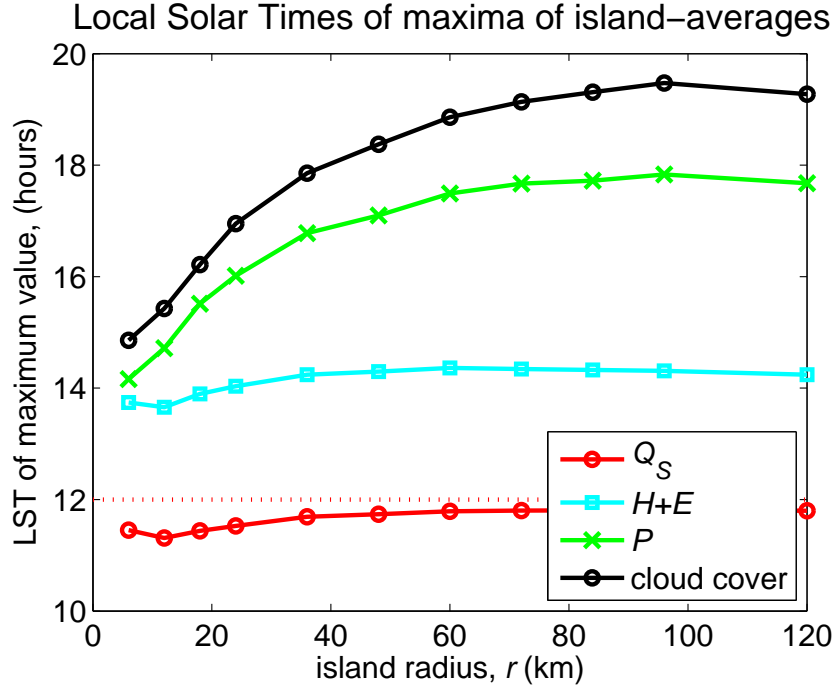
118

Figure 5-5: Plot of island radius against the phase of the maxima of island-averaged surface solar radiation (red), surface enthalpy fluxes (cyan), precipitation (green), and cloud fraction (black), for a set of simulations with SAM. The phase of the maxima of all four variables is calculated from the 1/day fourier component of each variable, averaged over all island grid cells.

5.4 Mean Rainfall Enhancement

To better understand why island rainfall enhancement occurs, we can decompose precipitation enhancement into local and remote water vapor sources. The local contribution to island rainfall enhancement is that the island evaporation rate can exceed the ocean evaporation rate; simulations suggest this effect has a magnitude of ∼0.5 mm/day (Figure 5-3). The remote contribution is stronger (∼1-4 mm/day from Figure 5-3), and related to the convergence of water vapor in the atmosphere over the island. We will discuss both the evaporation enhancement and the moisture convergence effects in this section, though we still cannot explain many aspects related to the strength of the moisture convergence mechanism and its scaling with island size.

The enhancement of evaporation over the island, and its scaling with radius, are governed by two separate mechanisms. The timing of clouds as a function of is-

land size, and the consequent varying impact of cloud shading on the surface energy budget, largely determines the scaling of evaporation enhancement with island size. As island radius increases, the cloud fraction peak shifts from mid-afternoon to after sunset, and the surface cloud radiative effect (CRE) contrast between island and ocean shifts from negative to positive. The evaporation contrast between island and ocean follows this scaling, but is shifted upwards by $\sim$10 W/m^2 (Figure 5-6). The explanation for this systematic offset, whereby the island evaporates more than the ocean even when cloud radiative effects on surface energy balance over island and ocean are equal, relates to the impact of surface variability on the time-mean surface temperature and partitioning of surface energy balance. By approximating the total turbulent enthalpy flux and longwave cooling from the surface with quadratic polynomials in the surface-air thermal disequilibrium, and assuming that they both have upward curvature, it can be shown that larger variance of surface temperatures implies a shift in partitioning of surface energy balance towards the flux that is more nonlinear (see Appendix 5.9). Because the turbulent exchange coefficient depends on the near-surface stability, and because the Clausius-Clapeyron equation is more nonlinear than the Stefan-Boltzmann equation, increasing the variance of surface temperatures thus tends to shift the surface energy budget away from radiative cooling and towards evaporative and sensible cooling. This mechanism also leads to a smaller, or negative, difference between time-mean surface temperature and time-mean surface air temperature. The time-mean surface air temperature over the island is also reduced due to diurnal variability, but this can be more simply explained as a result of averaging over a highly stable nocturnal boundary layer and a nearly neutral daytime boundary layer, rather than requiring invocation of surface energy balance. The combination of these two mechanisms – surface energy balance nonlinearity, and time-mean boundary layer stability – explains our finding that the island has a cooler time-mean surface temperature than the ocean in all simulations, by an amount that varies from 3.4 to 5.5 K across the range of island sizes. The surprising result that the land surface can be cooler due to the diurnal cycle was previously discussed by *Randall et al.* (1991), who noted that the global-mean surface temperatures over land
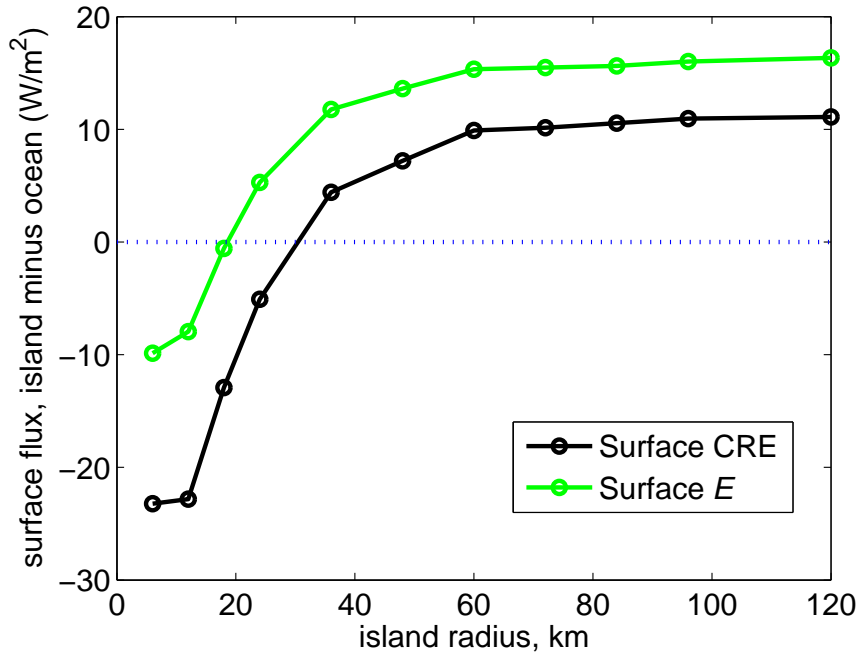
Figure 5-6: Plot of island minus ocean contrasts in surface cloud radiative effect (CRE, black) and evaporation (E, green), as a function of island radius. The contrast between island and ocean evaporation rates follows with the island-ocean CRE contrast, but is further increased by nonlinearities in the surface energy budget (see Appendix 5.9).

in a GCM simulation with a diurnal cycle of insolation were 2.7 K cooler than in a simulation with diurnal-average solar insolation.

Atmospheric moisture convergence dominates both the time-mean precipitation enhancement, and its scaling with radius. It is not obvious why there should be mean ascent and moisture convergence over the island, rather than mean subsidence and moisture divergence, and here we explore physical mechanisms that can "rectify" an oscillatory forcing into a time-mean circulation, with moisture convergence and ascent. Such mechanisms can be primarily thermodynamic or dynamic, though both thermodynamic and dynamic budget equations must hold in either case. An appealing thermodynamic explanation for time-mean ascent over the island would be a surplus in the domain-average top-of-atmosphere (TOA) net radiation over the island. Theories of Gross Moist Stability could then be used to relate the energy surplus of the island atmospheric column to the time-mean moisture convergence (*Neelin and*

Held, 1987; *Zeng and Neelin*, 1999; *Raymond et al.*, 2009). It does not appear, however, that the time-mean moisture convergence or circulation strength scale with the TOA radiative imbalance across the range of island sizes; Figure 5-7 shows that the TOA net radiation over the island is largest for the larger islands, where time-mean moisture convergence falls off, and that TOA net radiation is negative for some of the smallest islands, where time-mean moisture convergence is large. A TOA radiative surplus is thus neither a necessary nor a sufficient condition for time-mean moisture convergence, though it may still be an important contributor to the time-mean moisture convergence that is being masked by another more important mechanism. Gross Moist Stability thus proves to be a slippery concept for the system we are studying here, because the island-average proportionality factor between moisture convergence and moist static energy divergence is not constant in magnitude or sign with time, and even defining the Gross Moist Stability for circulations that vary on time scales that are comparable to lifetimes of convective clouds may be an ill-posed problem. This failure of simple thermodynamic arguments suggests that dynamical mechanisms are critical to explaining why there is time-mean ascent over the island, especially in some simulations where there is actually a TOA radiative deficit.

One dynamical mechanism that could plausibly rectify the diurnal cycle is related to the nonlinear dependence of convection on stability, and can be distilled into a dry fluid dynamical problem. Consider an infinite half-plane of nonrotating, unstratified fluid, bounded by on the bottom by a rigid wall, with a point on the bottom wall that oscillates in time between buoyancy source and sink, but which has no time-mean buoyancy input to the system. The point heat source will generate a buoyant plume when it is heating that will penetrate upward indefinitely, but the plume will not reverse when heating switches to cooling; rather, a cold pool will form and spread out across the lower boundary. We may thus expect that although there is no net buoyancy input, there will be a time-mean circulation, which will have deep ascent from the warm convective plume, as well as shallow subsidence from the spreading cold pool. Furthermore, if surface friction acts to limit the strength of the shallow cell enough, there could be time-mean ascent at all heights above the point source of
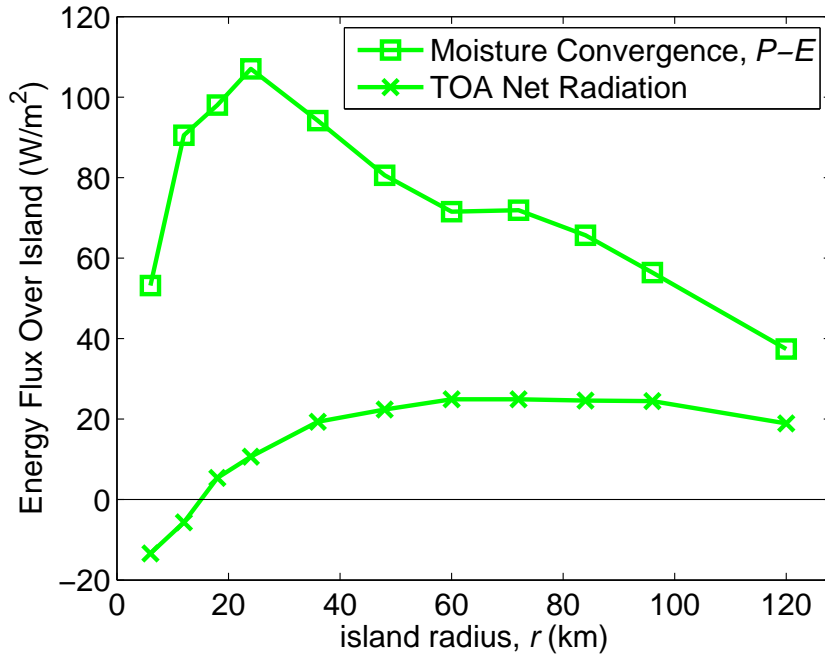
Figure 5-7: Plot of island radius against the island-averaged atmospheric latent heat convergence (open squares), and island-averaged top-of-atmosphere (TOA) net radiation (x symbols), for a set of simulations with SAM. There is no correlation between TOA net radiation and moisture convergence, across the set of island sizes.

buoyancy.

We can test this convective rectification mechanism in a slightly less idealized setting by using SAM as a dry atmospheric dynamical model. We simulate a 2-dimensional atmosphere, with 1 km horizontal resolution and domain length of 1000 km, and 64 vertical levels in a stretched grid. The initial sounding has a troposphere that is neutral to dry convection, with θ=300 K, patched to a T=200 K isothermal stratosphere (the tropopause is just above 10 km); temperatures are relaxed back to these values everywhere with a 5-day relaxation time scale. There is no atmospheric water vapor, clouds, or radiation. We apply a sensible heat flux at the lower boundary that is sinusoidal in time, with amplitude 0.05 K m/s, period of one day, and zero mean heat input. This oscillatory sensible heat flux is spatially localized to an island in the central 100 km of the domain, with no surface buoyancy flux elsewhere. In terms of anomalous surface buoyancy flux from the spatial mean, this spatially localized, oscillating forcing is very similar to results from the more realistic diurnal cycle in full-
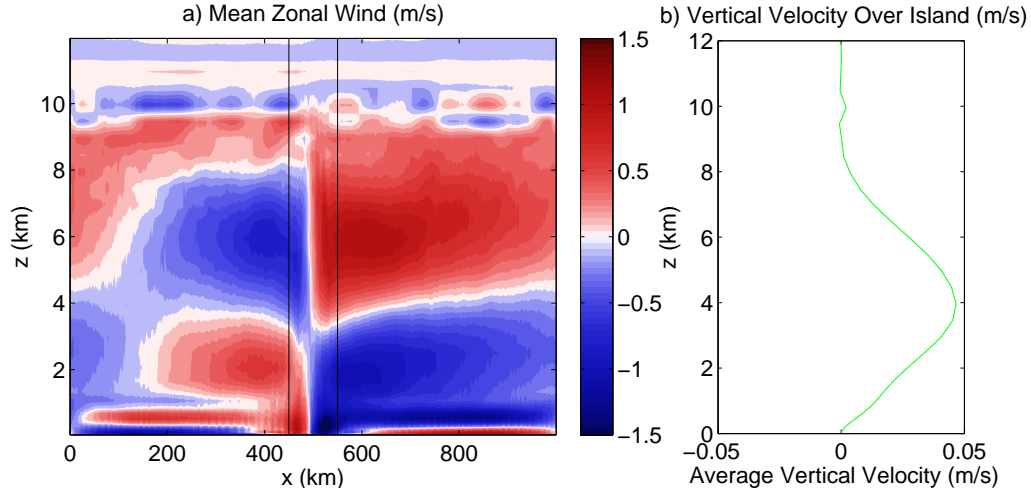
Figure 5-8: Plot of mean circulation in 2D dry simulation with SAM; subplots show a) mean zonal wind and b) mean vertical velocity from x=450 to x=550 km. As described in the text, a zero-mean sinusoidal buoyancy forcing is applied to the lowest model level, for the region indicated by vertical black lines in a).

physics SAM simulations, but rather than acting as a forcing in a totally quiescent background state, islands in full-physics SAM act as a perturbation to statistical radiative-convective equilibrium. In our dry simulation, a circulation indeed develops, with mean ascent at all heights over the island, with a maximum island-averaged vertical velocity of ∼4.5 cm/s at a height of 4 km above the surface (Figure 5-8). There is a shallow circulation as well, but the near-surface divergence and subsidence associated with it occur slightly outside the edges of the island, rather than over the island itself.

It is a leap to suppose that this is exactly the mechanism operating in our full-physics island simulations with SAM, where moisture introduces many additional complexities, including asymmetries between upward and downward motion, gravity wave dynamics, and the potential for multi-cell circulations with evaporation-driven downdrafts and descent. Furthermore, determining the scaling of the deep circulation with island size and buoyancy forcing amplitude in dry simulations would require much more work than the one case we have shown here. Despite these caveats, the basic rectifying mechanism of convection-stability interaction remains appealing, though it must still be reconciled with the thermodynamic balance of the time-mean

124

circulation. Particularly vexing is the question of how there can be deep time-mean ascent over the island in some simulations where the island atmospheric column is losing energy compared to surrounding columns over the ocean. The answer to this may be simply that the time-mean circulation has many degrees of freedom, and passes through stages during each day where the sign of the Gross Moist Stability reverses; only a small shift in circulation timing or vertical extent is required to substantially change the time-mean column energetic balance, including the ability to import moist static energy when there is time-mean ascent.

The dry convective rectification mechanism is also appealing because it predicts a perturbation atmospheric thermal structure that is similar to that observed in full-physics simulations with SAM (Figure 5-9). In particular, the atmosphere is colder at low levels, warmer through most of the depth of the troposphere, and then colder again in the lower stratosphere, compared to the initial sounding. These changes in lapse rate and vertical thermal structure provide a slightly different viewpoint for explaining why there is time-mean ascent over the island, and suggests the importance of islands for large-scale dynamics.

5.5   Changes in Mean Temperature

Simulations with an island typically have a warmer troposphere and a slightly cooler surface than control simulations with an all-ocean surface. Denoting the island area fraction A_I, we can look at the mass-weighted temperature perturbation from a control (all-ocean) simulation as a function of island area fraction (Figure 5-10). For smaller islands, an increase in A_I of 0.1 corresponds to a mass-weighted atmospheric temperature increase of about 0.8 K. This warming saturates, though, for the largest island, which occupies nearly a third of the total domain area. While the atmospheric column warms with the inclusion of an island, the surface temperature stays nearly the same, increasing slightly in some simulations and decreasing in others. A composite of the vertical structure of the thermal perturbation caused by including an island has slight cooling at the surface, a strong increase in boundary-layer stability,
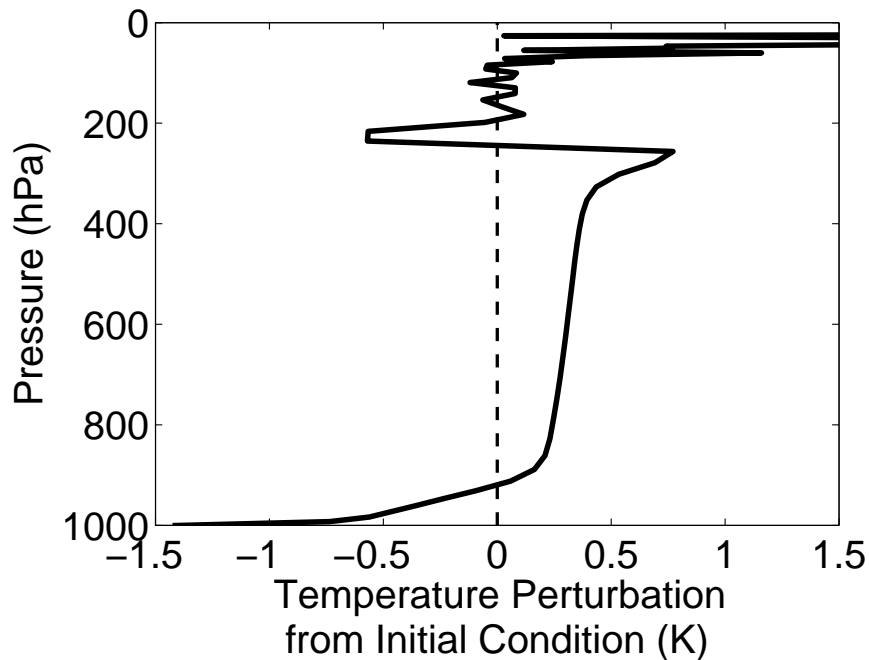
Figure 5-9: Plot of vertical structure of domain-average temperature perturbation from the initial condition in the 2D dry simulation with SAM.

a roughly moist-adiabatic temperature change in the free troposphere, and cooling in the lower stratosphere (Figure 5-11).

There are two reasons for the atmospheric warmth of these island simulations, relative to a comparable all-ocean simulation. The first is that the impact of the island on cloud fraction timing and top-of-atmosphere cloud radiative effect leads to an energetic surplus that warms both the atmosphere and the surface. This warming due to cloud timing is especially important for the larger island sizes where the clouds peak later in the day and there is a consequent strong positive cloud radiative effect and net radiative surplus over the island. But there is also a second reason, which tends to warm the atmosphere even in simulations where the cloud radiative effect over the island is zero or slightly negative. As in the above example of an oscillating heat source in a dry fluid leading to a mean circulation, the island has greater variability of surface buoyancy and enthalpy fluxes than the surrounding ocean. Furthermore, the dynamics of moist convection act to set the domain-average thermal structure of the free troposphere to a nearly convectively neutral state, with θ_e^* determined not
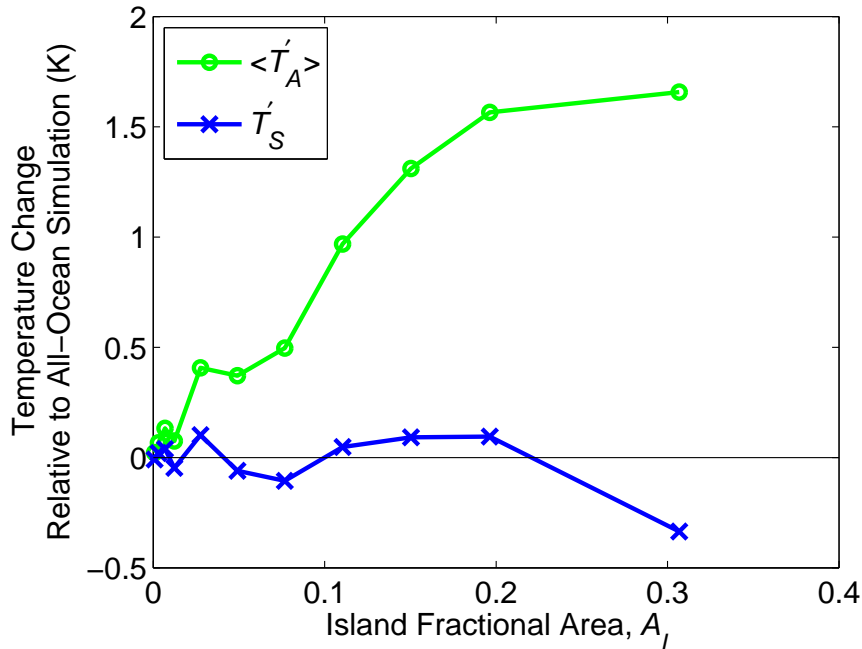
126

Figure 5-10: Plot of island area fraction A_I, against the mass-weighted atmospheric temperature perturbation ($\langle T'_A \rangle$, green), and the surface temperature perturbation (T'_S, blue). Both variables are averaged over the whole domain, and the perturbation is considered relative to comparable means from an all-ocean simulation.

by the mean, but by a high quantile, of boundary-layer moist entropy. But also as a consequence of variability, the time-mean temperatures within the boundary layer and at the surface itself, over land, tend to be lower than one would expect from the free-tropospheric moist adiabat. If the surface radiates directly to space through an atmospheric window, then greater surface variability can result in the same top-of-atmosphere longwave emission, but with less emission from a slightly cooler surface allowing for more emission from a slightly warmer atmosphere. We would expect that this mechanism would become less important with increasing temperature, as the atmospheric window closes off at temperatures much above those in the current tropics.

The mean ascent over the island can also be thought of as a consequence of the impact of the island on the thermal structure of the atmosphere. In the weak temperature gradient approximation (WTG) of tropical dynamics, anomalous heating of the free troposphere over a region must be balanced by ascent (e.g.,*Sobel et al.* (2001)). In
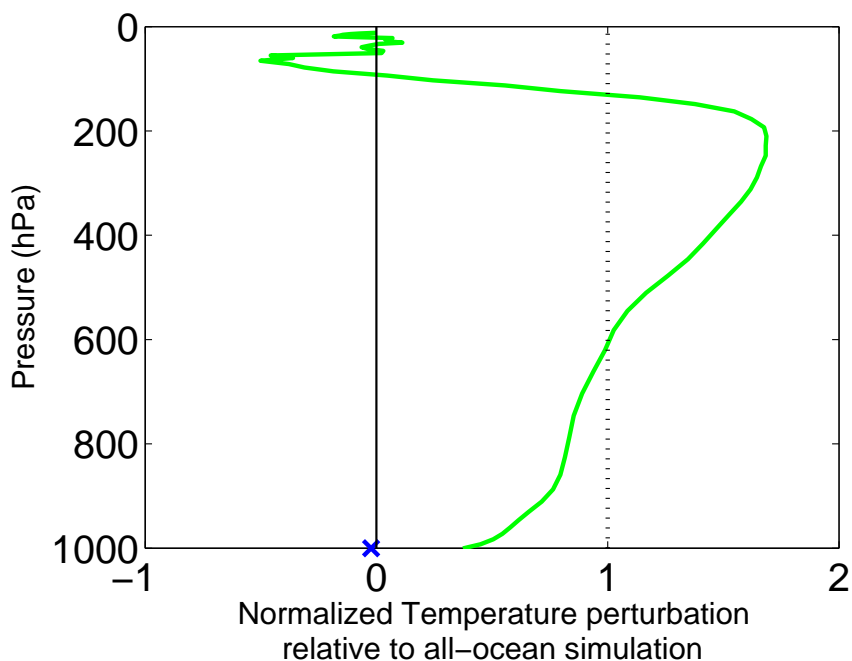
Figure 5-11: Plot of the normalized vertical structure of domain-average temperature perturbation averaged over the simulations shown in Figure 5-10. The vertical structure of warming is normalized to have a mass-weighted atmospheric mean of 1 K in this plot, and the average surface temperature change is shown as a blue x.

attempting to relax upper tropospheric temperatures to a warmer time-mean state, the radiative-convective dynamics over the island can be thought of as a heating that must be balanced by a deep ascending circulation, which converges moisture into the island column. To the extent that the domain-averaged free tropospheric temperature is warmer in simulations with an island, the WTG approximation also suggests that a larger region with islands would be a favored region for large-scale ascent, with mean subsidence over a comparable open ocean region. The strength of the large-scale circulation that would result, however, is difficult to estimate, and both cloud and ocean dynamical feedbacks could amplify or dampen such a circulation considerably. Explicitly simulating the strength of such a large-scale circulation, resulting from the presence of an island or group of islands, is a key focus of future work.

5.6   Relation to Sea Breeze Theory

One major question posed by our results relates to how the optimal island size for precipitation enhancement is determined. Work by *Robinson et al.* (2008), as well as *Rotunno* (1983), suggests the importance of an internal length scale, Nz_0/ω, for the response of a shallow linear land/sea breeze circulation to an oscillating heat source with angular frequency ω and scale height z_0. *Robinson et al.* (2008) hypothesize a "resonant response" of the linear sea breeze at a certain island size, and their results for convective intensity (see Figure 1 of *Robinson et al.* (2008)) bear a strong resemblance to our time-mean atmospheric moisture convergence (Figure 5-3). Exploration of the theory of the linear sea breeze may thus yield some useful insight about whether or not sea breeze dynamics play an important role in our results.

First, we note that previous studies by *Rotunno* (1983) and *Robinson et al.* (2008) both explored the linear sea breeze problem in Cartesian geometry, and largely examined the weakly dissipative limit. This leaves open questions of the validity of linear theory for fully nonlinear dynamical models (such as SAM), the effects of cylindrical versus Cartesian geometry, and the relevance of the weakly damped limit in a turbulent, dissipative boundary layer.

Previous work by *Robinson et al.* (2008) and *Robinson et al.* (2011) suggested that the internal linear-theory length scale may be useful for understanding the increase in convective intensity over islands as their size increases, but *Robinson et al.* (2013) note that the utility of linear theory is somewhat of a puzzle; one might expect real-world sea breezes to behave as nonlinear density currents. *Crook* (2001) also suggests that under weak mean-flow conditions, solving for island-averaged low-level convergence in a weakly stratified boundary layer must account for nonlinear dynamics. We can directly address the basic question of whether the simulated momentum budgets are dominated by linear or nonlinear terms, which ought to serve as the basis for more thorough investigation of one of the two limits. We start by writing the radial momentum equation,

$$\frac{\partial u_r}{\partial t} + u_r \frac{\partial u_r}{\partial r} = -\frac{1}{\rho}\frac{\partial p}{\partial r} - \mathcal{F}_r, \qquad (5.2)$$

where u_r is the radial wind, the left hand size contains linear $(\partial u_r/\partial t)$ and nonlinear $(u_r \partial u_r/\partial r)$ accelerations, and the right-hand side contains the pressure gradient acceleration, as well as a damping term $(\mathcal{F}_r)$. Assuming that the pressure gradient acceleration can be thought of as a buoyancy-driven forcing, we can diagnose the linearity of the sea breeze by seeing how much of the spatial structure in a composite of the pressure gradient forcing associated with the sea breeze is explained by linear and nonlinear terms in the surface wind momentum balance:

$$-\frac{1}{\rho}\frac{\partial p}{\partial r} = \overbrace{\frac{\partial u_r}{\partial t} + \alpha u_r}^{\text{Linear Terms}} + \overbrace{u_r\frac{\partial u_r}{\partial r} + \mathcal{F}_{r,\text{nonlin}}}^{\text{Nonlinear Terms}}. \tag{5.3}$$

Here, we have assumed that the surface drag can be expanded into a linear Rayleigh damping component with rate α, and a nonlinear residual component. For the purpose of understanding the validity of linear theory, we need to quantify the relative magnitudes of the linear and nonlinear terms in (5.3). We perform this analysis by computing radial and diurnal composites of terms in Equation (5.3); the linear portion of the damping is assumed to have $\alpha = 3.6 \times 10^{-5}$ s^{-1}, which is based on the surface drag coefficient and thickness of the lowest model level. We diagnose the nonlinear term as a residual of the pressure gradient acceleration that is unexplained by the linear terms (Figure 5-12). For the reference-case island simulation, the majority of the variance in the pressure gradient acceleration is borne by the linear terms. This finding holds increasingly well for larger island sizes, but the linear terms explain less than half of the spatial variance in the pressure gradient acceleration pattern for smaller island sizes. The momentum budget in our simulations thus suggests that we may be able to learn something by analyzing the linear sea breeze; though the nonlinear terms in the radial momentum equation are far from trivial, they at least do not dominate the budget across the full range of island sizes.

The theory of the linear sea breeze has been explored by a number of authors, but none to our knowledge have formulated the version of the problem that is most relevant to us; namely the theory of the linear sea breeze with no Coriolis force, cylindrical geometry, and modest damping. This last point, regarding the relevance
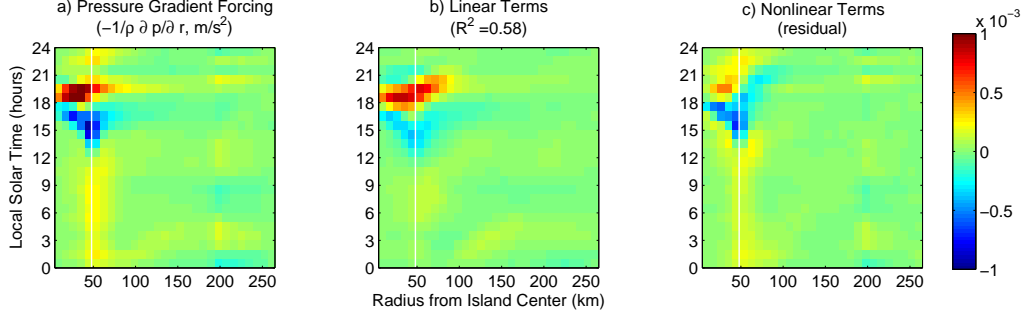
Figure 5-12: Radially and diurnally composited plot of the terms in the radial momentum budget for surface winds, in the reference-case island simulation (radius:left-to-right, local solar time: bottom-to-top). Subplots show a) Pressure gradient acceleration (m/s^2), b) linear terms in surface wind radial momentum equation ($\partial u_r/\partial t + \alpha u_r$) and c) the inferred sum of nonlinear terms in the radial momentum equation; see Equation (5.3). The majority of the variance in the pressure gradient acceleration is explained by the sum of the linear terms.

of dissipation, is touched upon by *Rotunno* (1983), who shows that the linear sea breeze circulation will peak near midnight in an inviscid model, and that significant damping is required to bring the peak circulation back into the afternoon. In a study of the diurnal cycle of temperature and pressure over North America, *Li and Smith* (2010) also show that a thermal damping coefficient on the order of $\sim 7 \times 10^{-5}$ s^{-1} is required to match the phase lag of temperature relative to local solar noon. In our simulations, as in the real world, low-level onshore flow peaks in the early to mid afternoon, indicating that damping is likely quite important to the simulated phase of the sea breeze circulation.

By using the Boussinesq equations, with a buoyancy forcing function B that oscillates in time with angular frequency ω, and assuming Rayleigh damping of both momentum and buoyancy with rate α, we can derive an equation for the overturning streamfunction ψ of the linear sea breeze (see Appendix 5.10 for full derivation):

$$\left(N^2 - \omega^2 + i\omega\alpha\right)\left(\frac{\partial^2 \psi}{\partial r^2} + \frac{1}{r}\frac{\partial \psi}{\partial r} - \frac{\psi}{r^2}\right) \;+$$
$$\left(\alpha^2 - \omega^2 + 2i\omega\alpha\right)\frac{\partial^2 \psi}{\partial z^2} \;=\; -\frac{\partial B}{\partial r}. \tag{5.4}$$

The buoyancy forcing function B has been formulated slightly differently by the studies of *Rotunno* (1983), *Robinson et al.* (2008), and *Robinson et al.* (2011). One basic insight provided by (5.4) is that it is the horizontal gradient of the buoyancy forcing, and not the buoyancy forcing itself, which acts as the forcing function for the overturning streamfunction. The same amount of spatially integrated buoyancy forcing may thus have a different response, and different scaling with island size, if the spatial structure function is an arctangent (*Rotunno*, 1983), a Gaussian (*Robinson et al.*, 2008), or a square wave/"top hat" (*Robinson et al.*, 2011). For illustrative purposes, we will show results for solutions with both an arctangent forcing and a Gaussian forcing, respectively as in *Rotunno* (1983) and *Robinson et al.* (2008), but with x replaced by r:

$$B(r,z)_{\text{arctan}} = B_0 e^{-z/z_0}\left(\frac{1}{2} - \frac{1}{\pi}\arctan\left(\frac{r-r_I}{a_0}\right)\right)e^{i\omega t} \qquad (5.5)$$

$$B(r,z)_{\text{Gaussian}} = B_0 e^{-z/z_0} e^{-r^2/r_I^2} e^{i\omega t}. \qquad (5.6)$$

We obtain solutions to (5.4) by writing the left hand side in discrete form, as the product of a matrix linear operator $\mathcal{L}$ acting on an array of values of ψ. Inverting $\mathcal{L}$ with MATLAB and multiplying by the buoyancy forcing array then yields the streamfunction:

$$\psi = -\mathcal{L}^{-1}\left(\frac{\partial B}{\partial r}\right); \qquad (5.7)$$

the real part of the product $\psi e^{i\omega t}$ is the oscillating solution that we seek. For reference conditions of N=0.01 s^{-1}, ω=2π day^{-1}, z_0=250 m, a_0=1000 m, and a buoyancy forcing amplitude corresponding to a sensible heat flux amplitude of H_0=50 W m^{-2} ($B_0 = gH_0/(\rho_0 c_p T_0 z_0)$), we plot the maximum onshore wind speed, and its phase lag from the maximum buoyancy forcing, as a function of island radius, for several different assumptions about the damping rate, forcing function, and geometry (Figure 5-13). The difference between Cartesian and cylindrical geometry leads to minimal difference in sea breeze strength or timing, but the geometric effect of focused flow does mean that the average convergence of the surface wind is approximately twice as large in the case of cylindrical symmetry. Because the radial gradient of buoyancy
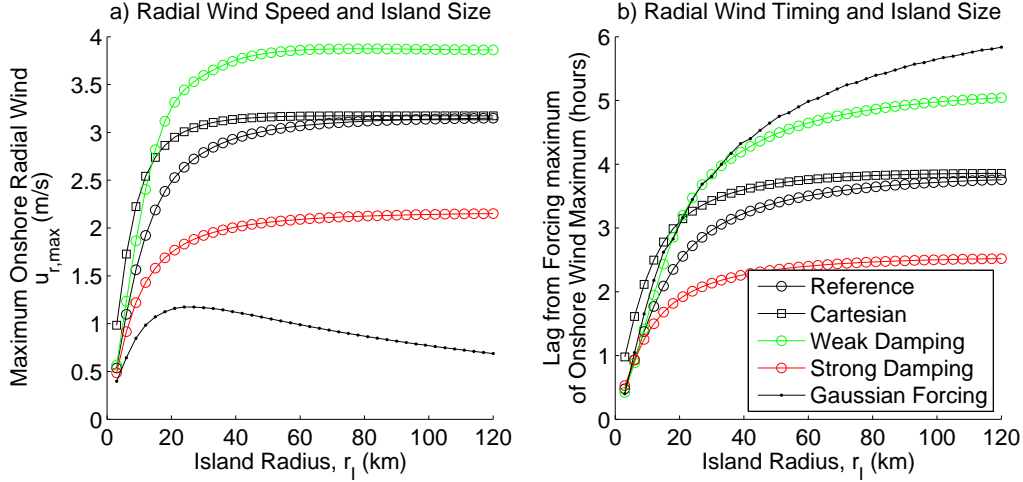
132

Figure 5-13: Plots of a) maximum onshore wind speed (m/s) and b) lag between peak buoyancy forcing and maximum onshore wind, against island radius, from numerical solutions to the linear sea breeze equations (5.4). The "Reference" case uses polar coordinates, and $\alpha=5\times10^{-5}$ s^{-1}, the "Cartesian" case only modifies geometry. "Low Damping" and "High Damping" solutions use $\alpha=2\times10^{-5}$ s^{-1} and $\alpha=1\times10^{-4}$ s^{-1}, respectively. The "Gaussian" case uses a Gaussian buoyancy forcing, as in Equation (5.6); the other four cases all use an arctangent forcing (5.5).

forcing is directly tied to the island size in the case of a Gaussian forcing, but has an independent scale (a_0) in the case of an arctangent forcing, the use of a Gaussian forcing leads to weaker maximum radial wind speeds, and a fall-off of wind speed at larger island radii; the arctangent forcing (used in the other four curves) has a generally stronger radial wind that plateaus for larger island sizes.

The impact of the heating function on the sea breeze strength, and particularly its response to changing island size, may explain the contrast in the findings of *Robinson et al.* (2008) and *Robinson et al.* (2011). While *Robinson et al.* (2008) find a clear maximum in metrics of convective intensity for an island half-width of ∼20 km, *Robinson et al.* (2011) find little decrease in convective intensity at even much larger islands, either in model simulations or satellite observations of the real world. If the strength of the sea breeze is connected to the intensity of subsequent convection, then this difference could be a function solely of the sharpness of the gradient of sensible heat flux at the island edge: real islands (as well as the simulated islands in *Robinson et al.* (2011)) have a sharp (arctangent-like) gradient of sensible heat flux at their

133

edges, rather than a smooth, Gaussian decay (as in *Robinson et al.* (2008)).

As noted above, the resonance in *Robinson et al.* (2008) provides a tempting hypothesis for why we find a maximum in moisture convergence for islands of radius $\sim$20 km. But upon closer inspection, their theory relates to the component of surface pressure that is in phase with the heating, and does not incorporate the surface pressure perturbation that is in quadrature with the heating. This component of the pressure perturbation has been referred to as the "thermal continental tide" by *Li and Smith* (2010), and saturates in the large-island limit (see Appendix 5.11), rather than decaying to zero. *Robinson et al.* (2008) also focus on the strength of the heat low at the center of an island as a measure of convective intensity; however, in the linear limit, it is far from clear that the island-center pressure perturbation is the best metric for convective intensity. Island-averaged convergence, for instance, might be thought of as a dynamical forcing for convection, and likely scales with $\delta p/r_I^2$, rather than with δp itself. Along these lines, if we estimate the maximum in island-average convergence as $2u_r/r_I$ from the "Reference" curve in Figure 5-13, we obtain a $\sim r_I^{-1}$ decay at large island sizes, and a maximum at $r_I = 0$; this matches the large-island fall-off of *Robinson et al.* (2008), but for different reasons, and without an intermediate maximum. We also cannot rule out the possibility that part of the fall-off with island size is limited by the size of the domain; simulations with a smaller domain had a moisture convergence peak at a slightly smaller island radius. Taken together with the questionable utility of the inviscid limit and the unrealistic spatial smoothness of the heating function in *Robinson et al.* (2008), these findings suggest that the resemblance between Figure 1 of *Robinson et al.* (2008) and our dependence of mean moisture convergence on island size in Figure 5-3 is likely nothing more than coincidence.

Linear sea breeze theory may still be useful, though, for explaining numerous aspects of our simulations. Though it may not determine a resonant scale for mean rainfall enhancement, it closely predicts maximum onshore wind speeds. In the next section, we also examine whether sea breeze theory can explain the phase lag of precipitation relative to surface enthalpy fluxes, and the scaling of this lag with island

size.

5.7 Phase Lags of Surface Fluxes and Rainfall

It is encouraging that our simulations with SAM often obtain an island precipitation maximum that is lagged by several hours relative to local solar noon, as observed over warm-season and tropical land in the real world, as well as moderate-size islands (e.g., *Liu and Zipser* (2008), *Hamilton* (1981), *Keenan et al* (2000)). Convective parameterizations often produce a peak of convective precipitation that occurs in the late morning, or around noon, in sharp contrast to observations (*Guichard et al.*, 2004; *Dirmeyer et al.*, 2012). It seems likely that resolving the mesoscale dynamics associated with the sea breeze, and resolving the cloud systems themselves, has allowed us to obtain a few-hour lag between local solar noon and peak rainfall. But there are numerous possibilities for what sets this lag, and why in our simulations it is sensitive to island size. Also, our results regarding the lag of the diurnal precipitation peak relative to local solar noon have at least two important caveats regarding comparison to the real world.

The first caveat is that the horizontal resolution in our simulations, at 3 km, is still far too coarse to realistically resolve convection (especially in the boundary layer); we can only really hope to capture convective systems. We must allow for the possibility that coarse resolution makes convection more sluggish in its response to surface heating than it would be in the real world. To address this concern, we have conducted three simulations with island radii of 12, 24, and 48 km, with doubled horizontal resolution of 1.5 km (four times as many grid points). Fortunately, increasing resolution generally has little influence on the timing of precipitation, or its phase lag from the surface enthalpy flux, and leads to a slightly longer lag, rather than a shorter one. For simulations with r_I=48 km, 3-km resolution yields an island rainfall peak at 17:06 LST, while 1.5-km resolution yields a later island rainfall peak at 17:40 LST. Resolution-sensitivity is even smaller for smaller islands; timings of peak surface shortwave radiation, surface enthalpy fluxes, precipitation, and cloud fraction

for r_I 12 and 24 km change by no more than 10 minutes due to doubling resolution. This sensitivity test is far from definitive, but suggests that the mechanisms resulting in important phase lags are at least relatively stable to increasing model resolution.

The second caveat is that it is important to consider the lag of circulation and precipitation relative to the forcing by surface sensible and latent heat fluxes, not just relative to the solar heating. As noted above with regards to Figure 5-5, the surface enthalpy fluxes themselves are lagged from local solar noon, by as much as 2-3 hours. This lag is likely too long; the common understanding seems to be that surface enthalpy fluxes peak within an hour of solar noon (e.g., *Deardorff* (1978), *Smith et al.* (1992), *Beringer and Tapper* (2002), *Betts* (2004)), though some studies have suggested that the lag could be as large as 2-3 hours (*Brubaker and Entekhabi*, 1995). It is difficult to find a decisive answer to the question of exactly how long the lag between solar forcing and enthalpy fluxes should be. Preliminary examination of gap-filled data from several eddy covariance stations from the AmeriFlux network (data available at `http://cdiac.ornl.gov/ftp/ameriflux/data/`) suggests that for a range of real land surfaces, the surface enthalpy fluxes lag solar forcing by only ∼10 minutes, a much shorter lag than the 2-3 hours we have simulated. This finding suggests that it is important to at least understand what sets this lag, and try to conduct simulations with an enthalpy flux peak closer to noon, if possible.

A linear model suggests that the relatively long lag of enthalpy fluxes relative to solar forcing in our simulations is due to the combination of relatively weak surface winds, low surface roughness, and the use of a slab model with relatively large heat capacity, rather than a thermally diffusive, multi-layer surface (*Deardorff*, 1978). The lag between peak shortwave radiation at the surface and peak surface turbulent enthalpy fluxes relates directly to the lag of temperature anomaly of a slab surface in response to an oscillating external forcing:

$$C_S \frac{\partial T_S'}{\partial t} = Q_{S0}\cos(\omega t) - \lambda T_S', \qquad (5.8)$$

where Q_{S0} is the oscillating forcing, and λ is a linearization coefficient of the total

longwave radiative plus turbulent enthalpy flux loss from the surface, with units of $W/m^2/K$. In response to the oscillatory forcing, the surface enthalpy flux will oscillate, as $\lambda T_S' \sim \cos[\omega(t - \tau_S)]$, with a phase lag, τ_S, given by:

$$\tau_S = \frac{1}{\omega} \arctan\left(\frac{\omega C_S}{\lambda}\right). \tag{5.9}$$

The flux linearization coefficient, λ, is given by the change in total energy flux out of the surface per unit change in surface temperature, and we have assumed that the temperature of the lowest model level varies much less than the surface temperature itself. Using bulk formulae to express the turbulent enthalpy flux, and assuming the surface emits as a blackbody,

$$\lambda \approx \rho c_K |\mathbf{v}|(c_p + L_v \partial q^* / \partial T) + 4\sigma_B T^3, \tag{5.10}$$

which varies depending on wind speed, drag coefficient, and absolute temperature. The weak surface winds and low surface roughness in our simulations mean that λ is relatively small. Using the linear coefficient of 14.1 $W/m^2/K$ in the fit from Figure 5-16 to give an estimate of $\rho c_K |\mathbf{v}|(c_p + L_v \partial q^* / \partial T)$, then inclusion of the Stefan-Boltzmann linearization would give $\lambda \sim 20 W/m^2/K$. With a surface heat capacity $C_{SL} = 0.05$ m.w.e., this results in an estimated surface enthalpy flux lag of 8970 s, or about 2 hours and 29 minutes. In the set of SAM simulations, the average lag of the turbulent surface enthalpy flux, relative to surface solar radiation, is 8900 s, with a standard deviation of 300 s when considering the range of 11 island sizes. This matches the simple estimate of the linear model nearly exactly, even though Figure 5-16 shows that surface turbulent enthalpy fluxes are far from linear in their dependence on surface temperature.

The phase lag in observations that is perhaps as small as $\sim$600 s likely reflects both the elevated roughness of real land surfaces, and the important role that leaf surfaces play as a functional interface between the atmosphere and surface. Increased surface roughness acts to increase λ, and the dominance of leaf surfaces in the absorption of solar radiation in many vegetation types acts to decrease the effective

value of C_S considerably below the value that would be representative of a diffusive soil surface. Taking both of these factors into account, *Nobel* (2008) estimates the thermal relaxation time scale of a leaf as a mere 18 s.

Thus, to test the robustness of some of our results to a more realistic phasing of peak enthalpy fluxes, we have performed a set of simulations with a much lower surface heat capacity of 0.005 m.w.e. In these simulations, the lag between surface solar radiation and turbulent enthalpy fluxes averages about 25 minutes, but the lag between peak enthalpy fluxes and precipitation is still on the order of 3 hours, and still increases with island size (Figure 5-14). The linearized surface heat flux theory of Equation (5.9) predicts a lag of 17 minutes, similar to but slightly shorter than the lag in simulation results. These very low heat capacity simulations also share many of the same features of mean rainfall enhancement of the primary results described above, but the time-mean moisture convergence is weaker, on the order of 1-2 mm/day (as opposed to 2-4 mm/day), likely because the TOA radiative surplus over the island is reduced (<0 for all island sizes) as a consequence of a systematically earlier cloud fraction peak. This gives further confidence that the time-mean moisture convergence cannot be easily explained by a thermodynamic mechanism.

As mentioned above, the major phase lag that depends on island size is the lag between peak surface enthalpy flux and peak rainfall and mid-tropospheric ascent (See Figure 5-5). There are a number of possibilities that could explain this lag; our results suggest that a successful mechanism must explain not only why it is on the order of 3-4 hours for large islands, but also why it decreases to nearly zero for small islands. A time scale for sea breeze fronts to collide at the center of the island would be given by r/u_r, but since u_r plateaus with island size, this timescale falsely predicts a continued increase for large islands. Another mechanism is provided by linear sea breeze theory, which indicates that it takes on the order of 3-4 hours for the near-surface convergence to respond to the surface heating for large islands, and this time scale decays to nearly zero for small islands (Figure 5-13). This mechanism requires some additional explanation, because the 3-4 hour lag in Figure 5-13 refers to convergence of surface winds, and we would expect a further lag between surface
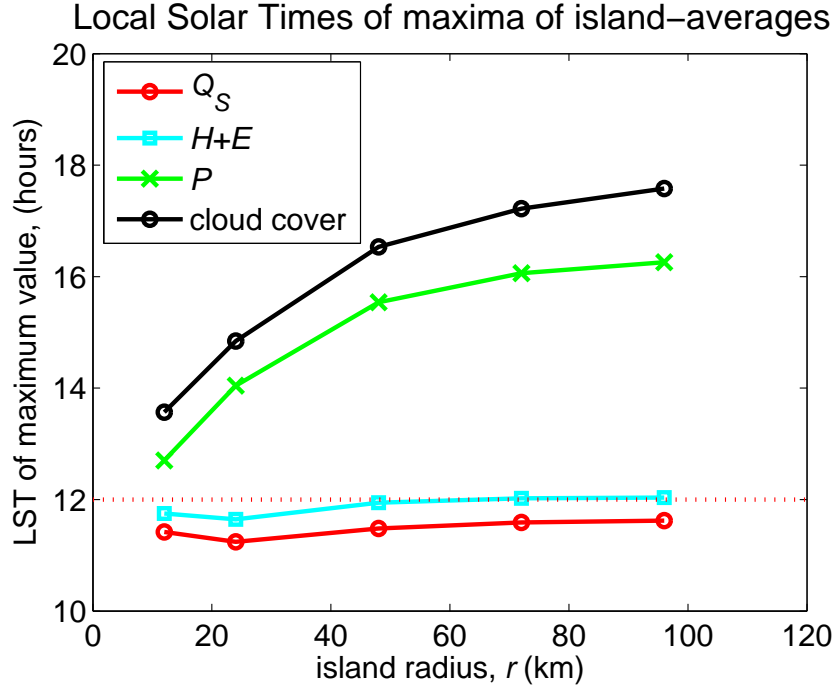
Figure 5-14: As in Figure 5-5; plot of island radius against the phase of the maxima of island-averaged surface solar radiation (red), surface enthalpy fluxes (cyan), precipitation (green), and cloud fraction (black), for a set of simulations with SAM with a reduced island surface heat capacity.

convergence and convection and mid-tropospheric ascent. Here, an apparent bias of the linear sea breeze theory may actually be its redeeming feature: the linear theory correctly estimates that maximum radial wind speeds at the surface are $\sim$3 m/s, but estimates the surface convergence to be late by about 2-3 hours (Figure 5-15). In SAM simulations, the surface convergence actually leads the surface buoyancy flux for the smallest islands, which is likely due to the suppression of late afternoon convergence by moist processes, especially downdrafts and cold pool divergence. Linear sea breeze theory may then be able to explain the timing of maximum rainfall if we can also explain a $\sim$2 hour lag between peak surface convergence and peak rainfall. Rigorously testing this idea, however, would require simulations with much different boundary conditions than we have thus far performed; perhaps the simplest means would be to subject the system to a day that was substantially different in length.
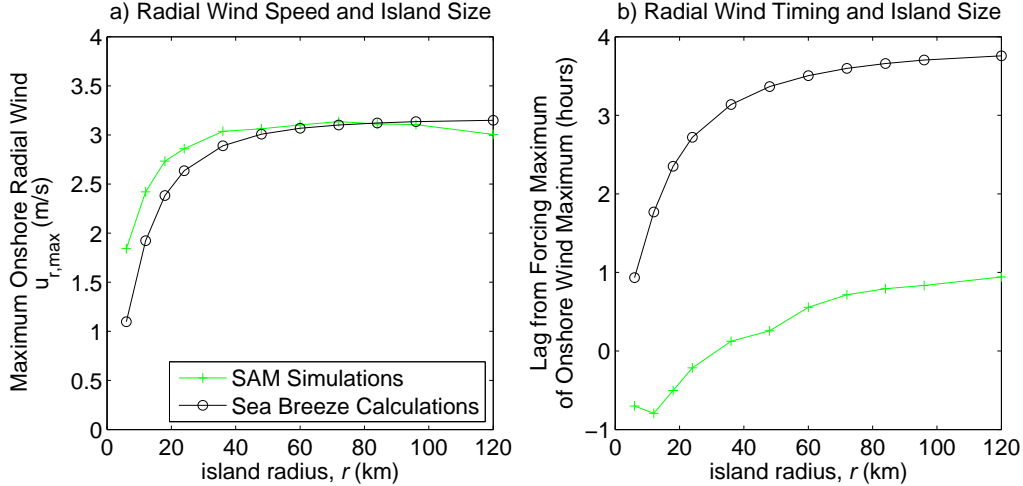
Figure 5-15: As in Figure 5-13, but including results from SAM; plots of a) maximum onshore wind speed (m/s) and b) lag between peak buoyancy forcing and maximum onshore wind, against island radius, for both SAM simulations and linear sea breeze theory. The amplitude of the surface buoyancy forcing in the linear sea breeze theory is taken to roughly match that from SAM.

5.8   Conclusions

We have presented results from simulations of radiative-convective equilibrium where a highly idealized, low heat capacity circular island is embedded in a slab-ocean domain. The island strongly affects the average distribution of rainfall, and all simulations show that the island is rainier than the surrounding ocean. Enhancement of evaporation over the island occurs due to both cloud radiative effects and nonlinearities in the surface energy budget. We suggest a dynamical mechanism that gives rise to time-mean ascent over the island, related to rectification of the dynamical response to a zero-mean oscillatory buoyancy forcing in a nonrotating, unstratified fluid. This mechanism suggests that loci where temporal surface buoyancy or enthalpy flux variability correlates with near-surface buoyancy or entropy can effectively generate available potential energy for a deep circulation with nearby ascent and remote subsidence in the time-mean.

We also find that the presence of an island typically results in an average warming of the atmospheric column. We explain this in terms of both domain-average cloud

radiative effects, and the aforementioned dynamical rectification mechanism, which tends to drive the mean thermal profile of the atmosphere towards a warmer state in the upper troposphere, and a cooler state in the boundary layer.

We study the utility of the linear sea breeze for understanding some of our results, and conclude that the framework may be useful for understanding both the strength of the sea breeze, and potentially the dependence of the timing of peak precipitation on island size. Although the atmospheric moisture convergence appears to have a resonance as a function of island size, we believe it is unlikely that the "gravity wave resonance" of *Robinson et al.* (2008) can explain it, despite a great deal of superficial similarity. We also find that the lag between peak solar forcing and peak surface enthalpy fluxes in most of our simulations is likely longer than is realistic in the real world, but its magnitude can be understood with a linear model of surface energy fluxes.

With regard to the idea that the phase lag between surface enthalpy flux forcing and maximum precipitation is set in part by an intrinsic time scale for the spin up of the surface convergence associated with a linear sea breeze, we should also note that sea breeze-like circulations are not in principle limited to coasts. Heterogeneity of soil moisture over otherwise homogeneous land, for instance, will give rise to a spatially variable amplitude of the surface buoyancy flux, which oscillates with a period of a day. A spectrum of spatial scales of boundary layer circulations would then emerge, mapping to a spectrum of time lags between peak buoyancy flux contrast and peak surface convergence. Our analysis of the linear sea breeze suggests that this mapping could give rise to a concentration of phase lags near the large-island limiting value, potentially giving rise to a several-hour phase lag between peak buoyancy forcing and peak rainfall even over an all-land surface. This hypothesis could be explored given data about the spatial variability of soil moisture and surface buoyancy fluxes over an otherwise homogeneous land region.

This paper leaves many doors open for future work. We have touched briefly on the result that convective intensity over the simulated island is far greater, by several metrics, than convective intensity over the ocean. But we have not explored in any

141

depth why extremes of precipitation scale as they do with island size. Our basic model configuration, of an isolated island in a slab-ocean domain, gives rise to a large set of external parameters, even with the background atmospheric state set internally. Preliminary investigation of the importance of island surface wetness, island heat capacity, barotropic mean flow, and removal of cold pools or cloud-radiation interactions, suggests that local enhancement of rainfall over an island due solely to the interaction of the diurnal cycle and a low-heat capacity surface is a robust result to many parametric assumptions. But sensitivity to mean temperature, island elevation, microphysics, and vertical wind shear have been left completely unexplored. The dependence of extremes of island rainfall on mean temperature is especially interesting in terms of its relevance to impacts of climate change.

Future work will attempt to clarify the scaling of atmopsheric moisture convergence with island size, by exploring the dry dynamical rectification mechanism in more detail. The suggestion that greater variability of surface fluxes over part of the domain could affect the domain-mean average temperature profile also points to several routes for attempting to understand impacts of islands on the large-scale circulation. One route is to perform simulations of RCE with a diurnal cycle of insolation over a homogeneous surface with a very broad range of heat capacities. Such simulations could help to clarify the controls on the phase lag of precipitation relative to surface enthalpy fluxes, and the extent to which coherent temporal variability in surface enthalpy fluxes generally translates to a warmer atmosphere. Another route is to perform simulations with a cloud-system resolving model where the domain has much different geometry, so as to explicitly resolve planetary-scale circulations that might result from island precipitation enhancement. One example of such geometry is in the very long 3D channel (9600 by 180 km) simulations of *Posselt et al.* (2008). We plan to conduct such simulations in the future, and hope that they will act as an idealized test of the extent to which islands of the Maritime Continent could affect the Walker Circulation.

142

5.9 Appendix A: Surface Energy Balance with Variance-Enhanced Fluxes

Here, we develop a simple mathematical model to explain why the increased variance of surface temperatures over land leads to a reduction in the time-mean surface temperature, and shifts the partitioning of surface energy balance away from longwave radiative cooling, and towards turbulent enthalpy fluxes. Consider second-order expansions of the total turbulent enthalpy flux, $F_K = H + E$, and the net surface longwave cooling, Q_L, where the control variable is the thermal disequilibrium, D, between the surface and the atmosphere at the lowest model level:

$$D = T_S - T_1 \tag{5.11}$$

$$F_K = F_{K0} + b_K D + a_K D^2 \tag{5.12}$$

$$Q_L = Q_{L0} + b_L D + a_L D^2, \tag{5.13}$$

where the a's are quadratic coefficients, the b's are linear coefficients, and the F_{K0} and Q_{L0} are the components of the fluxes that do not depend on surface thermal disequilibrium. For the reference-case island, the data are noisy, but the surface enthalpy flux is clearly quite nonlinear as a function of D (Figure 5-16), with suppression of turbulent fluxes under stable conditions ($D < 0$), and enhancement under unstable conditions ($D > 0$).

Surface energy balance amounts to a requirement that the sum of the time-mean and turbulent enthalpy fluxes equal the time-mean net shortwave heating:

$$0 = \overline{Q_S} - \overline{F_K} - \overline{Q_L}, \tag{5.14}$$

where $\overline{(\cdot)}$ denotes a time-mean. We decompose the surface thermal disequilibrium into a time-mean and a perturbation:

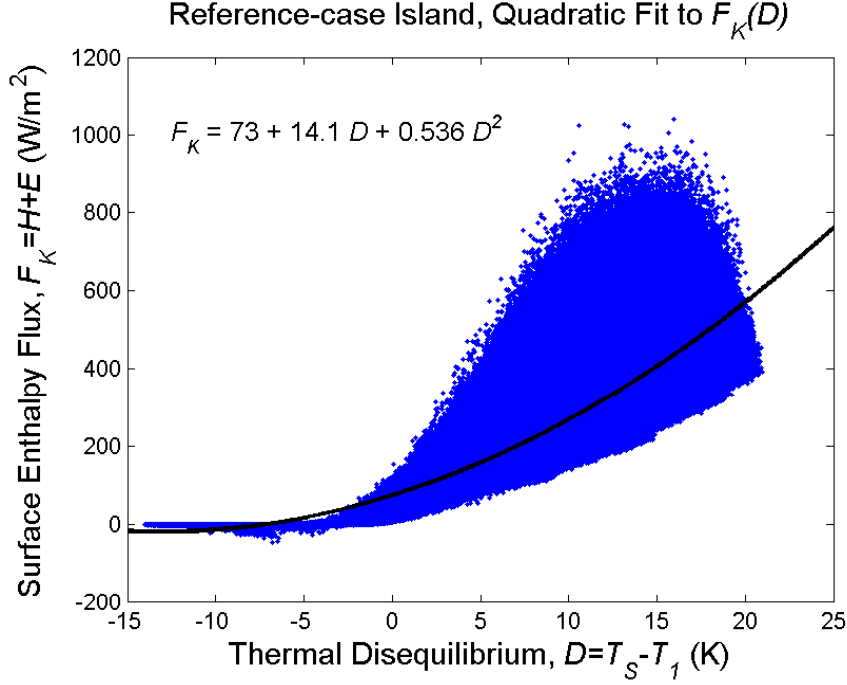$$D = \overline{D} + D', \tag{5.15}$$

Figure 5-16: Plot of a quadratic fit to the surface turbulent enthalpy flux, F_K, as a function of the thermal diesequilibrium between the surface and lowest model level temperature, $D = T_S - T_1$. The fit is shown for the reference-case island, based on 125 days of hourly-averaged data over all land grid points.

and we can then write the time-mean surface energy balance in terms of the mean and the variance of the surface thermal disequilibrium:

$$0 = (\overline{Q_S} - F_{K0} - Q_{L0}) - (b_K + b_L)\overline{D} - (a_K + a_L)\overline{D}^2 - (a_K + a_L)\text{Var}(D), \quad (5.16)$$

where $\text{Var}(D) = \overline{(D')^2}$ is the variance of the surface thermal disequilibrium. Now, we can solve for a relationship between the mean thermal disequilibrium $(\overline{D})$ and its variance $(\text{Var}(D))$:

$$\overline{D} = \frac{b_K + b_L}{2(a_K + a_L)} \left\{ \left[1 + \frac{4(a_K + a_L)}{(b_K + b_L)^2} (\overline{Q_S} - F_{K0} - Q_{L0} - (a_K + a_L)\text{Var}(D)) \right]^{1/2} - 1 \right\}$$
$$(5.17)$$

If both of the quadratic coefficients are positive, then it follows from (5.17) that increasing variance of the surface thermal disequilibrium must be accompanied by a decrease in the time-mean surface thermal disequilibrium. This has also been dis-

cussed by *Randall et al.* (1991), who used an exponential function for surface enthalpy flux, assumed a sinusoidal surface temperature in time, and numerically solved for the decrease in time-mean surface temperature that was associated with a given amplitude of surface temperature variability.

It is less obvious how an increase in the variance of the surface thermal disequilibrium affects the time-mean partitioning of surface energy balance between longwave cooling and turbulent enthalpy fluxes. Here we will show that increasing variance shifts the balance toward the flux that is more strongly nonlinear; generally speaking this is the turbulent enthalpy flux, as the nonlinearity of the Stefan-Boltzmann equation is small compared to the nonlinearities associated with surface turbulent fluxes of sensible and latent heat. We seek to calculate the sign of the derivative of the surface enthalpy flux, $\overline{F_K}$, with respect to the variance of the surface thermal disequilibrium, $\mathrm{Var}(D)$. Writing the total derivatives of $\overline{F_K}$ and $\overline{Q_L}$ with respect to $\mathrm{Var}(D)$ gives:

$$\frac{d\overline{F_K}}{d\mathrm{Var}(D)} = a_K + b_K \frac{d\overline{D}}{d\mathrm{Var}(D)} + a_K \frac{d\overline{D}^2}{d\mathrm{Var}(D)} \tag{5.18}$$

$$\frac{d\overline{Q_L}}{d\mathrm{Var}(D)} = a_L + b_L \frac{d\overline{D}}{d\mathrm{Var}(D)} + a_L \frac{d\overline{D}^2}{d\mathrm{Var}(D)}. \tag{5.19}$$

But we also know that $d\overline{Q_L}/d\mathrm{Var}(D) = -d\overline{F_K}/d\mathrm{Var}(D)$, so we can subtract (5.19) from (5.18) after dividing by a_L and a_K to eliminate many terms and obtain:

$$\left(\frac{1}{a_K} + \frac{1}{a_L} \right) \frac{d\overline{F_K}}{d\mathrm{Var}(D)} = \frac{d\overline{D}}{d\mathrm{Var}(D)} \left(\frac{b_K}{a_K} - \frac{b_L}{a_L} \right). \tag{5.20}$$

As shown above, $\partial \overline{D}/\partial \mathrm{Var}(D)$ is negative – increasing the variance of the surface disequilibrium decreases its time-mean value – and both a's are also positive, so:

$$\mathrm{sgn}\left(\frac{d\overline{F_K}}{d\mathrm{Var}(D)} \right) = \mathrm{sgn}\left(\frac{b_L}{a_L} - \frac{b_K}{a_K} \right). \tag{5.21}$$

If the longwave radiative cooling is more linear than the turbulent surface enthalpy flux, then the turbulent surface enthalpy flux will increase, at the expense of longwave cooling, as the variance of surface temperature increases. The phrase "more linear"

145

here is mathematically specific, in that it refers to a ratio of first-order and second-order coefficients in the expansion of the fluxes about a reference state. For blackbody radiation, and bulk formulae for surface turbulent fluxes with constant exchange coefficient c_K, the ratios of these coefficients are given by:

$$\frac{b_L}{a_L} = \frac{4\sigma T_0^3}{6\sigma T_0^2} = \frac{2}{3}T_0 \tag{5.22}$$

$$\frac{b_K}{a_K} = \frac{\rho c_K |\mathbf{v}|(L_v dq^*/dT + c_p)}{\rho c_K |\mathbf{v}| L_v d^2q^*/dT^2} \approx (1+B_e)\frac{RT_0^2}{\epsilon L_v}, \tag{5.23}$$

where T_0 is a reference temperature, and B_e is the equilibrium Bowen ratio, $c_p/(L_v dq^*/dT)$ (e.g., *Hartmann* (1994)). For $T_0 = 290$ K, $b_L/a_L \approx 193$, while $b_K/a_K \approx 24$; longwave radiation is much more linear than turbulent enthalpy transfer. Based on the fit in Figure 5-16, b_K/a_K is approximately 26, similar to our estimate here from the Clausius-Clayperon nonlinearity alone. The turbulent heat fluxes in the model are also affected by wind speeds, and by the direct dependence of the transfer coefficient c_K on D.

5.10   Appendix B: Linear Sea Breeze Theory: Equations with Damping

Following *Rotunno* (1983) and *Robinson et al.* (2008), we start with the Boussinesq equation set, linearized about a resting atmosphere with no horizontal temperature gradients, and modified for cylindrical geometry only in the continuity equation:

$$\frac{\partial u}{\partial t} = -\frac{1}{\rho}\frac{\partial p}{\partial r} - \alpha u \tag{5.24}$$

$$\frac{\partial w}{\partial t} - b = -\frac{1}{\rho}\frac{\partial p}{\partial z} \tag{5.25}$$

$$\frac{\partial b}{\partial t} + N^2 w = B - \alpha b \tag{5.26}$$

$$0 = \frac{1}{r}\frac{\partial}{\partial r}(ru) + \frac{\partial w}{\partial z}. \tag{5.27}$$

In (5.24)-(5.27), u is the radial wind, p is the pressure perturbation from a background hydrostatic profile, w is the vertical wind, b is the buoyancy, N is the Brunt-Vaisala frequency, α is a Rayleigh damping rate, and B is a buoyancy forcing function, which is periodic in time and confined in spatial extent to the island. We define a stream-function ψ to satisfy the continuity equation:

$$u = \frac{\partial \psi}{\partial z} \tag{5.28}$$

$$w = -\frac{1}{r}\frac{\partial}{\partial r}(r\psi). \tag{5.29}$$

Then, by cross-differentiating and adding the momentum equations to eliminate the pressure gradient terms, and combining the time derivative of this with the buoyancy equation and its time-derivative, we can obtain an equation for ψ alone:

$$\left[\frac{\partial^2}{\partial t^2} + \alpha\frac{\partial}{\partial t} + N^2\right]\left(\frac{\partial^2 \psi}{\partial r^2} + \frac{1}{r}\frac{\partial \psi}{\partial r} - \frac{\psi}{r^2}\right) +$$
$$\left[\frac{\partial^2}{\partial t^2} + 2\alpha\frac{\partial}{\partial t} + \alpha^2\right]\frac{\partial^2 \psi}{\partial z^2} = -\frac{\partial B}{\partial r}. \tag{5.30}$$

With the additional assumption that solutions are periodic in time ($\psi \sim e^{i\omega t}$), $\partial/\partial t \rightarrow i\omega$, and we obtain:

$$\left(N^2 - \omega^2 + i\omega\alpha\right)\left(\frac{\partial^2 \psi}{\partial r^2} + \frac{1}{r}\frac{\partial \psi}{\partial r} - \frac{\psi}{r^2}\right) +$$
$$\left(\alpha^2 - \omega^2 + 2i\omega\alpha\right)\frac{\partial^2 \psi}{\partial z^2} = -\frac{\partial B}{\partial r}. \tag{5.31}$$

This differs only in the formulation of the Laplacian from the corresponding Cartesian equation:

$$\left(N^2 - \omega^2 + i\omega\alpha\right)\frac{\partial^2 \psi}{\partial x^2} + \left(\alpha^2 - \omega^2 + 2i\omega\alpha\right)\frac{\partial^2 \psi}{\partial z^2} = -\frac{\partial B}{\partial x}. \tag{5.32}$$

In these equations, note that since $N^2 >> \omega^2$, the undamped equations ($\alpha = 0$) are hyperbolic, and the damped equations become elliptic when $\alpha > \omega$, or if the damping time scale is smaller than the time scale of the oscillating buoyancy forcing.

5.11 Appendix C: On the Resonant Response in *Robinson et al.* (2008)

In this section, we elaborate on the work of *Robinson et al.* (2008), hereafter RSL08. RSL08 explore the response of a dry, Boussinesq, weakly damped fluid with uniform stratification, to a buoyancy forcing function that is Gaussian in x, exponentially decaying in z, and sinusoidal in time. They obtain solutions by Fourier transforming the governing equations in space, solving an ODE for the vertical structure of the solution as a function of wavenumber, and then analytically evaluating the inverse spatial Fourier transform at $x = z = 0$, to obtain the maximum absolute value of the pressure perturbation at the time when buoyancy forcing is maximum. Here, we extend their results and show that their choice to evaluate the expression for perturbation surface pressure only at the time of maximum heating allows a 'resonance' to appear where one may not really exist.

Modifying terminology for consistency with the rest of this paper [(σ, H, a_0) from RSL08 here become (ω, z_0, r_I)], we take equation (9) of RSL08 as a starting point:

$$\hat{p}(k, z, t) = \frac{\hat{B}(k, z)}{\overline{\omega}[(1/z_0)^2 + \gamma^2]} \left[\frac{i}{z_0} e^{z/z_0} - \gamma e^{i\gamma z} \right], \tag{5.33}$$

where hat symbols denote Fourier transforms, k is the wavenumber in x, z_0 is the scale height of the buoyancy forcing, $\overline{\omega} = \omega - i\alpha$ is the angular frequency of the buoyancy forcing, modified slightly by the small damping parameter α, $\gamma \approx N|k|/\overline{\omega}$ is a vertical wavenumber (the absolute value on k ensures energy propagation is upwards), and $\hat{B}$ is the Fourier transform of the buoyancy forcing:

$$\hat{B}(k, t) = \frac{B_0 r_I}{\sqrt{2\pi}} e^{-k^2 r_I^2/4} e^{i(\omega t - \pi/2)}. \tag{5.34}$$

If we drop the small damping component of $\overline{\omega}$, and take the inverse Fourier transform

of the pressure, we obtain:

$$p(x, z, t) = \text{Re}\left[\frac{1}{\sqrt{2\pi}}\int_{-\infty}^{\infty}\hat{p}(k, z, t)e^{ikx}dk\right]. \tag{5.35}$$

Evaluating the integrand at $x = z = 0$, and plugging in the expressions from above for $\hat{p}(k, z, t)$, gives:

$$p(0, 0, t) = \frac{B_0 r_I}{2\pi}\int_{-\infty}^{\infty}\text{Re}\left[e^{i(\omega t - \pi/2)}(i/z_0 - N|k|/\omega)\right] \times$$
$$\frac{e^{-k^2 r_I^2/4}}{\omega[(1/z_0)^2 + (Nk/\omega)^2]}dk. \tag{5.36}$$

RSL08 proceed to further simplify this expression by considering only $t = \pi/(2\omega)$; however, we will evaluate the surface pressure at the island center at all times, and show that it substantially alters the interpretation of the results. To simplify the algebra in (5.36), we adopt the following definitions:

$$\tilde{k} = Nz_0 k/\omega \tag{5.37}$$
$$s = r_I\omega/(2Nz_0). \tag{5.38}$$

Then, taking the real part of the inverse transform, we obtain:

$$p(0, 0, t) = -\frac{B_0 z_0}{\pi\omega}\cos(\omega t - \pi/2)\int_{-\infty}^{\infty}\frac{se^{-s^2\tilde{k}^2}}{1 + \tilde{k}^2}|\tilde{k}|d\tilde{k}$$
$$-\frac{B_0 z_0}{\pi\omega}\sin(\omega t - \pi/2)\int_{-\infty}^{\infty}\frac{se^{-s^2\tilde{k}^2}}{1 + \tilde{k}^2}d\tilde{k}. \tag{5.39}$$

Both integrals are even functions; we multiply by 2 and transform the bounds of integration to $[0, \infty]$. Also, factoring out e^{s^2} from each integral, we obtain:

$$p(0, 0, t) = -\frac{B_0 z_0 se^{s^2}}{\pi\omega}\cos(\omega t - \pi/2)\int_0^{\infty}\frac{e^{-s^2(1+\tilde{k}^2)}}{1 + \tilde{k}^2}2|\tilde{k}|d\tilde{k}$$
$$-\frac{2B_0 z_0 se^{s^2}}{\pi\omega}\sin(\omega t - \pi/2)\int_0^{\infty}\frac{e^{-s^2(1+\tilde{k}^2)}}{1 + \tilde{k}^2}d\tilde{k}. \tag{5.40}$$

As in RSL08, with a change of variables $(t' = 1 + \tilde{k}^2)$, the first integral in (5.40)

149

becomes $E_i(1, s^2)$:

$$E_i(1, s^2) = \int_1^\infty \frac{e^{-s^2 t'}}{t'} dt'. \tag{5.41}$$

The second integral in (5.40) is related to Owen's T-function:

$$T(h, a) = \frac{1}{2\pi} \int_0^a \frac{e^{-\frac{h^2}{2}(1+x^2)}}{1+x^2} dx. \tag{5.42}$$

Owen (1980) (Table 2.4 p. 414), gives an identity for the relevant limit that $a \to \infty$:

$$
\begin{aligned}
T(h, \infty) &= \frac{1}{2}\left(1 - \frac{1}{\sqrt{2\pi}} \int_{-\infty}^h e^{-\frac{x^2}{2}} dx\right) \\
&= \frac{1}{4}\mathrm{erfc}(h/\sqrt{2}),
\end{aligned} \tag{5.43}
$$

where $\mathrm{erfc}(\cdot)$ is the complementary error function:

$$\mathrm{erfc}(h) = \frac{2}{\sqrt{\pi}} \int_h^\infty e^{-x^2} dx. \tag{5.44}$$

Using this information, we find that the second integral in (5.40) is given by:

$$\int_0^\infty \frac{e^{-s^2(1+\tilde{k}^2)}}{1+\tilde{k}^2} d\tilde{k} = 2\pi T(s\sqrt{2}, \infty) = \frac{\pi}{2}\mathrm{erfc}(s). \tag{5.45}$$

From this, we finally obtain a closed form for the surface pressure perturbation at the island center:

$$p(0,0,t) = -\frac{B_0 z_0}{\omega}\left(f_0(s)\cos\left(\omega t - \pi/2\right) + f_1(s)\sin\left(\omega t - \pi/2\right)\right), \tag{5.46}$$

where $f_0(s)$ and $f_1(s)$ are functions that scale the pressure perturbation as functions of nondimensional island size, s:

$$
\begin{aligned}
f_0(s) &= \pi^{-1} s e^{s^2} E_i(1, s^2) \\
f_1(s) &= s e^{s^2} \mathrm{erfc}(s).
\end{aligned}
$$

$$\tag{5.47}$$
$$\tag{5.48}$$

Figure 5-17 shows a plot of these two functions; while f_0 has a local maximum
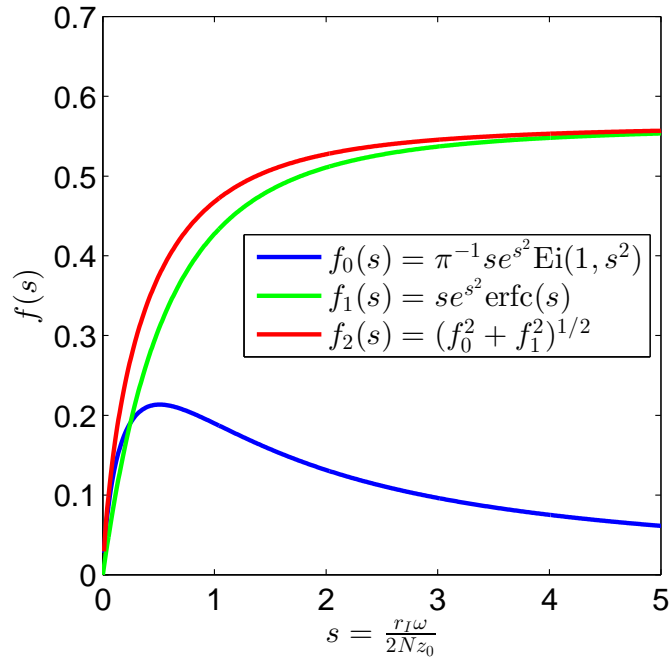
150

Figure 5-17: Plot of scaling functions $f_0(s)$ (blue) and $f_1(s)$ (green) for the strength of the surface pressure response to an oscillatory heating function that is gaussian in the horizontal, in linear, dry, Boussinesq sea breeze theory (See Appendix 5.11). The function $f_0(s)$ is essentially the same as that shown in Figure 1 of *Robinson et al.* (2008), except that it is not multiplied by the pressure drop scale factor, $-B_0 z_0/\omega$. The red curve shows the magnitude of $f_0(s)$ and $f_1(s)$ when they are added in quadrature, as they are in the time-dependent solution for the minimum surface pressure.

for $s = 0.5$, f_1 asymptotically increases towards a value of $1/\sqrt{\pi}$. Furthermore, when the two are summed in quadrature, the amplitude of the overall response has no local maximum as a function of island size. The surface pressure perturbation, evaluated at the time of maximum surface pressure perturbation, does not show evidence of having a resonance; the theoretical curves plotted by RSL08 are thus to some extent an artifact of choice of sampling time.

Chapter 6

Closing Remarks

To return to the conceit of Chapter 1, wherein this thesis is a conversation, between the characters of land-atmosphere interaction, on the one hand, and radiative-convective equilibrium, on the other; then this conversation now draws to a close. There is much that has been said here that rests on conversations past, much that could presently and productively be said in the presence of the other myriad characters in the climate system, much that has been left unsaid for the future. But all conversations must end.

6.1   Summary of Key Results

In Chapter 2, I developed the idea of the absorption-weighted zenith angle, which is defined mathematically and well-posed if the albedo is a monotonic and smooth function of the cosine of the solar zenith angle. If the albedo depends nearly linearly on the solar zenith angle, as is the case for the cloudy sky in both highly idealized calculations and more realistic radiative transfer calculations, then the absorption-weighted zenith angle is nearly equal to the insolation-weighted zenith angle. I showed that for a range of sky conditions and atmospheric temperature profiles, that the insolation-weighted zenith angle is a less biased choice than the commonly-used daytime-weighted zenith angle. Biases on the order of ~ 10 W/m² are likely common in idealized modeling simulations, solely as a result of the too-high or too-low choice of the solar zenith

angle. Moving forward, I hope that my findings will help to standardize the choice of solar zenith angle in idealized climate models; simulations with such models have only begun to tap into a wellspring of interesting questions relating to nonlinearities in the climate system.

In Chapter 3, I studied the time scales of relaxation toward radiative-convective equilibrium with an interactive surface temperature. I find that there is a long time scale of approach to equilibrium $\tau_C \approx (C_A + C_S)/B$, where C_A is the effective atmospheric heat capacity, C_S the surface heat capacity, and B is the change in outgoing longwave radiation with respect to surface air temperature, nearly equal to the inverse of the climate sensitivity. For a standard value of $B \sim 1.25$ W/m^2/K (e.g., *Soden and Held* (2006)), a dry atmospheric heat capacity ($C_{A,\mathrm{dry}} \sim 8 \times 10^6$ J/m^2/K) and a vanishing surface heat capacity would give a relaxation time scale on the order of 75 days. But the inclusion of the latent heat capacity of the atmosphere, and the amplification of temperature changes aloft, relative to surface temperature changes, substantially increase C_A above its dry value by as much as a factor of 2 to 3. Relaxation time scales can thus be as large as several hundred days, even when the thermal inertia of the surface vanishes. I suggest that this finding may have relevance to recent work that has suggested delayed monsoon onset, and an increase in the lag of tropical rainfall relative to peak solar forcing, under elevated CO_2. This work may also be relevant to "equable climates" of the deep past, which were much warmer and had less seasonal variation in temperatures, especially over northern hemisphere continents. It is plausible that the greater effective thermal inertia of the atmospheric column at warm temperatures could be partially responsible for this reduction in seasonality.

In Chapter 4, I developed a framework for understanding the sensitivity of near-surface temperatures to the properties of the land surface, including surface wetness, albedo, and roughness. For the idealized equilibrium boundary layer model of *Betts* (2000), I formulated an analytic sensitivity theory, where changes in land surface properties are treated as forcings, which are modulated by feedbacks to solve for a near-surface temperature response. I discuss the application of the theory to the case of physiological forcing by carbon dioxide; elevated atmospheric concentrations of

CO$_2$ have been shown to reduce the number and aperture of plant stomata, resulting in a reduction in the surface conductance to water vapor (g_v), other things equal. I estimate that a doubling of CO$_2$, which would lead to a $\sim 20\%$ reduction in g_v, would lead to a rise in air temperatures by ~ 0.5 K over moist and warm land surfaces. The theory could be extended to explore the response of near-surface temperatures to synoptic variability, or systematic changes in free-tropospheric temperature, and could also be used in its current state to look at the magnitude of regional temperature change that would be expected to result from anthropogenic disturbances like urbanization and agricultural expansion.

Finally, in Chapter 5, I tested the hypothesis that island precipitation enhancement is a result of rectification of the diurnal cycle. I performed simulations of radiative-convective equilibrium in a three-dimensional cloud-system resolving model, where the surface heat capacity is set to a spatially heterogeneous pattern, with low values representing an island, and higher values for the surrounding slab ocean. I find that the interaction of the diurnal cycle with this spatially variable surface heat capacity indeed rectifies into a mean circulation, with ascent over the island and subsidence elsewhere, especially in a dry ring in the immediate environs of the island. Rainfall in the time-mean is more than doubled over the island, as compared to the background ocean. I suggest a dynamical rectification mechanism, related to the interaction of convection and stability in a dry, unstratified, nonrotating fluid subjected to a buoyancy forcing that is localized in space, and periodic in time, but with zero-mean value. I find that it is difficult to explain the scaling with island size of moisture convergence over the island, but that linear sea breeze theory may explain the scaling with island size of the lag between peak surface enthalpy flux forcing and peak rainfall. It appears that island precipitation enhancement can emerge solely as a result of organized diurnal variability of surface enthalpy fluxes over an island, sometimes in defiance of conventional column-energy budget arguments regarding time-mean ascent or descent. The warming of the upper troposphere with inclusion of an island suggests that the increase in island area of the Maritime Continent over the past 3-5 million years could have strengthened the Walker Circulation, but more

work is needed to shore up this speculative result, preferably with a model that can resolve a range of scales of circulation, from the convective to the planetary.

6.2   Big Questions and Future Work

One of the most intriguing questions in climate, both academic and practical in nature, is whether the climate system has multiple equilibria for a given external forcing. The existence of multiple equilibria in the climate system as a whole, or in a subcomponent of the climate system, would imply that the climate is not uniquely determined as a function of boundary conditions, and also that the climate could abruptly jump from one state to another if perturbed enough from one conditionally stable equilibrium towards another. Multiple equilibria and instability have been a prominent subject of research in a range of subdomains of the climate system, ranging from radiative-convective equilibrium in the tropical atmosphere (*Sessions et al.*, 2010; *Emanuel et al.*, 2014), to subtropical low clouds and precipitation-aerosol interactions (*Feingold et al.*, 2010), to mid-latitude soil moisture-precipitation feedbacks (*D'Odorico and Porporato*, 2004), to interaction of sea ice with clouds and ocean heat transport (*Abbot*, 2008; *Rose*, 2010).

The primary point of contact of this thesis with potential for instability and multiple equilibria lies with an aspect of land-atmosphere interaction that I have entirely neglected: the feedback between precipitation and soil moisture, and the stability of soil moisture evolution. It may be possible to address this question head-on, by looking at radiative-convective equilibrium over land directly; a group at Columbia has done this and finds multiple equilibria associated with different partitioning of water between atmosphere and subsurface (*Rochetin et al., personal communication*). However, I believe that this direct approach, of attempting to simulate radiative-convective equilibrium over land, is unrealistic. The simplest realistic land-atmosphere system must also involve some ocean; no region of land sustains an isolated hydrologic cycle, so allowing moisture convergence or divergence from the atmospheric column over the land is essential. Although the simulations in this thesis in Chapters 4 and 5 allow

for such moisture convergence or divergence, they do not close the hydrologic cycle by allowing soil moisture to be determined prognostically. Simulations that extend the work in Chapter 5, with varied values of surface wetness (albeit still fixed in time), suggest that such coupling would be highly stable; islands of the size I have simulated would get rainier as the soil dried out, or less rainy as the soil moistened, tending to drive the system to a statistically stable state. Addressing this stability question directly, in my view, would be best done by simply adding a simple prognostic soil moisture evolution equation to the existing simulation geometry; either a bucket model or a slightly more sophisticated treatment (as in *Brubaker and Entekhabi* (1995)) could be used. An alternative could be to use an all-land lower boundary, but with the WTG approximation (*Sobel et al.*, 2001) allowing for vertical motion, and moisture convergence or divergence from the atmospheric column.

Extension of work in Chapter 4 to account for closure of the hydrological cycle, and soil moisture-precipitation feedbacks, could be done by including soil moisture as one of the prognostic variables, as in past studies (*Brubaker and Entekhabi*, 1995; *Entekhabi and Brubaker*, 1995; *Brubaker and Entekhabi*, 1996). This approach, however, is treacherous, because it makes the underlying model structure much more complex – perhaps enough so that analytic sensitivity analysis fails – but at the same time, makes very strong demands regarding simplification of convection and precipitation, which are likely to be wrong under many circumstances. My approach has been to treat surface conductance to water vapor as a fixed external parameter, which skirts around the issue of soil moisture in a somewhat primitive way. Perhaps future studies can find a way to combine some of my results with the prognosis of soil moisture.

Another big question in climate relates to the importance of interaction between variability and the mean state. This subject includes issues relating to effects of spatial variability on the mean state; for example, spatial variability in column water vapor can translate into a higher average emission of radiation for the same mean water vapor concentration, because outgoing radiation is a nonlinear function of column water vapor (*Pierrehumbert*, 2010). But variability-mean state interactions also lie the root of any discussion of weather-climate interactions; is weather simply drawn at

random from a bag that is predetermined by climate, or does weather alter the bag from which it is drawn? This thesis has multiple threads that intersect the complex problem of variability-mean state interaction.

In Chapter 2, I suggest that idealized climate model simulations are less readily comparable to each other, and to the real climate, because of biases in albedo. This finding is important because the question of how spatial variability of insolation and dynamics affect the global-mean climate is both profound and unanswered, and it is also a question that that idealized climate models are well-poised to answer, if biases can be minimized. I hope that at some point in the near future, an RCE-MIP, or some otherwise-named model intercomparison project, will remove insolation gradients and possibly also rotation from a set of climate models, and help to identify whether the Earth's mean climate deviates substantially from radiative-convective equilibrium on a sphere. If, as expected, Earth's mean temperature deviates considerably from RCE on a sphere, then the natural question becomes: what are the most important nonlinearities that interact with spatial variability in insolation and rotation? If the Earth's mean temperature does not deviate substantially from this state, the question becomes: why, with all of its complexities and potential nonlinearities, would simulation of mean planetary temperature be such a linear problem?

Results from Chapter 3 suggest a connection in the opposite direction: the mean temperature of the atmosphere affects its thermal inertia, and thus changes in the mean temperature could tend to dampen or amplify forced variability. Results from Chapter 4 go both ways, relating to both impacts of variability on the mean state, and impacts of the mean state on variability. I find that the evaporative forcing due to changing surface conductance to water vapor is nonlinear; this indicates that spatial or temporal variability in surface wetness could have an impact on the mean state. The theory anticipates that a region with more temporally variable soil moisture will be, on average, warmer, than a region with otherwise similar properties but less variance in soil moisture. The sensitivity of the equilibrium boundary layer is also found to depend on numerous aspects of the base state; in particular, a drier surface has less ability to dissipate external variability via evaporation. The extent to which either of

these variability-mean state interactions applies to real-world data, or climate model output, is unknown, but a potentially interesting topic for future work.

Chapter 5 intersects with the big idea of variability-mean state interaction in many places. I hypothesize that the island, sheerly by acting as to increase the variance of surface buoyancy flux, may considerably alter both the mean distribution of rainfall, and the thermal structure of the atmosphere in the whole domain. I also discuss how the increased variability of surface temperature over land translates to a decrease in the time-mean land surface temperature. Rectification mechanisms provide a clear path by which variability can affect the mean state.

Finally, this thesis brushes past the big and thorny question of clouds and climate in several places. The strong dependence of cloud albedo on zenith angle was mostly unknown to me prior to writing Chapter 2; that the zenith angle is generally low in the tropics may be an important reason why the net cloud radiative effect is nearly zero on average over the tropics. In Chapter 4, the issue of clouds and climate is briefly addressed, but only to discuss how the 2-column model is not really up to the task of simulating realistic clouds. The role of cloud feedbacks in the sensitivity of the land-boundary layer system remains an important open question. Finally, in Chapter 5, I find that variability in cloud timing that is correlated or anticorrelated with solar insolation can have large impacts on the surface energy budget over the island, and also on the domain-mean temperature. Given the deficiencies in the timing of convection in global climate models, it seems unlikely that models typically capture the correct diurnal cycle of cloud fraction, and considerable biases may result.

I hope that this thesis has been fun at times for the reader, and that this section has provided both a sense of closure, and a sense of expansive possibility. My time at MIT has merely reinforced my sense of the vastness of what remains to be understood about climate, of the ponderous and looming bulk of the aforementioned big questions, and the multitude of those unnamed and unknown. I can only hope that some of the ideas in this thesis, and the future directions proposed, help to chip away at the big questions in climate, and in some way contribute to sculpting our future understanding.

Bibliography

Abbot, D., 2008: A high-latitude convective cloud feedback, Harvard PhD Thesis, 145 pp.

Abbot, D., and K. Emanuel, 2007: A tropical and subtropical land–sea–atmosphere drought oscillation mechanism. *J. Atmos. Sci.*, **64**, 4458–4468, doi:10.1175/2007JAS2186.1.

Abbot, D., and E. Tziperman, 2008: Sea Ice, High Latitude Convection, and Equable Climates. *Geophys. Res. Lett.*, **35**, L03702, doi:10.1029/2007GL032286.

Allen, R., L. Pereira, D. Raes, and M. Smith, 1998: *Crop evapotranspiration: guidelines for computing crop water requirements, Irrigation and Drainage Paper 56*, 300 pp., United Nations FAO, Rome.

Andrews, T., M. Doutriaux-Boucher, O. Boucher, and P. Forster, 2011: A regional and global analysis of carbon dioxide physiological forcing and its impact on climate. *Clim. Dynam.*, **36**, 783–792, doi:10.1007/s00382-010-0742-1.

As-syakur, A., T. Tanaka, T. Osawa, and M. Mahendra, 2013: Indonesian rainfall variability observation using TRMM multi-satellite data. *International Journal of Remote Sensing*, **34**, 7723–7738, doi:10.1080/01431161.2013.826837.

Barsugli, J., and D. Battisti, 1998: The basic effects of atmosphere-ocean thermal coupling on midlatitude variability. *J. Atmos. Sci.*, **55**, 477–493.

Barsugli, J., S. Shin, and P. Sardeshmukh, 2005: Tropical Climate Regimes and Global Climate Sensitivity in a Simple Setting. *J. Atmos. Sci.*, **62**, 1226–1240.

Beringer, J., and N. Tapper, 2002: Surface energy exchanges and interactions with thunderstorms during the Maritime Continent Thunderstorm Experiment (MC-TEX). *J. Geophys. Res.*, **107**(D21), 4552, doi:10.1029/2001JD001431.

Betts, A., 2000: Idealized model for equilibrium boundary layer over land. *J. Hydrometeor.*, **1**, 507–523.

Betts, A., 2004: The Diurnal Cycle Over Land. *Forests at the Land-Atmosphere Interface*, eds M. Mencuccini, J. Grace, J. Moncrieff, and K. McNaughton, CABI Publishing, Cambridge, 73–93.

Betts, A., and J. Chiu, 2010: Idealized model for changes in equilibrium temperature, mixed layer depth, and boundary layer cloud over land in a doubled CO_2 climate. *J. Geophys. Res.*, **115**, D19108, doi:10.1029/2009JD012888.

Betts, A., and W. Ridgway, 1988: Coupling of the radiative, convective, and surface fluxes over the equatorial pacific. *J. Atmos. Sci.*, **45**, 522–536.

Betts, A., and W. Ridgway, 1989: Climatic equilibrium of the atmospheric convective boundary layer over a tropical ocean. *J. Atmos. Sci.*, **46**, 2621–2641.

Betts, R., P. Cox, M. Collins, P. Harris, C. Huntingford, and C. Jones, 2004: The role of ecosystem-atmosphere interactions in simulated amazonian precipitation decrease and forest dieback under global climate warming. *Theor. Appl. Climatol.*, **78**, 157–175, doi:10.1007/s00704-004-0050-y.

Biasutti, M., S. Yuter, C. Burleyson, and A. Sobel, 2012: Very high resolution rainfall patterns measured by TRMM precipitation radar: seasonal and diurnal cycles. *Clim. Dyn.*, **39**, 239–258, doi:10.1007/s00382-011-1146-6.

Bony, S., and K. Emanuel, 2001: A Parameterization of the Cloudiness Associated with Cumulus Convection; Evaluation Using TOGA COARE Data. *J. Atmos. Sci.*, **58**, 3158–3183.

Bordoni, S., and T. Merlis, 2013: Response of aquaplanet monsoons to changes in longwave radiation. Paper presented on 17 June at 19th Conference on Atmospheric and Oceanic Fluid Dynamics, Am. Meteorol. Soc., Newport, Rhode Island.

Boucher, O., A. Jones, and R. Betts, 2009: Climate response to the physiological impact of carbon dioxide on plants in the Met Office Unified Model HadCM3. *Clim. Dynam.*, **32**, 237–249, doi:10.1007/s00382-008-0459-6.

Bretherton, C., P. Blossey, and M. Khairoutdinov, 2005: An energy-balance analysis of deep convective self-aggregation above uniform SST. *J. Atmos. Sci.*, **62**, 4273–4292, doi:10.1175/JAS3614.1.

Bretherton, C., P. Blossey, and C. Jones, 2013: Mechanisms of marine low cloud sensitivity to idealized climate perturbations: A single-LES exploration extending the CGILS cases. *J. Adv. Model. Earth Sys.*, **5**, 316–337, doi:10.1002/jame.20019.

Brubaker, K., and D. Entekhabi, 1995: An analytic approach to modeling land-atmosphere interaction 1: Construct and Equilibrium behavior. *Water Resources Research*, **31**, 619–632.

Brubaker, K., and D. Entekhabi, 1996: Analysis of Feedback Mechanisms in land-atmosphere interaction. *Water Resources Research*, **32**, 1343–1357.

Cao, L., G. Bala, K. Caldeira, R. Nemani, and G. Ban-Weiss, 2009: Climate response to physiological forcing of carbon dioxide simulated by the coupled community atmosphere model (CAM3.1) and community land model (CLM3.0). *Geophys. Res. Lett.*, **36**, L10402, doi:10.1029/2009GL037724.

Cao, L., G. Bala, K. Caldeira, R. Nemani, and G. Ban-Weiss, 2010: Importance of carbon dioxide physiological forcing to future climate change. *Proc. Natl. Acad. Sci. (USA)*, **107**, 9513–9518, doi:10.1073/pnas.0913000107.

Carbone, R., J. Wilson, T. Keenan, and J. Hacker, 2000: Tropical Island Convection in the Absence of Significant Topography. Part I: Life Cycle of Diurnally Forced Convection. *Mon. Wea. Rev.*, **128**, 3459–3480.

Charney, J., 1975: Dynamics of deserts and drought in the Sahel. *Quart. J. Roy. Meteor. Soc.*, **101**, 193–202.

Clement, A., P. DiNezio, and C. Deser, 2011: Rethinking the Ocean's role in the southern oscillation. *J. Clim.*, **24**, 4056–4072, doi:10.1175/2011JCLI3973.1.

Clough, S., M. Shephard, E. Mlawer, J. Delamere, M. Iacono, K. Cady-Pereira, S. Boukabara, and P. Brown, 2005: Atmospheric radiative transfer modeling: a summary of the AER codes. *J. Quant. Spectrosc. Radiat. Transfer*, **91**, 233–244.

Connolly, P., T. Choularton, M. Gallagher, K. Bower, M. Flynn, and J. Whiteway, 2006: Cloud-resolving simulations of intense tropical *Hector* thunderstorms: Implications for aerosol-cloud interactions. *Quart. J. Roy. Meteor. Soc.*, **132**, 3079–3106, doi:10.1256/qj.05.86.

Cox, P., R. Betts, C. Bunton, R. Essery, P. Rowntree, and J. Smith, 1999: The impact of new land surface physics on the GCM simulation of climate and climate sensitivity. *Clim. Dynam.*, **15**, 183–203.

Cronin, T., 2013: A sensitivity theory for the equilibrium boundary layer over land. *J. Adv. Model. Earth Syst.*, **5**, doi:10.1002/jame.20048.

Cronin, T., and K. Emanuel, 2013: The climate time scale in the approach to radiative-convective equilibrium. *J. Adv. Model. Earth Syst.*, **5**, doi:10.1002/jame.20049.

Crook, N., 2001: Understanding Hector: The Dynamics of Island Thunderstorms. *Mon. Wea. Rev.*, **129**, 1550–1563.

D'Odorico, P., and A. Porporato, 2004: Preferential states in soil moisture and climate dynamics. *Proc. Natl. Acad. Sci. (USA)*, **101**, 8848–8851, doi:10.1073/pnas.0401428101.

Davis, W., L. Schultz, and R. Ward, 1889: An investigation of the sea-breeze. *New Engl. Meteorol. Soc. Obser.*, **21**, 214–264.

Dayem, K., D. Noone, and P. Molnar, 2007: Tropical Western Pacific Warm Pool and Maritime Continent Precipitation Rates and Their Contrasting Relationships with the Walker Circulation. *J. Geophys. Res.*, **112**, D06101, doi:10.1029/2006JD007870.

Deardorff, J., 1978: Efficient Prediction of Ground Surface Temperature and Moisture, with Inclusion of a Layer of Vegetation. *J. Geophys. Res.*, **83:C4**, 1889–1903.

Dirmeyer, P., B. Cash, J. Kinter, T. Jung, L. Marx, M. Satoh, C. Stan, H. Tomita, P. Towers, N. Wedi, D. Achutavarier, J. Adams, E. Altshuler, B. Huang, E. Jin, and J. Manganello, 2012: Simulating the diurnal cycle of rainfall in global climate models: resolution versus parameterization. *Clim. Dyn.*, *39*, 399–418, doi:10.1007/s00382-011-1127-9.

Dong, B., J. Gregory, and R. Sutton, 2009: Understanding Land-Sea Warming Contrast in Response to Increasing Greenhouse Gases. Part I: Transient Adjustment. *J. Clim.*, **22**, 3079–3097, doi:10.1175/2009JCLI2652.1.

Donohoe, A., and D. Battisti, 2011: Atmospheric and Surface Contributions to Planetary Albedo. *J. Climate*, **24**, 4402–4418, doi:10.1175/2011JCLI3946.1.

Doutriaux-Boucher, M., M. Webb, J. Gregory, and O. Boucher, 2009: Carbon dioxide induced stomatal closure increases radiative forcing via a rapid reduction in low cloud. *Geophys. Res. Lett.*, **36**, L02703, doi:10.1029/2008GL036273.

Dwyer, J., M. Biasutti, and A. Sobel, 2013: The effect of greenhouse-gas-induced changes in SST on the seasonality of tropical precipitation. Paper presented on 29 May at 6th Northeast Tropical Workshop, SUNY Albany, Rensselaersville, New York.

Eddington, A., 1926: *The Internal Constitution of the Stars.* Cambridge University Press, London, 407 pp.

Emanuel, K., 1994: *Atmospheric Convection.* Oxford University Press, New York, 580 pp.

Emanuel, K., and A. Sobel, 2013: Response of tropical sea surface temperature, precipitation, and tropical cyclone-related variables to changes in global and local forcing. *J. Adv. Model. Earth Syst.*, **5**, 447–458, doi:10.1002/jame.20032.

Emanuel, K., A. Wing, and E. Vincent, accepted article, Radiative-Convective Instability. *J. Adv. Model. Earth Syst.*, doi:10.1002/2013MS000270.

Emanuel, K., and M. Zivkovic-Rothman, 1999: Development and evaluation of a convection scheme for use in climate models. *J. Atmos. Sci.*, **56**, 1766–1782.

Entekhabi, D., and K. Brubaker, 1995: An analytic approach to modeling land-atmosphere interaction 2: Stochastic Formulation. *Water Resources Research*, **31**, 633–643.

Fedorov, A., P. Dekens, M. McCarthy, A. Ravelo, P. DeMenocal, M. Barreiro, R. Pacanowski, and S. Philander, 2006: The Pliocene Paradox (Mechanisms for a Permanent El Niño). *Science*, **312**(5779), 1485–1489.

Feingold, G., I. Koren, H. Wang, H. Xue, and A. Brewer, 2010: Precipitation-generated oscillations in open cellular cloud fields. *Nature*, **466**, 849–852, doi:10.1038/nature09314.

Field, C., R. Jackson, and H. Mooney, 1995: Stomatal responses to increased CO_2: implications from the plant to the global scale. *Plant, Cell, and Environment*, **18**, 1214–1225.

Fu, Q., and K. Liou, 1993: Parameterization of the Radiative Properties of Cirrus Clouds. *J. Atmos. Sci.*, **50**, 2008–2025.

Guichard, F., J. Petch, J. Redelsperger, P. Bechtold, J. Charboreau, S. Cheinet, W. Grabowski, H. Grenier, C. Jones, M. Kohler, J. Piriou, R. Tailleux, and M. Tomasini, 2004: Modelling the diurnal cycle of deep precipitating convection over land with cloud-resolving models and single-column models. *Quart. J. Roy. Meteor. Soc.*, **130**, 3139–3172.

Hall, R., 2002: Cenozoic Geological and Plate Tectonic Evolution of SE Asia and the SW Pacific: Computer-Based Reconstructions, Model and Animations. *Journal of Asian Earth Sciences*, **20**, 353–431.

Halley, E., 1686: An historical account of the trade winds, monsoons, observable in the seas between and near the tropicks, with an attempt to assign physical cause to said winds. *Phil. Trans. Roy. Soc. London*, **16**, 153–168.

Hamilton, K., 1981: A Note on the observed diurnal and semidiurnal rainfall variations. *J. Geophys. Res.*, **86**(C12), 12122–12126.

Hartmann, D., 1994: *Global Physical Climatology*. Academic Press, International Geophysics Series Volume 56, San Diego, 409 pp.

Held, I., 2005: The gap between simulation and understanding in climate modeling. *Bull. Amer. Meteor. Soc.*, **80**, 1609–1614, doi:10.1175/BAMS-86-11-1609.

Held, I., and M. Suarez, 1974: Simple albedo feedback models of the icecaps. *Tellus*, **26**, 613–629.

Held, I., R. Hemler, and V. Ramaswamy, 1993: Radiative-Convective equilibrium with explicit two-dimensional moist convection. *J. Atmos. Sci.*, **50**, 3909–3927.

Hohenegger, C., and B. Stevens, 2013: Controls on and impacts of the diurnal cycle of deep convective precipitation. *J. Adv. Model. Earth Syst.*, **5**, doi:10.1002/2012MS000216.

Iacono, M., J. Delamere, E. Mlawer, M. Shephard, S. Clough, and W. Collins, 2008: Radiative forcing by long-lived greenhouse gases: Calculations with the AER radiative transfer models. *J. Geophys. Res.*, **113**, D13103, doi:10.1029/2008JD009944.

Jacobs, C., and H. De Bruin, 1992: The sensitivity of regional transpiration to land-surface characteristics: significance of feedback. *J. Clim.*, **5**, 683–698.

Jones, H., 1992: *Plants and Microclimate*, 2 ed., 428 pp., Cambridge University Press, Cambridge, UK.

Keenan, T., S. Rutledge, R. Carbone, J. Wilson, T. Takahashi, P. May, N. Tapper, M. Platt, J. Hacker, S. Selesky, M. Moncrieff, K. Saito, G. Holland, A. Crook, and K. Gage, 2000: The Maritime Continent Thunderstorm Experiment (MCTEX): Overview and Some Results. *Bull. Amer. Meteor. Soc.*, **81**, 2433–2455.

Khairoutdinov, M., and D. Randall, 2003: Cloud Resolving Modeling of the ARM Summer 1997 IOP: Model Formulation, Results, Uncertainties, and Sensitivities. *J. Atmos. Sci.*, **60**, 607–625.

Khairoutdinov, M., and C.-E. Yang, 2013: Cloud resolving modelling of aerosol indirect effects in idealised radiative-convective equilibrium with interactive and fixed sea surface temperature. *Atmos. Chem. Phys.*, **13**, 4133–4144, doi:10.5194/acp-13-4133-2013.

Kim, C., and D. Entekhabi, 1998: Feedbacks in the Land-surface and mixed-layer energy budgets. *Boundary-Layer Meteorology*, **88**, 1–21.

Kirtman, B., and E. Schneider, 2000: A Spontaneously Generated Tropical Atmospheric General Circulation. *J. Atmos. Sci.*, **57**, 2080–2093.

Lammertsma, E., H. de Boer, S. Dekker, D. Dilcher, A. Lotter, and F. Wagner-Cremer, 2011: Global CO_2 rise leads to reduced maximum stomatal conductance in florida vegetation. *Proc. Natl. Acad. Sci. (USA)*, **108**, 4035–4040, doi:10.1073/pnas.1100371108.

Li, Y., and R. Smith, 2010: Observation and Theory of the Diurnal Continental Thermal Tide. *J. Atmos. Sci.*, **67**, 2752–2765, doi:10.1175/2010JAS3384.1.

Liu, C., and E. Zipser, 2008: Diurnal cycles of precipitation, clouds, and lightning in the tropics from 9 years of TRMM observations. *Geophys. Res. Lett.*, **35**, L04819, doi:10.1029/2007GL032437.

Manabe, S., and R. Strickler, 1964: Thermal equilibrium of the atmosphere with a convective adjustment. *J. Atmos. Sci.*, **21**, 361–385.

Manabe, S., and R. Wetherald, 1967: Thermal equilibrium of the atmosphere with a given distribution of relative humidity. *J. Atmos. Sci.*, **24**, 241–259.

McNaughton, K., and T. Spriggs, 1986: A mixed-layer model for regional evaporation. *Boundary-Layer Meteorology*, **34**, 243–262.

Medlyn, B., C. Barton, M. Broadmeadow, R. Ceulemans, P. Angelis, M. Forstreuter, M. Freeman, S. Jackson, S. Kellomäki, E. Laitat, A. Rey, P. Roberntz, B. Sigurdsson, J. Strassemeyer, K. Wang, P. Curtis, and P. Jarvis, 2001: Stomatal conductance of forest species after long-term exposure to elevated CO_2 concentration: a synthesis. *New Phytologist*, **149**, 247–264.

Monteith, J., 1965: Evaporation and Environment. In: *The State and Movement of Water in Living Organisms*, Cambridge University Press, pp. 205–234.

Neale, R., and J. Slingo, 2003: The Maritime Continent and Its Role in the Global Climate : A GCM Study. *J. Climate*, **16**, 834–848.

Neelin, J., and I. Held, 1987: Modeling Tropical Convergence Based on the Moist Static Energy Budget. *Mon. Wea. Rev.*, **115**, 3–12.

Nilsson, J., and K. Emanuel, 1999: Equilibrium atmospheres of a two-column radiative-convective model. *Quart. J. Roy. Meteor. Soc.*, **125**, 2239–2264.

Nobel, P., 2008: *Physicochemical and Environmental Plant Physiology, Fourth Edition*. Academic Press, Oxford UK, 582 pp.

Notaro, M., S. Vavrus, and Z. Liu, 2007: Global vegetation and climate change due to future increases in CO_2 as projected by a fully coupled model with dynamic vegetation. *J. Clim.*, **20**, 70–90, doi:10.1175/JCLI3989.1.

Ochsner, T., R. Horton, and T. Ren, 2001: A New Perspective on Soil Thermal Properties. *Soil Science Society of America Journal*, **65**, 1641–1647.

Owen, D., 1980: A table of normal integrals. *Communications in Statistics — Simulation and Computation*, **9**, 389–419.

Pierrehumbert, R., 1995: Thermostats, Radiator Fins, and the Local Runaway Greenhouse. *J. Atmos. Sci.*, **52**, 1784–1806.

Pierrehumbert, R., 2002: The hydrologic cycle in deep-time climate problems. *Nature*, **419**, 191–198.

Pierrehumbert, R., 2010: *Principles of Planetary Climate*. Cambridge University Press, Cambridge, UK, 652 pp.

Pincus, R., H. Barker, and J. Morcrette, 2003: A fast, flexible, approximation technique for computing radiative transfer in inhomogeneous cloud fields. *J. Geophys. Res.*, **108**(D13), 4376, doi:10.1029/2002JD003322.

Popke, D., B. Stevens, and A. Voigt, 2013: Climate and Climate Change in a Radiative-Convective Equilibrium Version of ECHAM6. J. Adv. Model. Earth Sys., **5**, 1–14, doi:10.1029/2012MS000191.

Posselt, D., S. van den Heever, and G. Stephens, 2008: Trimodal cloudiness and tropical stable layers in simulations of radiative convective equilibrium. *Geophys. Res. Lett.*, **35**, L08802, doi:10.1029/2007GL033029.

Qian, J.-H., 2008: Why Precipitation Is Mostly Concentrated over Islands in the Maritime Continent. *J. Atmos. Sci.*, **65**, 1428–1441, doi:10.1175/2007JAS2422.1.

Ramanathan, V., 1976: Radiative Transfer Within the Earth's Troposphere and Stratosphere: A Simplified Radiative-Convective Model. *J. Atmos. Sci.*, **33**, 1330–1346.

Ramanathan, V., and J. Coakley, 1978: Climate Modeling Through Radiative-Convective Models. *Reviews of Geophysics and Space Physics*, **16**, 465–489.

Ramaswamy, V., et al., 2001: Radiative Forcing of Climate Change. In: *Climate Change 2001: The Scientific Basis. Contribution of Working Group I to the Third Assessment Report of the Intergovernmental Panel on Climate Change* [Houghton, J.T.,Y. Ding, D.J. Griggs, M. Noguer, P.J. van der Linden, X. Dai, K. Maskell, and C.A. Johnson (eds.)]. Cambridge University Press, Cambridge, United Kingdom and New York, NY, USA, 881 pp.

Randall, D., Harshvardhan, and D. Dazlich, 1991: Diurnal Variability of the Hydrologic Cycle in a General Circulation Model. *J. Atmos. Sci.*, **48**, 40–62.

Raymond, D., 1995: Regulation of moist convection over the west pacific warm pool. *J. Atmos. Sci.*, **52**, 3945–3959.

Raymond, D., S. Sessions, A. Sobel, and Z. Fuchs, 2009: The Mechanics of Gross Moist Stability. *J. Adv. Model. Earth Syst.*, *1*, doi:10.3894/JAMES.2009.1.9.

Renno, N., 1997: Multiple equilibria in radiative-convective atmospheres. *Tellus*, **49**(A), 423–438.

Renno, N., K. Emanuel, and P. Stone, 1994: Radiative-convective model with an explicit hydrologic cycle. I: Formulation and sensitivity to model parameters. *J. Geophys. Res.*, **99**, 14429–14441.

Robinson, F., M. Patterson, and S. Sherwood, 2013: A Numerical Modeling Study of the Propagation of Idealized Sea-Breeze Density Currents. *J. Atmos. Sci.*, **70**, 653–667, doi:10.1175/JAS-D-12-0113.1.

Robinson, F., S. Sherwood, D. Gerstle, C. Liu, and D. Kirshbaum, 2011: Exploring the Land-Ocean Contrast in Convective Vigor Using Islands. *J. Atmos. Sci.*, **68**, 602–618, doi:10.1175/2010JAS3558.1.

Robinson, F., S. Sherwood, and Y. Li, 2008: Resonant Response of Deep Convection to Surface Hot Spots. *J. Atmos. Sci.*, **65**, 276–286, doi:10.1175/2007JAS2398.1.

Romps, D., 2011: Response of Tropical Precipitation to Global Warming. *J. Atmos. Sci.*, **68**, 123–138, doi:10.1175/2010JAS3542.1.

Rose, B., 2010: Oceanic Control of the Sea Ice Edge and Multiple Equilibria in the Climate System, MIT PhD Thesis, 227 pp.

Rossow, W., and R. Schiffer, 1999: Advances in Understanding Clouds from ISCCP. *Bull. Amer. Meteor. Soc.*, **80**, 2261–2287.

Rotunno, R., 1983: On the Linear Theory of the Land and Sea Breeze. *J. Atmos. Sci.*, **40**, 1999–2009.

Sato, T., H. Miura, M. Satoh, Y. Takayabu, and Y. Wang, 2009: Diurnal Cycle of Precipitation in the Tropics Simulated in a Global Cloud-Resolving Model. *J. Climate*, **22**, 4809–4826, doi:10.1175/2009JCLI2890.1.

Schwarzschild, K., 1906: On the Equilibrium of the Sun's Atmosphere. in *Selected Papers on the Transfer of Radiation*, 1966: ed D. Menzel, Dover, 25–34.

Sellers, P., et al., 1996: Comparison of radiative and physiological effects of doubled atmospheric CO_2 on climate. *Science*, **271**, 1402–1406.

Sessions, S., S. Sugaya, D. Raymond, and A. Sobel, 2010: Multiple equilibria in a cloud-resolving model using the weak temperature gradient approximation. *J. Geophys. Res.*, **115**, D12110, doi:10.1029/2009JD013376.

Shukla, J., and Y. Mintz, 1982: Influence of Land-Surface Evapotranspiration on the Earth's Climate. *Science*, **215**, 1498–1501.

Simpson, J., T. Keenan, B. Ferrier, R. Simpson, and G. Holland, 1993: Cumulus mergers in the maritime continent region. *Meteorol. Atmos. Phys.*, **51**, 73–99.

Smith, E., A. Hsu, W. Crosson, R. Field, L. Fritschen, R. Gurney, E. Kanemasu, W. Kustas, D. Nie, W. Shuttleworth, J. Stewart, S. Verma, H. Weaver, and M. Wesely, 1992: Area-Averaged Surface Fluxes and Their Time-Space Variability Over the FIFE Experimental Domain. *J. Geophys. Res.*, **97**(D17), 18599–18622.

Sobel, A., C. Burleyson, and S. Yuter, 2011: Rain on small tropical islands. *J. Geophys. Res.*, **116**, 1–15, doi:10.1029/2010JD014695.

Sobel, A., J. Nilsson, and L. Polvani, 2001: The weak temperature gradient approximation and balanced tropical moisture waves. *J. Atmos. Sci.*, **58**, 3650–3665.

Soden, B., and I. Held, 2006: An assessment of climate feedbacks in coupled ocean-atmosphere models. *J. Climate*, **19**, 3354-3360, doi:10.1175/JCLI3799.1.

Takahashi, K., 2009: Radiative constraints on the hydrological cycle in an idealized radiative-convective equilibrium model. *J. Atmos. Sci.*, **66**, 77–91, doi:10.1175/2008JAS2797.1.

Tennekes, H., 1973: A model for the dynamics of the inversion above a convective boundary layer. *J. Atmos. Sci.*, **30**, 558–567.

Tompkins, A., and G. Craig, 1998: Radiative-convective equilibrium in a three-dimensional cloud-ensemble model. *Quart. J. Roy. Meteor. Soc.*, **124**, 2073–2097.

Tompkins, A., and G. Craig, 1998: Time-scales of adjustment to radiative-convective equilibrium in the tropical atmosphere. *Quart. J. Roy. Meteor. Soc.*, **124**, 2693–2713.

van Heerwaarden, C., J. Vila-Guerau de Arellano, A. Moene, and A. Holtslag, 2009: Interactions between dry-air entrainment, surface evaporation and convective boundary-layer development. *Quart. J. Roy. Meteor. Soc.*, **135**, 1277–1291, doi: 10.1002/qj.431.

van Heerwaarden, C., J. Vila-Guerau de Arellano, A. Gounou, F. Guichard, and F. Couvreux, 2010: Understanding the daily cycle of evapotranspiration: A method to quantify the influence of forcings and feedbacks. *J. Hydrometeor.*, **11**, 1405–1422, doi: 10.1175/2010JHM1272.1.

Vila-Guerau de Arellano, J., C. van Heerwaarden, and J. Lelieveld, 2012: Modelled suppression of boundary-layer clouds by plants in a CO_2-rich atmosphere. *Nature Geosci.*, **5**, 701–701, doi:10.1038/NGEO1554.

Wang, J., R. Adler, G. Huffman, and D. Bolvin, 2014: An Updated TRMM Composite Climatology of Tropical Rainfall and Its Validation. *J. Climate*, **27**, 273–284, doi:10.1175/JCLI-D-13-00331.1.

Ward, R., 1906: The classification of climates: I. *Bull. Amer. Geogr. Soc.*, **38**, 401–412.

Weaver, C., and V. Ramanathan, 1995: Deductions from a simple climate model: Factors governing temperature and atmospheric thermal structure. *J. Geophys. Res.*, **100**(D6), 11515–11591.

Wetherald, R., and S. Manabe, 1975: The effects of changing the solar constant on the climate of a general circulation model. *J. Atmos. Sci.*, **32**, 2044–2059.

Williams, E., 2004: Islands as miniature continents: Another look at the land-ocean lightning contrast. *J. Geophys. Res.*, **109**, 2–6, doi:10.1029/2003JD003833.

Wordsworth, R., F. Forget, F. Selsis, J. Madeleine, E. Millour, and V. Eymet, 2010: Is Gliese 581d habitable? Some constraints from radiative-convective climate modeling. *Astron. Astrophys.*, **522**, A22, doi: 10.1051/0004-6361/201015053.

Wyant, C., C. Bretherton, P. Blossey, and M. Khairoutdinov, 2012: Fast Cloud Adjustment to increasing CO_2 in a Superparameterized Climate Model. *J. Adv. Model. Earth Sys.*, **4**, M05001, doi:10.1029/2011MS000092.

Yang, G. and J. Slingo, 2001: The diurnal cycle in the tropics. *Mon. Wea. Rev.*, **129**, 784–801.

Zeng, N., and J. Neelin, 1999: A Land-Atmosphere Interaction Theory for the Tropical Deforestation Problem. *J. Climate*, **12**, 857–872.

Zhang, L., Q. Li, Y. Gu, K. Liou, and B. Meland, 2013: Dust vertical profile impact on global radiative forcing estimation using a coupled chemical-transport-radiative-transfer model. *Atmos. Chem. Phys.*, **13**, 7097–7114, doi:10.5194/acp-13-7097-2013.